

Resolution Enhancement Techniques (RET) for Immersion Lithography

LING MOH LUNG

NATIONAL UNIVERSITY OF SINGAPORE

2010

Resolution Enhancement Techniques (RET) for Immersion Lithography

LING MOH LUNG
(B.Eng. (Hons), NUS)

A THESIS SUBMITTED
FOR THE DEGREE OF DOCTOR OF PHILOSOPHY
DEPARTMENT OF MECHANICAL ENGINEERING
NATIONAL UNIVERSITY OF SINGAPORE

2010

Acknowledgements

I would like to express my outmost gratitude towards my project supervisors, Prof Tay Cho Jui and Prof Quan Chenggen for their guidance in this research work. They have been very patient in guiding and providing insightful advices which is helpful in my progress. Working under them has been a very fruitful learning experience. I would like to thank Prof Tay for his patience on checking through my manuscript and this dissertation to ensure they are technically and grammatically correct. Furthermore, I feel thankful to have Prof Quan for the productive discussion on technical aspect of this work. This project is a joint effort between National Universtiy of Singapore (NUS) and GlobalFoundries Singapore Private Limited. I am always grateful to have Dr. Lin Qunying, and Dr. Chua Gek Soon as my mentors. Dr. Lin has been helpful in providing the necessary resources for this project and we have numerous constructive discussions. I appreciate her efforts in guiding me. Dr. Chua has been a wonderful mentor as well. Throughout the course of this study, he has inspired me to explore and think independently. I would not have learnt as much without his guidance. He has shared useful experiences and motivated me along the course of this study. Furthermore, I would like to also thank Tan Sia Kim. Sia Kim is open-minded and experienced. He has shared his knowledge selflessly and I enjoyed the discussions with him.

I would also like to thank Dr. Lap Chan (Director) and Dr. Ng Chee Mang (Program Manager) for giving me this wonderful opportunity to join the Special Project group (Local universities collaboration group). Dr. Lap Chan has great passion in teaching and he has inspired his students to think critically. He is always approachable for advices. Both Dr. Chan and Dr. Ng has shared their knowledge on semiconductor manufacturing

which is beneficial for me as I am new to the field. Dr. Ng has also provided useful advices and necessary resources. I also thank all of my colleagues from the Special project group as we have enjoyed the time learning and sharing knowledge. I have gained tremendous amount of information from attending their research sharing sessions.

Finally, I am sincerely thankful to have my family for giving me encouragements and supports all the time. They have always been caring and supportive throughout this wonderful four year journey of my research.

Table of contents

Acknowledgements	i
Summary	vii
List of Tables	ix
List of Figures	x
List of symbols	xviii
Chapter 1 Introduction	
1.1 Background	1
1.2 Research contributions	6
1.3 Outline	8
Chapter 2 Literature review	
2.1 Immersion lithography	
2.1.1 Limitation of optical lithography	10
2.1.2 Extensions of optical lithography	15
2.1.3 Resolution improvement	19
2.1.4 Imaging problems	
2.1.4.1 Process related and haze defects.....	23
2.1.4.2 Forbidden pitch phenomenon in the application of off-axis illumination	25
2.1.4.3 Contact holes patterning challenges	27
2.2 Resolution enhancement techniques (RET)	
2.2.1 Optical and process correction (OPC)	31

2.2.2 Off-axis illumination (OAI)	36
2.2.3 Phase-shifting mask (PSM)	39
2.2.4 Advanced resolution enhancement techniques	44
2.3 Optical imaging theory	
2.3.1 Fraunhofer diffraction	50
2.3.2 Fourier optics for aerial image formation.....	53
2.3.3 Partial coherent imaging theory.....	57
2.3.4 High numerical aperture (NA) vector imaging	61
Chapter 3 Theoretical analysis	
3.1 Influence of mask defect on image	63
3.2 Resolution enhancement	69
3.3 Effect of changing mask openings shape on imaging	82
Chapter 4 Experimental and simulation work	
4.1 Linewidth and process windows measurement	
4.1.1 Linewidth measurement	90
4.1.2 Focus exposure matrix	91
4.1.3 Lithography exposure tool	93
4.2 Mask design.....	94
4.3 Simulation work	
4.3.1 Effect of progressive defect growth on imaging	96
4.3.2 Modified OAI for resolution enhancement at forbidden pitch.....	97

4.3.3 Circular mask openings and radial segmentation approach for contact holes patterning	99
---	-----------

Chapter 5 Results and Discussion

5.1 Influence of mask defect

5.1.1 Resolution improvement by immersion lithography	102
--	------------

5.1.2 Critical factors in defect printability

5.1.2.1 Effect of changes in mask transmission.....	105
5.1.2.2 Effect of changes in mask phase	108
5.1.2.3 Effect of pattern density	109
5.1.2.4 Effect of transmission.....	116
5.1.2.5 Effect of phase shift	118
5.1.2.6 Effect of partial coherence	120

5.2 Illumination optimization for off axis illumination

5.2.1 CD, DOF and η for single and double annular sources

5.2.1.1 CD through pitch comparison	124
5.2.1.2 DOF through pitch comparison	126
5.2.1.3 Overlap ratio η comparison.....	127

5.2.2 Optimization based on η for double annular source shape.....

5.2.3 Extension to other source shapes

5.2.4 Optical proximity correction for modified OAI

5.2.4.1 Line end shortening on end to end structures.....	139
5.2.4.2 Line end shortening for staggered structure	144

5.3 Resolution enhancement for contact hole patterning	
5.3.1 CD and DOF performance comparison	148
5.3.2 Comparison of NILS, MEEF and aerial image	153
5.3.3 Enhancement for staggered contact holes pattern	160
5.3.4 Optimization of Δr in radial segmentation approach	165
Chapter 6 Conclusions and recommendations for future work	
6.1 Conclusions	169
6.2 Recommendations for future work	171
References	173
Appendix A List of publications	192
Appendix B Rayleigh resolution criterion	193
Appendix C Resist Calibration	198

Summary

This study focuses on resolution enhancement techniques (RET) for immersion lithography regime. Primarily, this study deals with interaction of mask defects on wafer imaging, forbidden pitch phenomenon in the application of off-axis illumination (OAI), and contact holes patterning challenges.

Progressive growth of haze defects on attenuated phase-shifting masks (AttPSM) has become one of the most common issues in 193 nm immersion lithography. Thorough understandings of mask defects and their influence on imaging are necessary in controlling process variations and implementing systematic defects disposition. In this study, the impact of mask defect on lithography is studied through experiments and simulations. Masks with programmed defects of various sizes at different locations are studied and simulations are carried out for haze defects of different phases and transmissions. An image perturbation model is also used to describe the behavior of mask defects.

OAI is widely applied in optical lithography for resolution enhancement. It refers to illumination light that is tilted away from the normal incident angle. In practice, the selections and settings for OAI are often optimized to the smallest pitch in a particular design. However, the setting for one pitch may not be beneficial for other pitches. At certain pitches, diffraction pattern distribution has resulted in a destructive interference due to large phase difference between different diffraction orders. Consequently, image contrast is affected and depth of focus (DOF) is often reduced drastically. At such pitches, the critical dimension (CD) fluctuation is significant and DOF is often insufficient for processing. Consequently, forbidden pitches have become one of the limiting factors in

the design of integrated circuit and are often avoided. An illumination source shape modification to minimize CD and DOF fluctuation at forbidden pitch is proposed. Overlap ratio η between 1st order (and higher order) and 0th order light is used in the process of determining appropriate partial coherent settings for the proposed source shape. The modified source shape consists of basic OAI source shapes which could be extended to a double annular, double dipole or double quadrupole configuration.

Contact holes patterning has become increasingly challenging as dimension reduces. In the conventional approach to pattern contact holes, mask with square apertures is used. However, as the dimension of features reduces, the diffracted light from mask arrives at larger angle at the pupil plane. Since optical lithography is a low-pass frequency filtering process, this has resulted in additional loss of light which degrades the image contrast. A new approach for contact hole patterning is presented. Instead of targeting a square shape in printed feature, a circular shape is targeted. In this approach, circular apertures on mask are used. The patterning of circular apertures on mask has become possible with the advancement of mask writing tools. The imaging performance resulting from circular apertures will be compared with the conventional approach.

List of Tables

2.1	Progress of wavelength reduction in optical lithography.....	11
4.1	Experimental conditions for programmed defect mask exposure.....	95
4.2	Summary of simulation conditions for defect study.....	97
4.3	Summary of illumination conditions.....	98
4.4	Summary of pitch range (Target CD = 45 nm).....	98
4.5	Illumination conditions for other sources.....	99
4.6	Illumination conditions for line end shortening study.....	99
4.7	Summary of simulation conditions for regular contact holes array.....	100
4.8	Summary of simulation conditions for staggered contact holes array.....	101
4.9	OPC feature size for staggered contact hole pattern	101
5.1	Influence of different defect parameters.....	122

List of Figures

1.1	Illustration of positive and negative resist process.....	2
1.2	Growing number of transistors in a microprocessor.....	3
1.3	Projection of critical dimension (CD) for future technology node.....	4
1.4	Key components of lithography system and resolution enhancement techniques for each component.....	5
2.1	Evolution of lithography lens system.....	13
2.2	Historical trend for NA over the past decade.....	13
2.3	Historical trend of process related resolution factor k_1	14
2.4	Definition of numerical aperture (NA) , $NA = n \sin \alpha$	16
2.5	Schematic diagram of dry and immersion system.....	18
2.6	Configuration between lens and wafer stage for an immersion exposure tool.....	19
2.7	Optical path difference (OPD) between on-axis and off-axis light at point P.....	21
2.8	Optical path difference (OPD) between on-axis and off-axis light at point P.....	22
2.9	Types of defects classified by location: (a) pinhole, (b) post, (c) clear extension, (d) dark extension.....	24
2.10	Haze defect occurrence on masks.....	25
2.11	Types of off-axis illumination:(a)Annular, (b)Dipole, (c)Quadrupole...	26
2.12	A typical CD response over different pitch as a result of application of OAI.....	27

2.13	Contact holes array of different pitch showing corner rounding and side lobe printing issues.....	29
2.14	Optical proximity effects on linewidth and process windows variation...	32
2.15	Fragmentation method: (a)Hammerhead at line end ; (b)Corner serifs...	34
2.16	Scattering bars placed adjacent to isolated feature.....	35
2.17	SRAF for contact holes.....	36
2.18	Effect of OAI on diffraction order distribution.....	38
2.19	Conventional and off-axis partial coherent illumination.....	38
2.20	Phase difference due to thickness difference of d.....	41
2.21	Alternating phase-shifting mask (AltPSM).....	42
2.22	Phase conflicts in application of AltPSM.....	43
2.23	Attenuated phase-shifting mask (AttPSM).....	44
2.24	Illustration of a double exposure process: (a) design, (b) first exposure mask, (c)second exposure mask, (d) printed pattern on wafer.....	46
2.25	Typical double patterning processes: (a) Litho-etch-litho-etch (LELE), (b) Litho-freeze-litho-etch (LFLE), and (c) Self aligned double patterning (SADP).....	47
2.26	Pixelated mask for advanced logic patterning.....	49
2.27	Free form illumination based on source mask optimization.....	49
2.28	Schematic diagram of evanescent wave assist features.....	50
2.29	Illustration of Huygens' principle.....	51
2.30	Diffraction zone depends on distance from the slit.....	53
2.31	Common Fourier transform pairs.....	54

2.32	Diffraction of light passing through mask collected at projection lens...	56
2.33	Definition of spatial frequencies in relation with lithography system.....	57
2.34	Effect of tilted incident light on the distribution of diffraction order.....	59
2.35	Diffraction order distribution for coherent and partial coherent illumination.....	60
2.36	TE and TM polarization of electric field.....	63
3.1	Interference between two neighboring partial coherent beams.....	64
3.2	Illustration of main feature and a neighboring defect on a mask.....	66
3.3	Mutual coherence of an annular source.....	68
3.4	Spatial frequencies shift due to partial coherent illumination.....	71
3.5	Diffraction orders distribution of a mask subjected to partially coherent light.....	71
3.6	Diffraction orders distribution for OAI.....	72
3.7	Typical diffraction pattern observed at projection pupil plane for annular OAI.....	73
3.8	Schematic diagram of Köhler illumination.....	73
3.9	Diffraction order of binary mask illuminated by an off-axis source point.....	74
3.10	Definition of spatial frequencies f_x and f_y	75
3.11	Preferable overlap between 1 st and 0 th order diffracted light at pupil plane for small and large pitch size.....	79
3.12	Comparison between single and double annular source shape.....	81
3.13	Diffraction orders distribution for double annular source.....	81

3.14	Improvement of overlapping area at pupil plane using a double annular source.....	82
3.15	Normalized intensity plot for circular and square aperture along positive x – axis.....	84
3.16	Comparison between Bessel and sinc function envelope.....	87
3.17	Illustration of radial segmentation approach.....	89
4.1	Schematic diagram of a SEM.....	90
4.2	Wafer split for FEM experiment.....	91
4.3	Illustration of a typical Bossung plot.....	92
4.4	Illustration of (a) Common process window ; (b) Exposure latitude against depth of focus.....	93
4.5	Lithography exposure tool.....	94
4.6	Location of programmed defect relative to main features.....	95
4.7	Location of simulated defect relative to main features.....	96
4.8	Radial segmentation for staggered contact hole pattern.....	100
5.1	Comparison between CD through pitch performance for immersion and dry lithography.....	102
5.2	Comparison of DOF through pitch between immersion and dry lithography.....	103
5.3	Changes in CD as a result of mask transmission error (a) immersion ; (b) dry.....	105
5.4	Changes in CD as a result of mask phase error (a) immersion ; (b) dry.....	107

5.5	CD variation for an active layer with adjacent and mid-point defects.....	109
5.6	CD variation for a polysilicon layer with adjacent and mid-point defects.....	110
5.7	Comparison of experimental CD variations for an active and polysilicon layer with adjacent defect.....	111
5.8	Simulated CD variation of 160nm and 220nm pitch with adjacent and mid-point defects ($T_d = 6\%$, $\phi_d = 180^\circ$).....	112
5.9	Simulated CD variation of 160nm and 220nm pitch with adjacent and mid-point defects ($T_d = 0\%$, $\phi_d = 0^\circ$).....	114
5.10	Simulated CD variation of 180nm pitch with adjacent and mid-point defects and different transmissions ($\phi_d = 180^\circ$).....	115
5.11	Simulated CD variation of 180nm pitch with adjacent and mid-point defects and different transmissions ($\phi_d = 0^\circ$).....	117
5.12	Simulated CD variation of 180nm pitch with adjacent defects and different phase shifts ($T_d = 10\%$).....	118
5.13	Simulated CD variation of 180nm pitch with mid-point defects and different phase shifts ($T_d = 10\%$).....	119
5.14	Simulated CD variation of 140nm pitch with adjacent defects and different partial coherence settings (Annular OAI, $\sigma_{out} = 0.94$, $T_d = 0\%$, $\phi_d = 0^\circ$).....	120

5.15	Simulated CD variation of 140nm pitch with mid-point defects and difference partial coherence settings (Annular OAI, $\sigma_{out} = 0.94$, $T_d = 0\%$, $\phi_d = 0^\circ$).....	121
5.16	CD through pitch for a double annular source (Condition 3) and conventional annular source (Condition 4).....	124
5.17	DOF through pitch for double annular source (Condition 3) and conventional annular source (Condition 4).....	125
5.18	Overlapping factor η and DOF for a double annular (Condition 3) and conventional annular illumination (Condition 4).....	128
5.19	Optimum partial coherent values for different pitches.....	129
5.20	DOF and η for different σ_{in} for 130nm pitch using an annular source shape (NA=1.12, σ_{out} =0.88).....	130
5.21	Comparison of DOF and η for a double annular source using Conditions 1, 2 and 3.....	133
5.22	CD through pitch performance comparison between conventional dipole and double dipole illuminations.....	134
5.23	Common process window between 130 nm, 160 nm and 200 nm pitch.....	135
5.24	Comparison between CD through pitch performance for conventional quadrupole and double quadrupole illuminations.....	136
5.25	Common process window (hatched area) for 130, 160 and 200nm pitch contact holes array.....	137

5.26	Line end shortening for an end to end structure.....	138
5.27	OPC feature size comparison between dipole and double dipole illumination for end to end structure.....	142
5.28	Line end shortening for a staggered structure.....	143
5.29	OPC feature size comparison between dipole and double dipole illumination for a staggered structure.....	145
5.30	Illustration of a regular contact hole array.....	147
5.31	CD through pitch performance comparison between a mask with circular and square apertures.....	148
5.32	DOF through pitch comparison between a mask with circular and square apertures.....	149
5.33	Common process window comparison for a contact hole array of 130 nm and 500 nm pitch.....	151
5.34	NILS through pitch comparison between a mask with circular and square apertures.....	153
5.35	MEEF through pitch comparison between a mask with circular and square apertures.....	155
5.36	Aerial image intensity plot for contact holes array of (a) 130 nm , (b) 150 nm , and (c) 190 nm pitch.....	156
5.37	A comparison of 1 st order diffraction amplitude for a mask with circular and square apertures.....	158
5.38	Illustration of a staggered contact hole pattern.....	159

5.39	A comparison of DOF between mask with circular and square aperture for a staggered contact hole pattern with spacing d	161
5.40	A comparison of NILS between mask with circular and square apertures for a staggered contact hole pattern with spacing d	162
5.41	A comparison of aerial image intensity between mask with circular and square apertures for a staggered contact holes pattern with (a) $d = 160\text{nm}$, and (b) $d = 200\text{nm}$	164
5.42	Optimization of radial extension Δr for staggered contact holes with different spacing d by NILS.....	165
5.43	A comparison of aerial image intensity plot comparison between a staggered contact hole pattern with and without radial extension for spacing (a) $d = 100\text{ nm}$, (b) $d = 160\text{ nm}$ and, (c) $d = 200\text{nm}$	167
6.1	Illustration of proposed concept for line end shortening correction.....	171

List of symbols

k_1	Process related resolution factor
λ	Wavelength of light
NA	Numerical aperture
k_2	Process related depth of focus factor for dry lithography
n	Refractive index
α	Maximum half angle of incident light on a lens
δ	Optical path difference
k_3	Process related depth of focus factor for immersion lithography
R	Resolution
p	Pitch
$\Delta\phi$	Phase difference
$E_i(x, y)$	Electric field incident on mask
$m(x, y)$	Mask function
$M(f_x, f_y)$	Fourier transform of mask function
σ	Partial coherence factor
f_x	Spatial frequency in x direction
f_y	Spatial frequency in y direction
$S(f_x', f_y')$	Source function
I	Image intensity
μ_{eff}	Effective mutual coherence between main and neighboring features

T	Transmission
ϕ_d	Phase change caused by a defect
a_0	Magnitude of 0 th order light
a_1	Magnitude of 1 st order light
r	Radius of a circular opening on mask
Δr	Radial extension
θ_r	Opening angle of a segment for circular openings mask

Chapter 1 Introduction

Over the past few decades, semiconductor industry has achieved remarkable advances in integrated circuits (IC) technology. Optical lithography has played a crucial role in meeting the demand for continual miniaturization of integrated circuit features and supporting cost effective high throughput volume manufacturing. While the next generation lithography (NGL) technology such as extreme ultraviolet (EUV) lithography experiences delays in progress, 193 nm immersion lithography was introduced and has successfully bridged the gap between current and the next generation lithography. Nevertheless, immersion lithography needs resolution enhancement techniques (RET) to sustain the aggressive demand for dimensional scaling. A brief background on optical lithography and the motivation for the study of resolution enhancement techniques is covered in this chapter.

1.1 Background

The fabrication of an IC chip involves various physical and chemical processes on silicon wafers. These processes mainly consist of film deposition, patterning and doping. (Wolf, 1990) Optical lithography is the process of defining features on wafers which then would be subjected to certain processes. Fig. 1.1 shows typical positive and negative resist lithography process. The patterning and etching or deposition process need to be repeated for around 25 to 40 times to produce a fully functional IC chip. Circuit features that are produced on IC chip are in nanometer accuracy and the layout is often highly

complicated. A state of the art IC chip contains more than 100 millions transistor packed in an area of 1cm^2 .

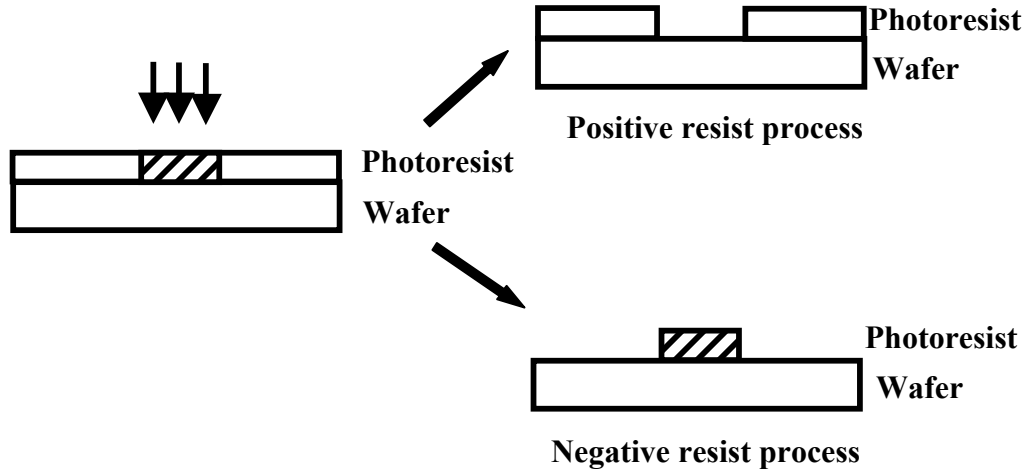


Fig. 1.1 Illustration of positive and negative resist process

Over the years, circuit features continue to shrink and IC chips functions are improving in a tremendous pace. Moore's law has driven the advancement of semiconductor industry and has become a benchmark for the progress of the industry. Proposed by Intel co-founder Gordon Moore, Moore's law suggests that the number of transistors in an IC chip has to be increased by two times in a period of 18 months to maintain the cost effectiveness in the semiconductor industry. (Moore, 1965 and 1976) Comparison between Moore's law prediction and actual advancement for Intel microprocessor chip is shown in Fig. 1.2. (Intel, 2005) It can be seen that the number of transistors packed in an IC chip has increased by two time in a period of 18 months.

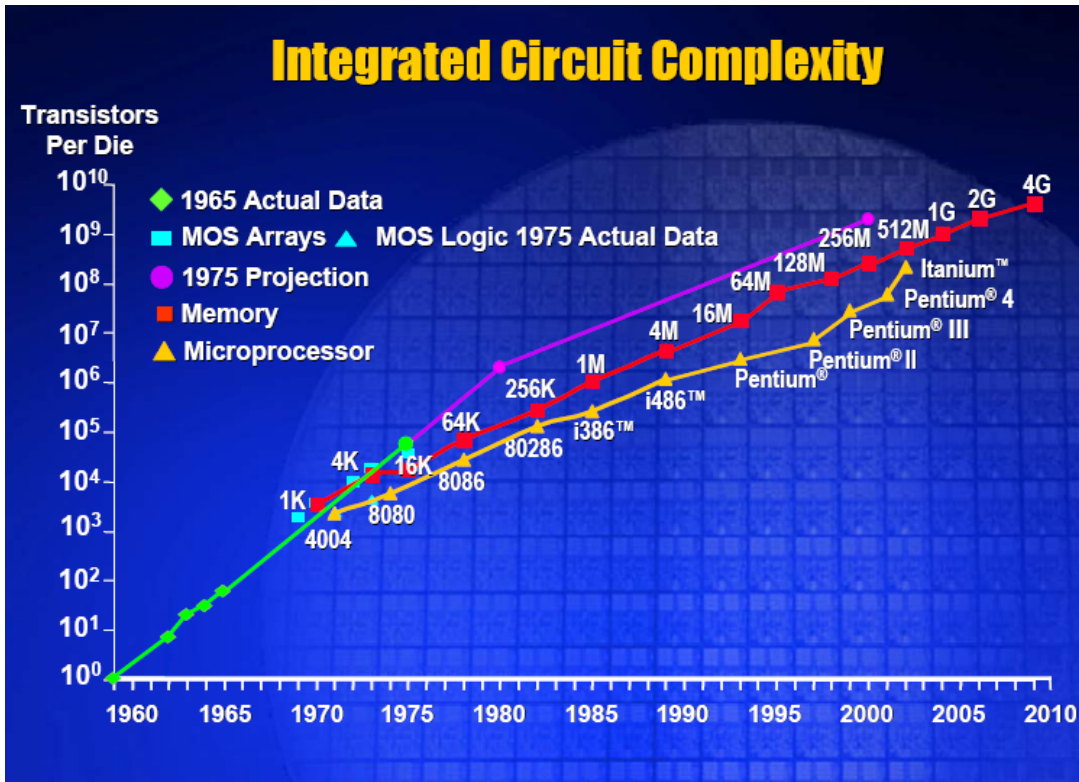


Fig. 1.2 Growing number of transistors in a microprocessor

The demand of Moore's law has to be met by continuously shrinking the size of micro circuit feature on a chip. Fig. 1.3 shows the ITRS roadmap which specifies the requirement in reduction of gate width as technology advances. (ITRS, 2007) There are several key components in a lithography system, namely illumination source, mask, projection lens and wafer stage control, as illustrated in Fig. 1.4. (Ito and Okazaki, 2000) Improvement in resolution can be accomplished by reducing the exposure wavelength, changing the illumination source shape, applying phase shifting mask, increasing numerical aperture (NA) of the lens system, and optimizing film stack as well as process control, as illustrated in Fig. 1.4. Nevertheless, wavelength reduction and fabricating lens with larger NA requires significant investment in terms of time and resources. Other

techniques that are mentioned essentially modify the wavefront that arrives at the wafer image plane, categorized as RET. Resolution enhancement techniques are essential to enable lithography process to meet the demand in dimensional scaling while exposure wavelength and new infrastructure are being developed. Meanwhile, RET also requires relatively less investment in resource compared to development of new tools.

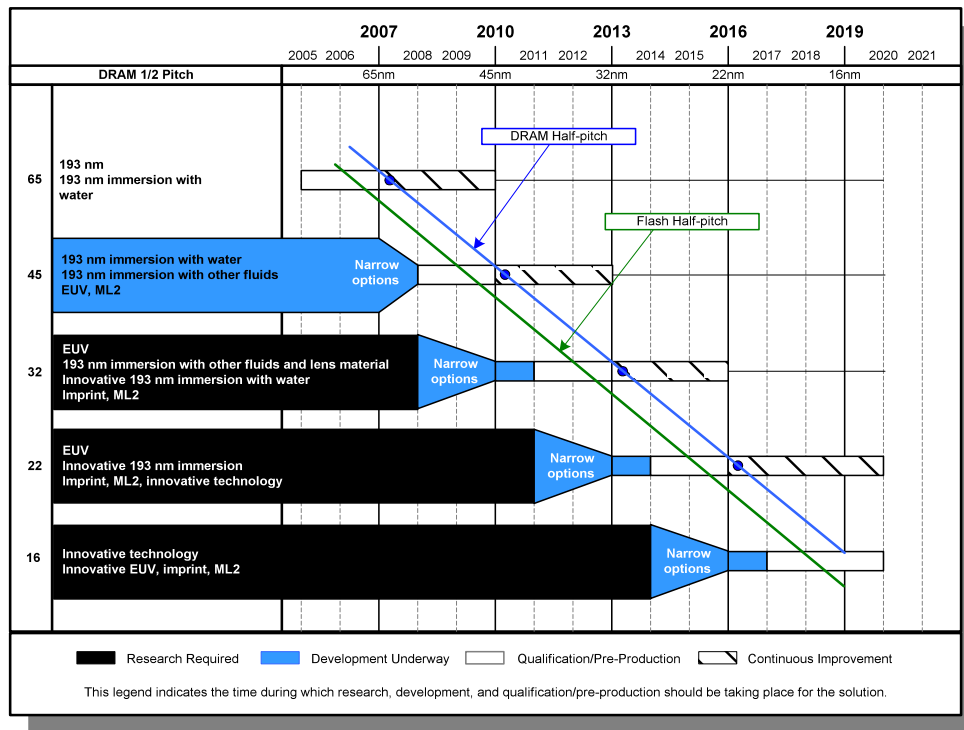


Fig. 1.3 Projection of critical dimension (CD) for future technology node

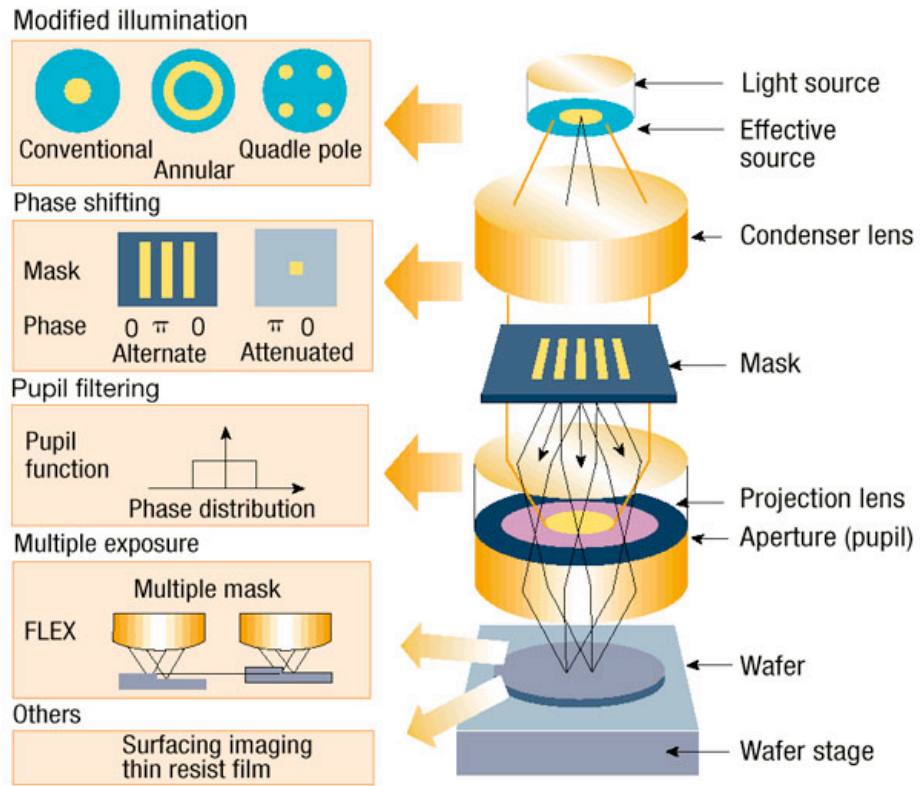


Fig. 1.4 Key components of lithography system and resolution enhancement techniques for each component

1.2 Research contributions

This thesis focuses on investigating several issues in RETs for immersion lithography. The investigations are conducted in several aspects of lithography system through understanding of fundamental issues. Based on the understanding developed, resolution enhancement techniques for process windows enhancement in sub 65 nm technology node are proposed.

Application of phase shifting mask has improved the resolution and process window in lithography process. Nevertheless, the occurrence of progressive mask defects growth (or haze) has been observed increasingly in 193 nm lithography. This can be attributed to the increasing exposure dose and prolonged exposure in advanced technology node. With the advent of immersion lithography, the resolution limit of lithography system is improved. Hence, it is important in understanding the contribution of different factors that contribute to haze defect printability to ensure the resolution improvement provided by phase shifting mask is not compromised. Through systematic study, critical factors that contribute to defect printability are identified.

In the application of OAI, forbidden pitch phenomenon is observed and it limits the range of pitch that can be patterned in single exposure process. This is attributed to non optimum overlapping of diffraction orders at the pupil plane resulted by conventional OAI source shape since it is optimized to smaller pitch. Modification to conventional OAI source shape is proposed in this study. It is accomplished by removing the portion that contributes to degradation of image contrast at forbidden pitch. The results have

shown improvement of through pitch CD uniformity and process windows. From the study, the forbidden pitch phenomenon is effectively minimized.

The patterning of contact holes is one of the most challenging issues in lithography, particularly in sub 65 nm regime. Intrinsicly, it is more difficult to optimize the patterning due to two dimensional nature of contact holes. As dimensions continue to shrink, the effect of diffraction has resulted in significant amount of corners rounding and loss of process windows robustness. The conventional method in determining mask design is done by targeting a square printed target and performs optical proximity correction to achieve a final image that is as close to a square as possible. An alternative approach by changing the printed target to circular and perform radial segmentation proximity correction is proposed. The results show promising potential in improving through pitch image contrast and process window robustness.

In the course of this study, several publications have been generated. These include five conference and three journal papers. In addition, two US patent applications have been submitted. (See Appendix A)

1.3 Outline

This dissertation is organized as follows: Chapter 2 provides an overview on the development in immersion lithography and RET. The effect of immersion lithography on resolution and process windows is analyzed. In addition, issues that are the focus of this thesis are reviewed. Furthermore, an overview of optical imaging theory used for modeling of optical lithography is presented.

In Chapter 3, theoretical development that forms the basis of the study in the course of this research is presented. The contribution of different factors of a defect on main feature image formation is described with the aid of image perturbation model. Development of customized OAI based on the overlapping ratio between zero order and first order diffracted light at the pupil plane is presented. The difference between proposed circular apertures and conventional square aperture for contact formation is highlighted.

In Chapter 4, the experimental and simulation approaches that are adopted in this thesis are discussed.

Chapter 5 presents the results and discussion based on the study conducted. The effect of mask cleaning and progressive defect growth on the application of phase shifting mask for immersion lithography is first discussed. Subsequently, the impact of implementing the proposed customized OAI on forbidden pitch effect suppression is examined. Furthermore, improvements in contact hole patterning by circular printed target are presented.

In Chapter 6, the thesis concludes with a summary on the important findings and results derived from the course of this study. Meanwhile, some suggestions for future research based on the observations and understandings acquired are given.

Chapter 2 Literature review

Optical lithography has been widely employed for achieving continuous miniaturization of integrated circuit. However, at 193 nm argon fluoride (ArF) dry lithography, the industry had encountered a bottleneck due to delays in EUV lithography. In this chapter, the motivation for lithography technology to move towards immersion lithography and limitations of optical lithography are discussed. The impact of immersion lithography on resolution and depth of focus (DOF) is discussed based on theoretical analysis. A review on issues that are subject of study in this thesis is provided.

2.1 Immersion lithography

2.1.1 Limitation of optical lithography

The resolution limit of an optical lithography system is determined by the Rayleigh equation (Lin, 1986)

$$R = k_1 \frac{\lambda}{NA} \quad (2.1)$$

where k_1 is resolution factor related to process, λ is the wavelength of the exposure system and NA is the numerical aperture. Smaller feature can be patterned by reducing the k_1 factor, decreasing the exposure wavelength, and increasing the NA of the lens. Table 2.1 shows historical data of wavelength and minimum linewidth in optical lithography (Burning, 2007). From 1980s to early 1990s, mercury arc lamp is sufficient to meet the challenge of linewidth requirement. Subsequently, the challenge of further reduction in linewidth and increase in throughput which demands source with higher power is met with introduction 248 nm krypton fluoride (KrF) excimer laser light source.

Reduction of linewidth below 100 nm is achieved through introduction of 193 nm argon fluoride (ArF) laser as light source.

Table 2.1 Progress of wavelength reduction in optical lithography

Year	Wavelength (nm)	Light source	Linewidth (nm)
1986	436	Mercury arc G-line	1200
1988	365	Mercury arc I-line	800
1991	365	Mercury arc I-line	500
1994	248	KrF excimer laser	350
1997	248	KrF excimer laser	250
1999	248	KrF excimer laser	180
2001	248	KrF excimer laser	130
2003	193	ArF excimer laser	90
2006	193	ArF excimer laser	65

The successful introduction of shorter wavelength depends on several factors. First, light source that is capable of delivering adequate power to satisfy the high throughput requirement of lithography. Second, the development of photoresist and optical materials that is compatible with the light source. Beyond 193 nm ArF excimer laser, 157 nm Fluorine (F₂) excimer laser was pursued but it was removed from the roadmap of lithography due to difficulties in lens material and photoresists (Fahey et. al, 2001). Another candidate considered as successor to 193 nm lithography is extreme ultra-violet (EUV) lithography. The exposure wavelength for EUV is 13.5 nm and this could enable further scaling of linewidth to below 22 nm technology node. The optical element for EUV lithography will be based on reflective optics. Nevertheless, there are challenges which include achieving source power that supports high throughput production, photoresist sensitivity, and masks inspection (Hermans et. al, 2010).

The enhancement in NA of lens system can also reduce the minimum linewidth. The improvement in lens design and manufacturing technology has enabled a steady increase in NA. The physical limit of NA for a lens system with air as medium between lens and the wafer is 1. However, the maximum NA achieved with dry optical system is 0.93 due to difficulties in controlling the aberrations and manufacturing of large lens system (Matsuyama et. al.,2006). The evolution of lithography lens system can be seen in Fig. 2.1, as NA becomes larger, the number of optical lens element and physical size of lens increase significantly.

Fig 2.2 shows the NA trend for lithography optical lens system over the years (Burning, 2007). From 1980s to 2006, NA of optical lens system has increased from 0.30 to 0.93. Since the physical limit of dry optical lens system is 1, further improvement in NA offers diminishing gain in reduction of linewidth with other parameters remains the same.

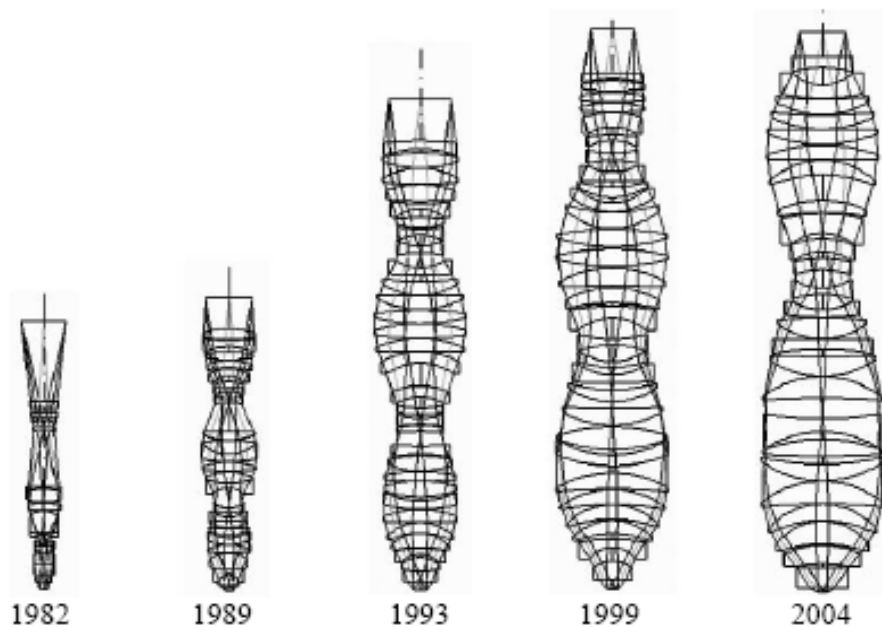


Fig. 2.1 Evolution of lithography lens system

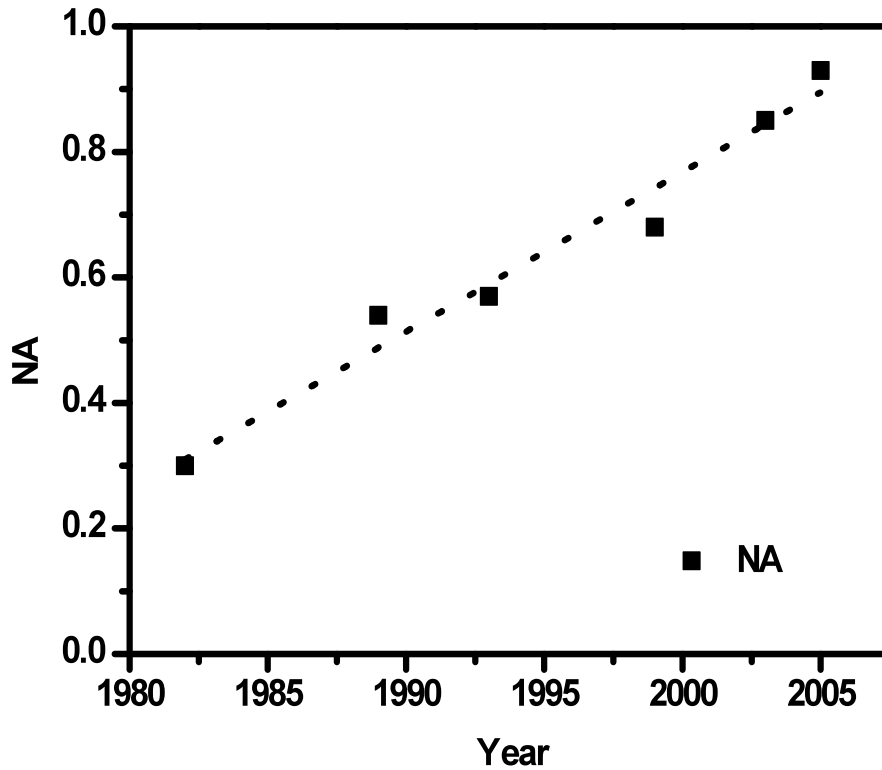


Fig 2.2 Historical trend for NA over the past decade

The process related resolution factor k_1 can be lowered to enable smaller feature size. This can be achieved through improvement in tools accuracy, better process control and RET, which mainly include modified illumination schemes, and photomask techniques. The historical trend of k_1 is shown in Fig 2.3. Over the past decades, the value of k_1 has dropped from 0.75 to around 0.35. Lower k_1 indicates increasingly complex process control and aggressive RET solutions, which results in higher manufacturing cost. The physical limit of k_1 for a single exposure lithography process is 0.25, but it would require significant amount of efforts to push the k_1 below 0.35 due to cost considerations and challenges in process controls.

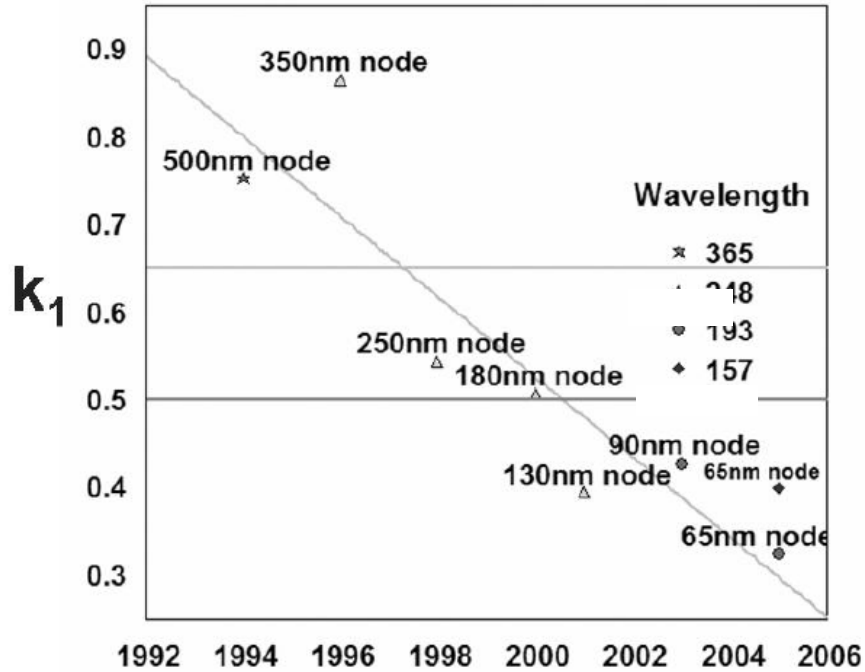


Fig 2.3 Historical trend of process related resolution factor k_1

From Table 2.1, Fig 2.2, and Fig 2.3, it is not difficult to observe that improvement in all three factors above is equally crucial to achieve the smallest possible resolution in optical lithography. Thus far, the challenge of reducing linewidth has been addressed and allows the industry to progress with tremendous pace. Nevertheless, dry optical lithography faces the limitation of further improvement in lens NA, significant rise in cost for more complicated process controls, increasingly complicated RET, as well as delays in the introduction of shorter exposure wavelength. The industry has to find an intermediate solution that is cost effective to bridge the gap between 193 nm optical lithography and next generation lithography with shorter wavelength.

Apart from minimum linewidth, DOF is another important factor that determines the resolution limit of a lithography process. Depth of focus can be defined as the range of focus which keeps the linewidth of the printed feature within 10% of targeted value,

given a specified range of exposure dose variation. The expression for DOF is written as (Lin, 1986)

$$\text{DOF} = k_2 \frac{\lambda}{\text{NA}^2} \quad (2.2)$$

Similar to k_1 , k_2 is the process related DOF factor. k_2 depends on the criteria used to define acceptable imaging qualities and on the type of feature being imaged. A more detail discussion on Eq. (2.1) and (2.2) is given in Appendix B. It can be observed that DOF is directly proportional to the exposure wavelength and inversely proportional to the square of NA. It is interesting to observe that while smaller linewidth is pursued, the DOF suffers with decreasing wavelength and increasing NA. Therefore, while pursuing smaller linewidth, it is necessary to ensure that the process DOF is not severely degraded. There are several approaches to cope with diminishing DOF, which include RET, application of chemical mechanical planarization (CMP) processes, optimization of film stack, reduction in lens aberrations and improvement in process controls.

2.1.2 Extensions of optical lithography

In previous discussion, it has been mentioned that the physical limit of NA for a lithography lens system with air (refractive index, $n = 1$) as medium in between lens element and wafer is 1. Generally, NA is determined by the product of refractive index n of the medium and the sine of the half maximum angle α of incident light that can be collected by the lens, as shown in Fig 2.4.

$$\text{NA} = n \sin \alpha \quad (2.3)$$

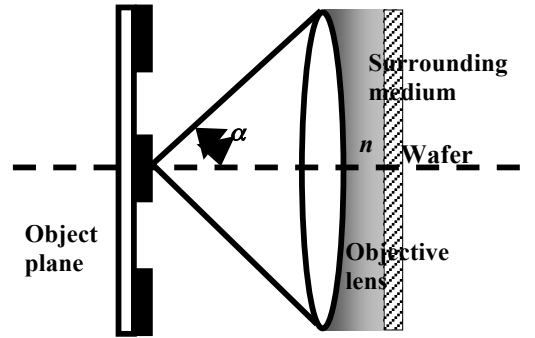


Fig 2.4 Definition of numerical aperture (NA), $NA = n \sin \alpha$

The maximum value of $\sin \alpha$ is 1. Thus, in order to achieve NA greater than unity, the medium between the lens and wafer has to be replaced with material with refractive index greater than 1. In 19th century, Lietz Wetzler has implemented this concept on microscopy and developed oil immersion microscopy with NA of 1.3 (Kawata et. al.,1989). It was widely accepted and become a common technique used nowadays. The earliest publication proposing the concept of immersion lithography is by Kawata et. al, in 1989. This had inspired the lithography community to look into the possibility of immersion lithography (Owen et. al., 1992). Despite having been known for a long time, immersion lithography has not gained serious attention until early 2000s (Hoffnagle et. al., 1999). This is because dry lithography systems have not reached the resolution bottleneck and there are difficulties in designing liquid handling system on the exposure tools. While 193 nm ArF dry lithography approaching resolution limit and the development in next generation lithography infrastructure encountering difficulties to be introduced on time, immersion lithography is proposed as intermediate solution to bridge the gap.

The basic idea of immersion lithography is to fill up the air space between the last element of the imaging lens and the surface of the photoresist on the wafer with a higher index medium (Lin, 2004a). At 193 nm, water appears to be the perfect medium for immersion. This is because the absorption coefficient is low for water and it has a reasonably high refractive index of 1.437 at 193 nm exposure wavelength. Apart from optical properties, other material characteristics have to be considered. The immersion fluid should not cause any physical or chemical change to the surfaces it is in contact with, including resist, lens and its antireflective coating. It also needs to have large dissolution capacity for gas so that any bubble formed can be dissolved quickly. The fluid viscosity should be low enough so that it can flow freely without slowing down the exposure tool scanning. Ultra pure degassed water possesses these properties and thus chosen as immersion fluid. The schematic diagram of immersion system compared with dry system is shown in Fig 2.5. The main difference between dry and immersion system is the medium between the lens and wafer and the water handling system. Other than that, much of the system remain unchanged and the infrastructure is essentially incremental upgrade from 193 nm dry lithography system.

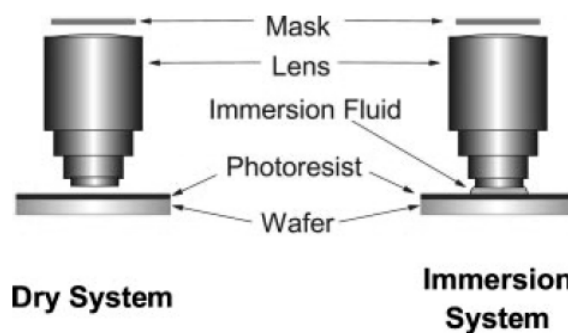


Fig 2.5 Schematic diagram of dry and immersion system

The configuration between the last lens element and wafer stage for an immersion exposure tool is shown in Fig 2.6 (Owa and Nagasaka, 2003). A small puddle of water is kept between the lens and the wafer during wafer exposure. New water is constantly pumped under the lens to keep the optical properties of the fluid consistent and to prevent contamination. There are several advantages which resulted in the adoption of this configuration. First, since the volume of water in this configuration is small, the wafer throughput can be maintained at around 120 wafers per hour (wph). Second, the wafer stage is identical to that of a dry system, saving time and cost for development. Third, the alignment, focusing and leveling setup remain unchanged (Chen et. al., 2005).

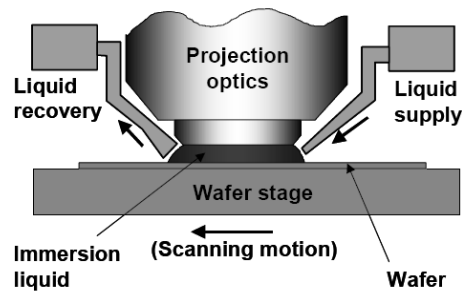


Fig 2.6 Configuration between lens and wafer stage for an immersion exposure tool

The development of immersion lithography progressed in an amazingly rapid rate. The research and development works started in 2002 in producing tools that support high volume manufacturing. Two years later in 2004, the first high volume production tool is shipped for applications in semiconductor manufacturing (Rothschild and Bloomstein, 2004). The rate of progress and acceptance by the semiconductor industry compared with previous lithography technology transitions is unique for immersion lithography. The

first full functional microprocessor is fabricated by immersion lithography system in a period of less than 10 months after the first shipment of immersion tools.

2.1.3 Resolution improvement

The validity of Eq. (2.1) in representing resolution in immersion lithography regime is examined. For an optical system, resolution can be estimated from determining the optical path difference (OPD) between the light that arrives from center of the lens and that arrives from the outermost edge of the lens. As shown in Fig. 2.7, the exact OPD, δ between light from center and edge of the lens at point P is (Lin, 2004b)

$$\delta = A_0P - AP = \sqrt{r^2 + x^2} - s = \frac{(r^2 + x^2) - s^2}{\sqrt{r^2 + x^2} + s} \quad (2.4)$$

r is the distance between A_0 and P_0 and s is the distance between A and P. For a spherical waverfront, $A_0P_0 = AP_0 = r$. Applying cosine rule to triangle P_0AP ,

$$s^2 = r^2 + x^2 - 2rx \cos(90 - \alpha) \quad (2.5)$$

Therefore, $(r^2 + x^2) - s^2 = 2rx \sin \alpha$. Thus,

$$\delta = \frac{2rx \sin \alpha}{\sqrt{r^2 + x^2} + s} \quad (2.6)$$

Note that in lithography, the value for x is in the order of nanometer and r is in the order of centimeter. Thus, x can be neglected. s can be approximated by r and Eq. (2.6) can be written as

$$\delta = x \sin \alpha \quad (2.7)$$

The first minimum in a dark fringe occurs as the OPD equals half of the wavelength divided by refractive index, i.e.

$$\delta = \frac{\lambda}{2n} \quad (2.8)$$

Combining Eq. (2.7) and (2.8),

$$R = x = \frac{\lambda}{2n \sin \alpha} \approx k_1 \frac{\lambda}{\text{NA}} \quad (2.9)$$

This is similar to Eq. (2.1). Hence, Eq. (2.1) is still valid in the regime of high NA immersion lithography.

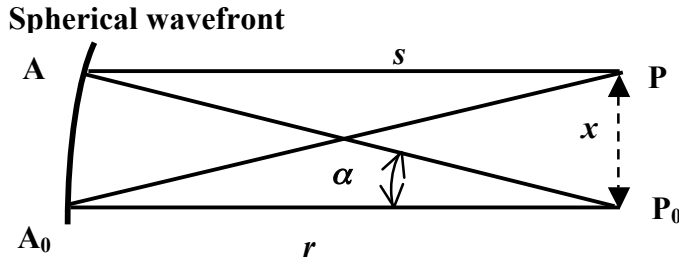


Fig 2.7 Optical path difference (OPD) between on-axis and off-axis light at point P

From Eq. (2.9), the insertion of water between the last lens element and wafer has effectively increased the NA by a factor of n . Therefore, assuming other parameters remain unchanged, the minimum resolvable linewidth has been scaled by a factor of $\frac{1}{n}$.

In terms of water, the refractive index of water is 1.437 at 193 nm exposure wavelength and thus the minimum linewidth is reduced by 28.6 %. It is also noted that the NA of the system is no longer limited to 1. For a lens system that has NA of 0.93 in air, the NA under immersion condition is around 1.34. The implementation of immersion lithography has resulted in a significant improvement in the resolution while keeping the change in infrastructure to a minimal. Thus, immersion lithography has extended the lifetime of 193 nm ArF lithography and enabled continual scaling of dimensions.

Similarly the validity for DOF expression in Eq. (2.2) has also been investigated. The exact OPD δ at point P, which is at a distance z beyond P₀ can be written as (Lin, 2004b)

$$\delta = A_0P - AP = (r+z) - l = \frac{(r+z)^2 - l^2}{(r+z)+l} \quad (2.10)$$

Applying cosine law for triangle P₀AP,

$$l^2 = r^2 + z^2 - 2rz \cos(180 - \alpha) \quad (2.11)$$

Therefore $(r^2 + z^2) - l^2 = 2rz \cos(180 - \alpha)$. Thus,

$$\delta = \frac{2rz(1 - \cos \alpha)}{r+z+l} = \frac{4rz \sin^2 \frac{\alpha}{2}}{r+z+l} \quad (2.12)$$

Since r is much larger than z and l can be approximated by r , $r+z+l \approx 2r$. The distance z

at which OPD equals $\frac{\lambda}{4n}$ is defined as the DOF,

$$z = \text{DOF} = \frac{\lambda}{8n \sin^2 \frac{\alpha}{2}} \quad (2.13)$$

For small angle of α , $\sin \frac{\alpha}{2} \approx \frac{\alpha}{2}$, Eq. (2.13) can be simplified to the form of Eq. (2.2)

$$\text{DOF} = \frac{\lambda}{8n \left(\frac{\alpha}{2}\right)^2} \approx k_2 \frac{\lambda}{n \text{NA}^2} \quad (2.14)$$

However, for larger angle of α , $\sin \frac{\alpha}{2}$ must be evaluated and hence

$$\text{DOF} = \frac{\lambda}{8n \sin^2 \frac{\alpha}{2}} \approx k_3 \frac{\lambda}{n \sin^2 \frac{\alpha}{2}} \quad (2.15)$$

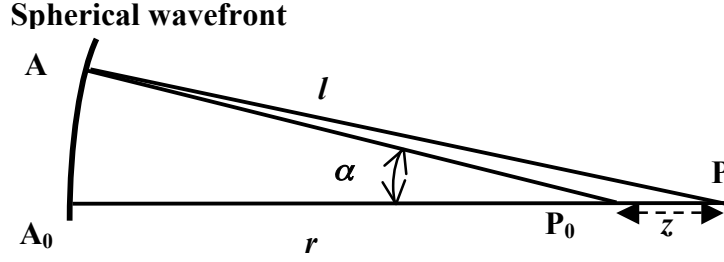


Fig 2.8 Optical path difference (OPD) between on-axis and off-axis light at point P

In Eq. (2.15), k_3 is a process related DOF factor defined for high NA (i.e. $NA > 1$) immersion lithography. For small α , Eq. (2.14) and (2.15) should be equivalent. Hence at small α ,

$$k_2 = 4k_3 \quad (2.16)$$

Thus, for small angle, Eq. (2.14) can represent the DOF. However, for high NA immersion lithography, Eq. (2.15) can represent the DOF more accurately.

From Eq. (2.15), the DOF depends on the inverse of $\sin^2 \frac{\alpha}{2}$ instead of the inverse of $\sin^2 \alpha$. The effect of immersion lithography on DOF of a lithography process can be assessed in two different situations. First, maintaining the same maximum angle as in dry lithography, resolution can be improved by $\frac{1}{n}$. Nevertheless, in pursuing smaller resolution, the DOF is reduced by $\frac{1}{n}$ according to Eq. (2.15). Secondly, keeping the resolution constant, a smaller angle at the lens is needed compared to the dry lithography case. Since a smaller angle is used, the DOF will be improved according to Eq. (2.15).

From the discussion above, the expression for resolution and DOF in high NA immersion regime should be written in the form of Eq. (2.9) and Eq. (2.15). It is seen that the

resolution can be improved by a factor of $\frac{1}{n}$ by implementing immersion lithography.

However, the tradeoff for achieving smaller resolution is the reduction of DOF by a factor of $\frac{1}{n}$.

2.1.4 Imaging problems

2.1.4.1 Process related and haze defects

Mask defect has emerged as one of the most encountered issues in lithography. In general, there are two types of defect: process related defect and progressive defect (or haze). Process related defects are resulted from process errors during mask fabrication. Defects on mask may originate from several sources such as incoming mask blank, writing process, development process, etches process, and the strip process (Kalk et. al, 2000). The types of defects encountered can be classified according to their locations as pinhole, post, clear extension, and dark extension, as shown in Fig. 2.9. Defects result in CD errors and affecting the process windows. One of the technologies to remove mask defects is focus ion beam (FIB) repair method (Gans et. al, 1997). Opaque defects can be repaired by FIB milling which physically sputter etch the defects. For clear defects, FIB induced carbon deposition can be to fill the clear region that is originally dark.



Fig 2.9 Types of defects classified by location: (a) pinhole, (b) post, (c) clear extension, (d) dark extension

Progressive growth of defect (or haze) has emerged as one of the most commonly encountered issues in 193nm projection lithography. Grenon et. al. (2004), Johnstone et. al. (2003), and Bhattacharyya et. al. (2002) have examined the mechanism for haze defect formation through a series of controlled experiments and material characterizations. They have attributed the formation of haze defects to the presence of residues from mask cleaning, out-gassing from pellicle materials and contaminants from environment. The increase in exposure energy and prolonged exposure time with 300 mm wafer has also enhanced the growth of haze defects. A typical occurrence of mask haze defect is shown in Fig. 2.10 (Choi et. al, 2008). The presence of haze defects causes transmission loss (Labovitz et. al., 2008) which in turn affects lithography CD control, process windows and results in the lowering of line yield. As a result, masks have to be inspected and cleaned at regular intervals to remove haze defects (Osborne et. al., 2005).

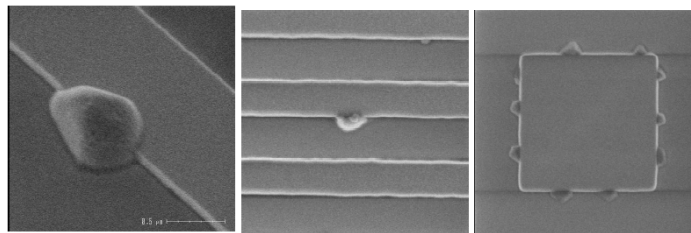


Fig 2.10 Haze defect occurrence on masks

The presence of mask defect is detrimental to lithography process window and CD control. It negates the improvement resulted from application of RET and worse still, as technology node progress to smaller dimensions, the tolerance on defects has become tighter. Defect inspection tools can be used for detecting the location of defects and aerial image measurement system (AIMS) is used to determine changes in aerial image caused

by the defects (Schmid et. al., 2004). However, AIMS are not readily available at all wafer fabs. Thus, understanding of haze defects on printing is helpful in minimizing zealous cleaning and repairing.

2.1.4.2 Forbidden pitch phenomenon in the application of off-axis illumination

Off-axis illumination (OAI) is widely applied in optical lithography for resolution enhancement. It refers to illumination light that is tilted away from the normal incident angle. The diffracted light can still be captured by the projection lens at a smaller pitch. Some common illumination source shapes are shown in Fig. 2.11. This would enable lithography system to resolve smaller feature sizes with ample DOF (Reynolds, 1986 ; Mack, 1989; Asai et.al., 1991; Noguchi et. al. ,1992; Shiraishi et. al., 1992; Ogawa et. al., 1994).

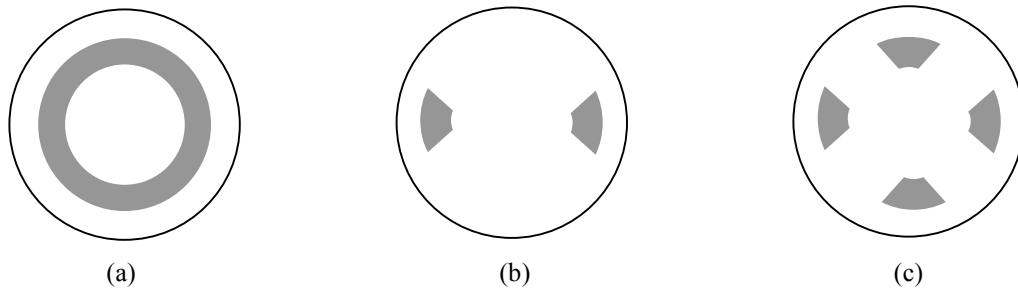


Fig 2.11 Types of off-axis illumination:(a)Annular, (b)Dipole, (c)Quadrupole

In practice, the selections and settings for OAI are often optimized to the smallest pitch in a particular design. However, the setting for one pitch may not be beneficial for other pitches. At certain pitches, diffraction pattern distribution has resulted in a destructive interference due to large phase difference between different diffraction orders. Consequently, image contrast is affected and DOF is often reduced drastically. At such

itches, the CD fluctuation is significant and DOF is often insufficient for processing (Fig. 2.12). Consequently, forbidden pitches have become one of the limiting factors in the design of integrated circuit and are often avoided (Shi et. al, 2002; Smith, 2003).

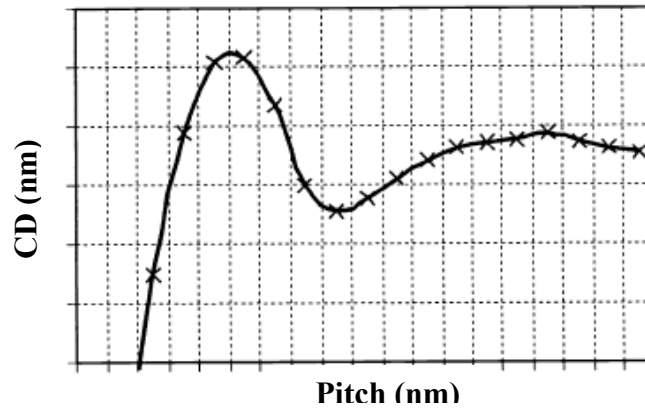


Fig 2.12 A typical CD response over different pitch as a result of application of OAI

Sub resolution assist features (SRAF) can be inserted at some larger forbidden pitch to improve image contrast and DOF (Liebmann, 2003) but it cannot be applied on smaller pitches. The space between smaller pitch features will cause difficulties in the insertion of SRAF during mask fabrication. Double patterning lithography (DPL) or double exposure (DE) can be used to resolve the forbidden pitch issue, but it would result in added manufacturing cost and impose stringent overlay requirement for the tool (Park et. al., 2006).

Source shapes can be optimized by inserting source points in the illumination plane through an iterative process using simulation software. The process is often known as source mask optimization (SMO). Illumination source is first discretized and source points that results in optimum process windows are chosen iteratively. Optimization of mask pattern shape can also be considered during SMO to achieve better process window.

Rosenbluth and Seong (2006) have discussed a SMO approach to achieve optimum process window in which each source point is chosen based on the final image fidelity. Tsujita et. al. (2007) has discussed illumination optimization for conventional source shape or arbitrary source shape. Whilst Brist et. al. (2005) discussed about the interaction between optical proximity correction (OPC) and illumination optimization, and Roy et. al. (2004) proposed a methodology for extending design rules using simultaneous optimization of illumination settings and OPC. However, SMO provides optimized source shapes that are more patterns specific. Thus, the additional cost to manufacture might not be justified. Results from SMO can be used as a guideline to illumination settings for conventional OAI but forbidden pitch effect will occur for conventional OAI.

2.1.4.3 Contact holes patterning challenges

Contact holes patterning has become increasingly challenging as dimension reduces. In the conventional approach to pattern contact holes, reticle with square apertures is used. However, as the dimension of features reduces, the diffracted light from reticle arrives at larger angle at the pupil plane. Since optical lithography is a low-pass frequency filtering process, this has resulted in additional loss of light which degrades the image contrast (Wong, 2001). The current optical proximity correction (OPC) for contact holes patterning includes dimensional biasing and addition of serifs at corners (Saleh and Sayegh, 1981; Ito et. al., 1986; Starikov, 1981). In these methods, the targeted shape for a contact hole is square and OPC features are added in order to ensure a printed contact hole resembles a square as closely as possible. Nevertheless, due to the limit of diffraction, diffracted light is partially filtered out at the pupil plane. As a result, the

printed contact hole would always have rounded corner and appear circular in shape (Jones and Byers, 2003; Burkhardt and Seong, 2003). Even though a square shape is used as targeted shape, the printed pattern will appear circular. Moreover, the printing of side lobes as a result of interaction between higher order light from neighboring features is encountered more frequently (Singh and Mukherjee, 2002; Coles and Somervell, 2006). As shown in Fig. 2.13, as the contact holes pitch reduces, the corner rounding is more significant and printed contact holes appear to be circular. It is also seen that side lobe printing due to interaction between neighboring diffracted light occurs at larger pitch. The process window enhancement by conventional OPC is becoming insufficient. Conventional approach is not fully optimized.

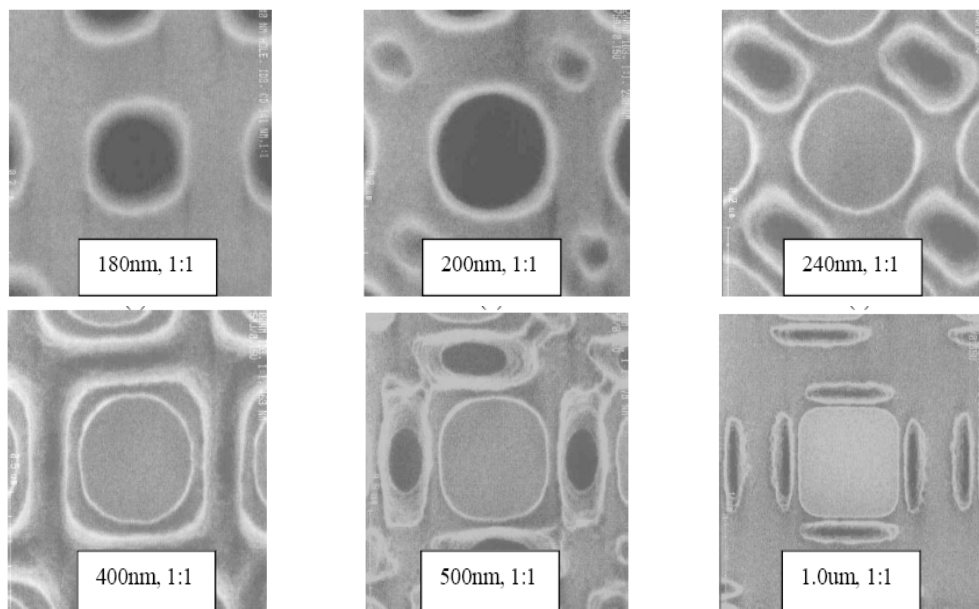


Fig 2.13 Contact holes array of different pitch showing corner rounding and side lobe printing issues

Several methods to further improve process window for contact holes patterning have been proposed. Interference mapping lithography (IML) involves the addition of sub

resolution assist feature at specific location on reticle to mitigate the printing of side lobes (Socha et. al., 2004). Simultaneous optimization of illumination source and mask features for contact holes patterning has also been demonstrated (Socha et. al., 2005; Rosenbluth et. al., 2009). Double patterning approach has been shown to be feasible to achieve dense contact holes array as well (Vanleenhove and Steenwinckel, 2007). However, IML and computational lithography are computationally intensive solutions and are pattern specific, every design need to be considered individually. Moreover, double patterning approach is limited to contact holes in regular array and is challenging to be implemented for random contact holes.

2.2 Resolution enhancement techniques (RET)

Classical resolution of an imaging system is defined by Rayleigh criteria, which states that resolution limit occurs when two of Airy's disks are separated so that the maximum of the neighbour is placed at the first zero of the intensity for the neighbouring feature. In this condition, the separation can be derived as (Airy, 1835; Hecht, 2002)

$$\Delta l = 0.61 \frac{\lambda}{\text{NA}} \quad (2.17)$$

Resolution was defined based on images formed by distant stars, and it was intentional that the image contrast is observable by human eye. In optical lithography, the minimum separation is determined by Eq. (2.9) (Wong, 2001),

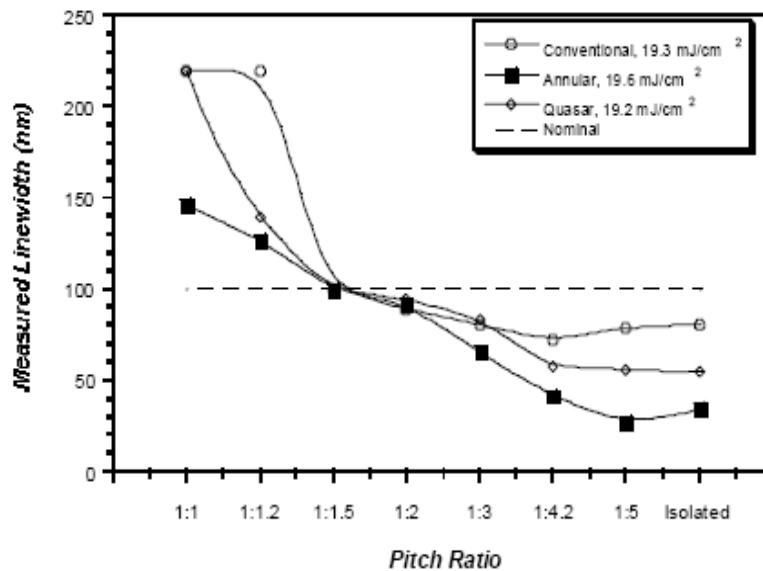
$$R = x = \frac{\lambda}{2n \sin \alpha} \approx k_1 \frac{\lambda}{\text{NA}} \quad (2.18)$$

As mentioned in prior discussions, k_1 represents the process related resolution factor. The benchmark range k_1 in the most current optical lithography process is around 0.3 to 0.4. Hence, optical lithography is capable of achieving resolution that is lower than the classical Rayleigh criteria. Unlike human eye, photoresist in lithography is developed and tuned to have high sensitivity which is capable of amplifying weak image contrast. Lithography system can be optimized by applying manipulations to the optical wavefront such that improvement on image quality can be achieved, the approaches used are collectively known as RET (Brueck and Chen., 1999; Schellenberg, 2005). The components for wavefront include amplitude, phase, and direction. The three main disciplines in RET correspond in controlling these variables: optical proximity correction (or optical and process correction) (OPC) for the wavefront amplitude, OAI for the

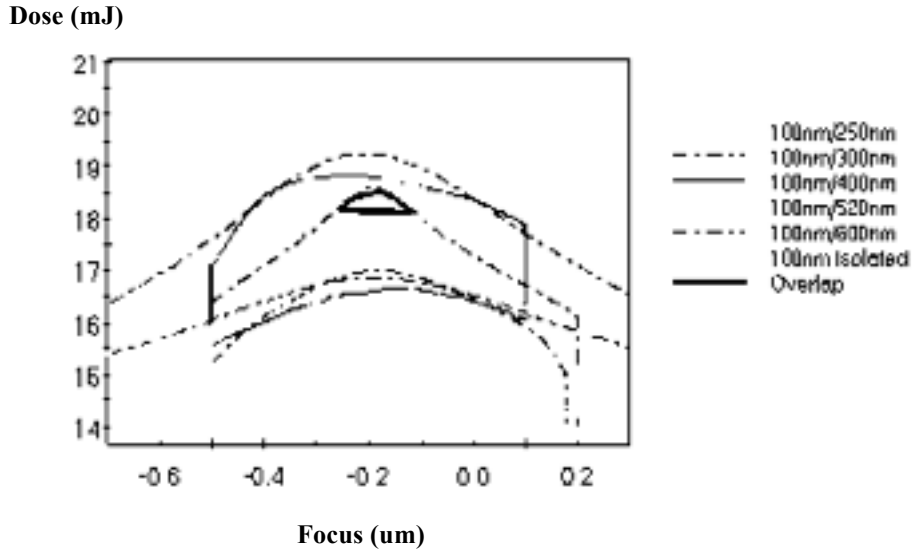
wavefront direction, and phase shifting mask (PSM) for the wavefront phase. Each of these techniques is reviewed.

2.2.1 Optical and process correction (OPC)

The abbreviation “OPC” was initially referred to as optical proximity correction. However, its usage has been extended to layout compensation in optical lithography for other process induced variations in addition to optical proximity effects (Schellenberg, 2004). Optical proximity effects are the variations of linewidth as a function of the proximity of neighbouring features. Due to the interaction between a main feature and its neighbouring features, the printed linewidth between an isolated line and a dense line in a dense array of equal lines and spaces is different (Wong, 2001; Mack, 2008). As a result of this variation, the DOF for features with different pitch is also different. A typical CD and DOF through pitch performance without OPC is shown in Fig. 2.14.



(a)



(b)

Fig 2.14 Optical proximity effects on (a) linewidth and (b) process windows variation

Optical proximity effect does not only affect CD and DOF of one dimensional line and space pattern, it also resulted in similar variation in two dimensional contact holes. Furthermore, corner rounding and line end shortening effects are also observed due to diffraction and frequency filtering of lithography system. Process induced linewidth variations are resulted by microloading effects, wafer stack nonuniformity, exposure tool imperfections, and etc (Lin, 1990; Youn et. al., 1996; Ooishi et. al., 2003; Jensen and Hansen, 2004). Optical and process correction is the technique of pre-distorting mask patterns such that the printed patterns are as close to the desired shapes as possible (Saleh and Sayegh, 1981). Modifications that can be made on mask include selective feature size biasing, fragmentation, and placement of sub resolution assist features (SRAFs) (Chen et. al., 1997; Joesten et. al., 2002).

The difference in CD between targeted and experimentally obtained can be corrected by applying biasing to mask feature. Optically, the optimum exposure dose to produce the

targeted CD for feature with different pitch varies. Exposure dose are usually optimized to the smallest pitch to be patterned. To enable feature of other pitch to be printed correctly under the same dose, biasing by increasing or decreasing mask feature size can be applied. This method is direct and effective in achieving uniform feature size control. However, the drawback is that selective feature size biasing trade exposure latitude with DOF. Effectively, the image quality is not improved. Thus, it is used for patterns with intermediate pitch which do not have sufficient space for insertion of SRAFs.

Line end shortening and corner rounding can be resolved by applying fragmentation method which alters the shape of a targeted feature by moving its edges. This results in the addition of hammerheads or serifs at the line ends and corners, as shown in Fig. 2.15 (Lin, 1990; Liebmann et. al., 1994; Schellenberg et. al.; Mack, 2008). The optimal sizes of hammerheads and serifs depend on several factors such as spacing between neighbouring feature and illumination settings.

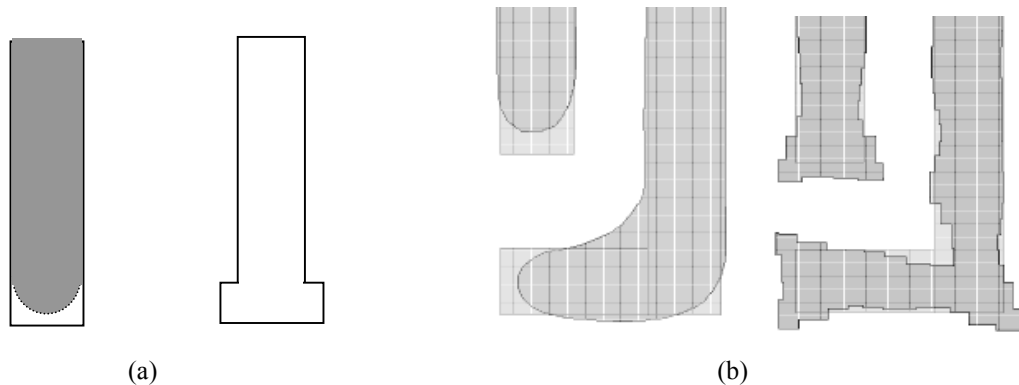


Fig 2.15 Fragmentation method: (a)Hammerhead at line end ; (b)Corner serifs

The insertion of SRAFs is effective in correcting dimension of printed feature. For pattern with line and space, the SRAFs applied are known as scattering bars (SBs). Scattering bar are lines that are smaller than the resolution limit of lithography system.

They are placed adjacent to main feature with larger or isolated pitch size, as illustrated in Fig 2.16 (Garofalo et. al., 1993; Garofalo et. al., 1995; Chen et. al., 1997; Mack, 2008). By doing so, it creates a “dense pitch” environment around the feature with relatively sparse pitch.

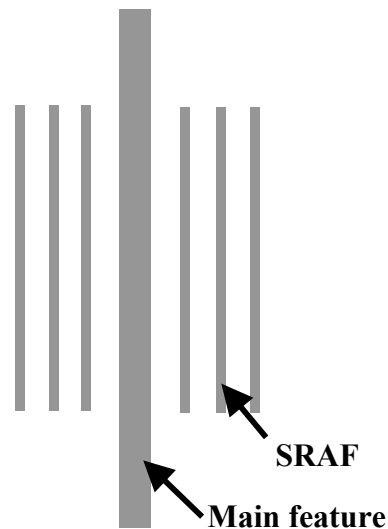


Fig. 2.16 Scattering bars placed adjacent to isolated feature

Since the illumination conditions are optimized for dense pitch, the DOF at isolated pitch can be improved and the difference in desired CD and CD on wafer can be minimized. The proper insertion of SBs requires both experimental and software verification. Factors that need to be considered include illumination settings, mask fabrication accuracy and precaution need to be taken to prevent the printing of assist features. Similarly, SRAFs can also be applied to improve process windows for two dimensional contact holes pattern, as indicated in Fig. 2.17. The placement and sizing of SRAFs can be optimized by aid of computer simulation.

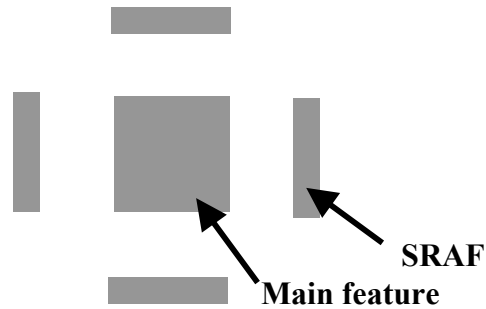


Fig. 2.17 SRAF for contact holes

There are two approaches for OPC: Rule-based OPC, and Model-based OPC. In rule-based OPC, the corrections are implemented in accordance with a set of rules (Otto and Henderson, 1996; Chen et. al., 1997). For one dimensional pattern, the rules can be derived from conducting CD through pitch experiment and interpolating the data to obtain the appropriate biasing values. For two dimensional biasing, the optimum line end treatment and corner serif size are determined empirically. After setting up the rules, corrections are applied through running scripts known as design rule checker (DRC) software package. The application of rule-based OPC is very straight forward and efficient when mask data has small amount of variety. However, the generation of design rules has become a time consuming process for mask pattern with complicated pattern. Moreover, in order to improve the accuracy as technology node moving to smaller dimension, the number of rules increases tremendously. The additional effort to be put in has become unjustifiable. Thus, beyond 130 nm technology node, the accuracy and robustness of rule based OPC degraded. The semiconductor manufacturing industry has then switched to model based OPC for sub 130 nm technology node.

Model based OPC (Waas et. al.,1994; Rieger and Stirniman, 1996; Cobb and Zakhor, 1997; Liu et. al., 1998) implements calibrated lithography models to predict the proximity effects for actual chip pattern. Fragmentation approach is used to move certain edge of a mask feature until the targeted pattern is achieved. The computational requirement of model based OPC approach is heavier than rule based OPC since simulation is required for an entire chip. Thus, the programming architecture of lithography model must be fast and effective in using computing resources. The lithography model includes aerial imaging, resist development and sometimes etch model. The aggressiveness of model based OPC depends on the size of the segments. Smaller segments result in more aggressive OPC but this will contribute to higher mask making cost and computing time.

2.2.2 Off-axis illumination (OAI)

It was found in microscopy that illumination with oblique incident angle is capable of achieving improved resolution. In lithography, illumination with oblique incident angle which significantly reduces or eliminates the normal incident component is known as off-axis illumination (OAI) (Reynolds, 1986; Noguchi et. al., 1992; Asai et. al., 1992; Kamon et. al., 1991; Wong 2001; Mack 2008). The incident angle is effectively tilted from normal, which result in a shift of diffraction pattern from mask at the objective lens. Consequently, diffraction order from smaller pitch can be captured and resolved. The effect of OAI on diffraction pattern is illustrated in Fig. 2.18.

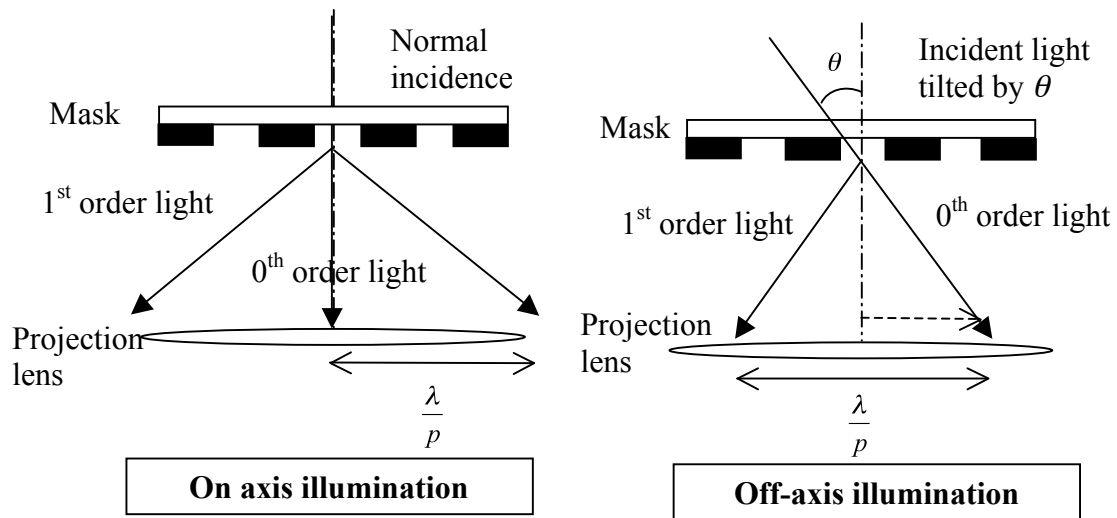


Fig. 2.18 Effect of OAI on diffraction order distribution

Conventional illumination and off-axis illumination shapes are shown in Fig. 2.19. The illumination sources used in lithography are partial coherent illumination in which the light incidents at a range of angle on the mask. Conventional illumination is the most common form of partial coherent illumination. By removing the normal incident component, various shapes of OAI can be derived. The source shapes that are commonly encountered are annular, dipole, and quadrupole.

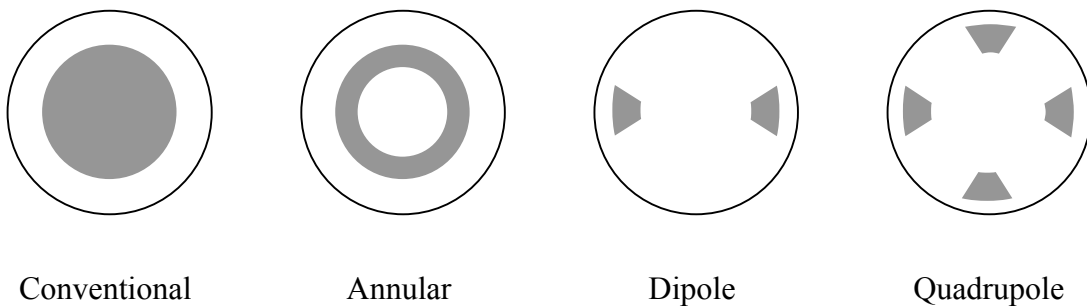


Fig. 2.19 Conventional and off-axis partial coherent illuminations

The illumination settings for OAI are usually optimized to maximize image quality and process window for the smallest pitch. However, this improvement is not for larger and

isolated pitch. The distribution of diffraction order resulted in poorer image contrast and DOF at larger pitch condition. At larger pitch, the image contrast and DOF degradation can be partially restored by inserting SRAFs appropriately. However, as discussed previously, there is a certain range of pitches at which the DOF and CD are extremely poor, known as forbidden pitch. At the forbidden pitch region, the spaces in between features are too narrow for insertion of SRAFs. Consequently, forbidden pitch has to be avoided and it has limited the pitch range that can be patterned.

Each of the OAI source shapes has their advantages and limitations which has to be taken into consideration during the selection of appropriate OAI scheme. Dipole source shape is the simplest form of OAI illumination. It is capable of maximizing the image contrast and DOF for one dimensional pattern (Oriei et. al., 1994; Finders et. al., 2000; Bok et. al., 2002). This is achieved by optimizing the illumination partial coherence settings in order to result in symmetrical distribution of diffraction order at the objective lens. Consequently, better image contrast and DOF can be obtained. However, there are some limitations for dipole OAI. It is highly directional sensitive. A dipole orientated along x-axis can only be optimized to print vertical line and space pattern but will result in poor image for horizontal line and space pattern. Vice versa, y-axis dipole is optimum for horizontal line and space pattern. Nevertheless, dipole is suitable for the patterning of high density one dimensional line and space pattern in the memory industry such as DRAM or flash memory devices.

Quadrupole source shape consists of four poles that are placed to achieve equivalent imaging enhancement for both horizontal and vertical pattern (Ogawa et. al., 1994; Watson et. al., 1998). The four poles are evenly spaced about the center and they produce

diffraction pattern that is beneficial in both directions. Apart from line and space pattern, quadrupole illumination can also be optimized for patterning of regular contact holes array. Nevertheless, for line and space array orientated along 45 degree, quadrupole illumination will not be effective. This is because there will be two poles that is parallel to the orientation of the feature which result in diffraction distribution that degrades image contrast and DOF.

Both dipole and quadrupole source shapes are orientation dependence and is not suitable for pattern with various orientations. Annular source shape which consists of a ring is directionally insensitive and thus capable of enhancing image contrast and DOF for pattern with different orientations (Reynolds, 1986; Kamon et. al., 1991). This is because annular source shape is radial symmetric and hence it provides equivalent enhancement regardless of orientation. However, the penalty is that annular illumination has introduced additional background light due to its larger area compare with dipole and quadrupole, which sacrifices the image contrast and DOF slightly. Despite this drawback, annular illumination is preferred because the orientation of patterns is not limited to certain direction in practice.

2.2.3 Phase-shifting mask (PSM)

Conventional chrome-on-glass (COG) mask has binary mask transmittance with light transmitted 100 % through the quartz areas and blocked completely by the chrome areas. Binary-intensity mask modifies only the amplitude of light passes through it, the mask transmission function is therefore defined only by 0 or 1 (Wong, 2001; Mack 2008). Phase-shifting mask is designed to modify both amplitude and phase of light of the

transmitted light. Phase difference can be created through difference in the quartz thickness, as shown in Fig. 2.20 below.

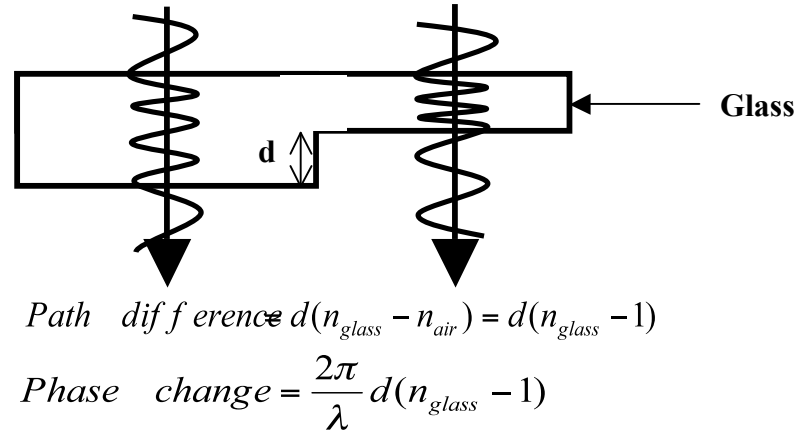


Fig. 2.20 Phase difference due to thickness difference of d

When two light rays pass through different thicknesses of the mask, they experience different optical path lengths which result in phase difference between them. The phase difference can be controlled by varying the quartz thickness. Phase difference between light that passes through nearby region of the mask is:

$$\Delta\phi = \frac{2\pi d}{\lambda}(n_g - 1) \quad (2.19)$$

If the phase difference is 180° , light travels through neighbouring feature will interfere destructively. Destructive interference cancels the electric field amplitude and the region where it occurs is completely dark. The concept of PSM is based on destructive interference for improvement in image contrast. For a COG mask, the space between neighbouring lines does not contain region that is completely dark due to lack of phase interaction. Thus, the aerial image resulted from PSM has larger difference between maximum and minimum image intensity and is more robust than that of a COG mask.

The improved image contrast and robustness of PSM has enabled patterning of features with smaller pitch. There are two forms of PSM (Levenson et. al., 1982, 1984; Prouty and Neureuther, 1984; Nitayama et. al., 1989; Terasawa et. al., 1991; Schellenberg et. al., 1992) that are commonly used in lithography: Alternating phase-shifting mask (AltPSM) and Attenuated phase-shifting mask (AttPSM).

The cross section of an AltPSM for equal line and space pattern is shown in Fig. 2.21. Two neighbouring lines are covered with glass of different thickness. The difference in thickness will induce a 180° phase-shift between light that passes through these two lines.

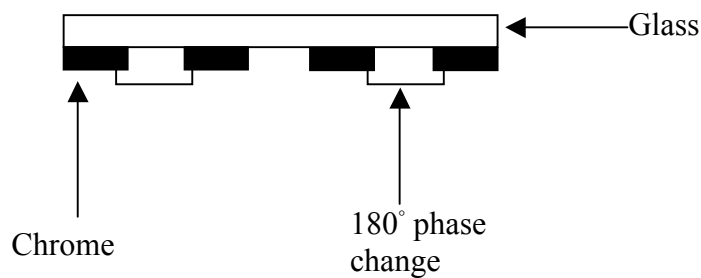


Fig. 2.21 Alternating phase-shifting mask (AltPSM)

Due to the phase-shift, the diffraction pattern collected from an AltPSM will not contain 0^{th} order and other even order light. Under this condition, only $\pm 1^{\text{st}}$ order light is collected and thus resulted in two-beam interference. $\pm 1^{\text{st}}$ order will distribute symmetrically about the center of projection lens. Thus, the optical path length when $\pm 1^{\text{st}}$ order travel towards the wafer surface is always equal. The DOF will be improved through application of AltPSM. Alternating phase-shifting mask can be used for printing of dense line and space pattern due to its enhanced process window and superior image contrast.

Nevertheless, there are a couple of implementation issues that is concerned with AltPSM: phase conflicts, and phase and intensity imbalance. There are two types of phase conflicts, as seen in Fig. 2.22.

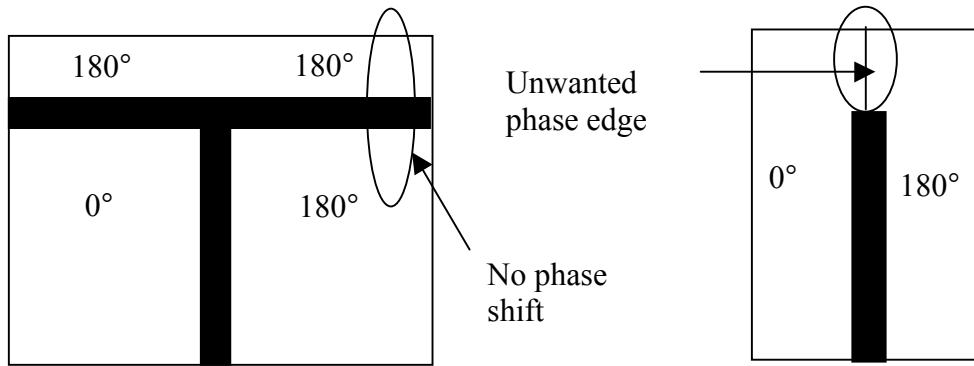


Fig 2.22 Phase conflicts in application of AltPSM

The first type is a lack of phase shift across a critical feature when there is an odd wrapping of phase assignments. The second type is known as termination problem which occurs at the end of a line, which results in the printing of undesired dark line. The solution for phase conflicts is not straightforward. A design that is modified to accommodate application of AltPSM can be adopted but it would require some design trade offs. Alternatively, a double exposure process can be used. The first exposure involves patterning of critical features and the second exposure is for the patterning of non critical features. However this would increase the cost significantly as two masks are required and double exposure process lowers the throughput. Intensity and phase imbalance is resulted by the etched quartz thickness which resulted in phase shift error if the etching is non uniform and additional diffraction as light passes through the etched region. This problem can be resolved by dual trench approach by etching both phase

shifted and unshifted region, by undercut etch to allow additional light through the widened space, or by biased space approach which enlarge the phase shifted region.

The cross sectional view of an AttPSM is shown in Fig. 2.23. It features much resemblance of COG mask but the opaque region is replaced by partially transmitting phase shifting material. The partially transmitting region normally consists of Molybdenum silicide (MoSi) with 6 % transmission and 180 ° phase change. Compared with COG mask, AttPSM is capable of producing sharper transition of the image due to phase interaction effect. Thus, process latitude improvement can be achieved. However, the improvement of image quality for dense pattern by AttPSM is not as much as AltPSM because there is some amount of background light in between neighbouring features. In addition, the diffraction order of AttPSM contains zero order light because it is not cancelled by light from neighbouring feature.

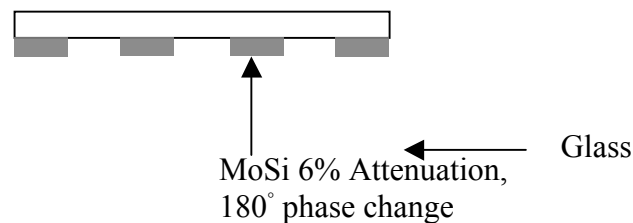


Fig. 2.23 Attenuated phase-shifting mask (AttPSM)

The advantage of AttPSM over AltPSM is the simplicity and low cost of replacing COG mask. There is no additional etching process in mask manufacturing as encountered in AltPSM fabrication. In addition, due to similarity between COG and AttPSM, minimal effort in modifying design to enable its application is needed. Furthermore, AttPSM has no issue of phase conflicts of AltPSM. With proper optimizations such as insertion of

SRAF and adoption of OAI, AttPSM is capable of achieving sufficient enhancement to process latitude. Thus, AttPSM has been widely used in critical lithography layers currently.

Nonetheless, the most common issue experienced in application of AttPSM is the formation of sidelobes (Hsu et. al., 2005). The interference between light from space and the phase shifted region cancels out near the space edge and resulted in zero image intensity which improves the image contrast. However, light diffracted from the non phase shifting might interfere constructively and form sidelobes between features. The printing of unwanted sidelobes is detrimental to line yield and result in failure of the chip functioning normally. Sidelobes printing issues can be strategically placing assist slots, the methodology applied is known as interference mapping lithography (IML).

2.2.4 Advanced resolution enhancement techniques

While the development of next generation lithography techniques is slower than expectation, the semiconductor industry is developing intermediate solutions which are capable of enabling the progress of Moore's law. There are several advanced resolution enhancement techniques that have shown the potential of pushing smaller resolution limit. These advanced RET can be categorized as: Double exposure and double patterning approach, Computational lithography approach, and alternative assist features.

In a double exposure process, the pattern of a critical layer is formed by two or more exposures steps (Hsu et. al., 2004, 2006; Lee et. al., 2008). A critical layer which contains pattern that is beyond resolution limit of single exposure process is split into two or more masks. A wafer to be patterned will be exposed using both masks. The latent

image formed at resist will be the sum of image from both masks, as shown in Fig. 2.24. Using double exposure method, the resolution limit of single exposure process can be overcome. One of the major challenges in double exposure process is in the photo resist. During the first exposure, some of the unexposed area is partially exposed due to background light coming from a nearby feature and it is known as resist memory effect. As a result, the resolution limit of double exposure approach cannot be lower than k_1 of 0.25. Other issues that have to be addressed in double exposure approach are the stringent requirement for accurate overlay control, effective methodology of pattern splitting, and increase in mask cost due to requirement for additional masks.

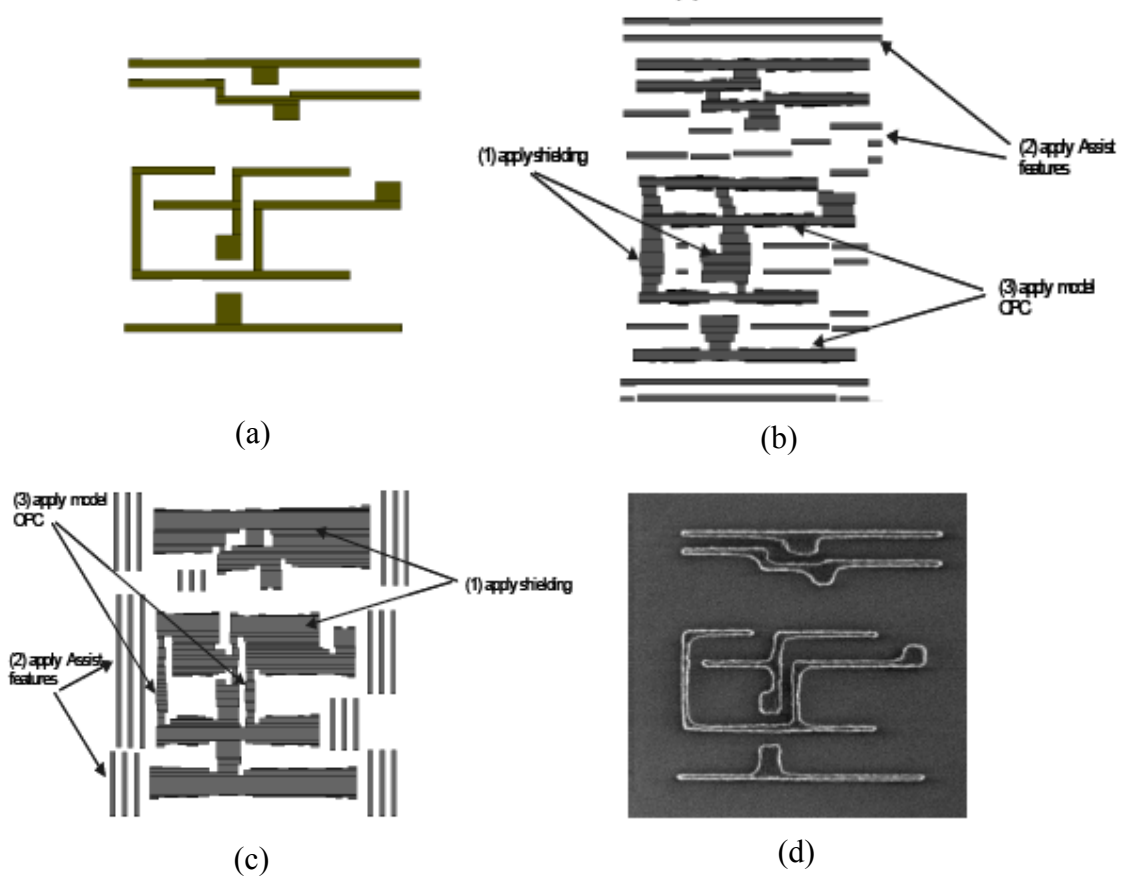
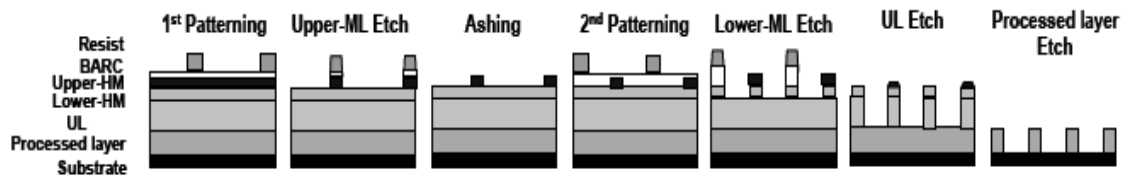
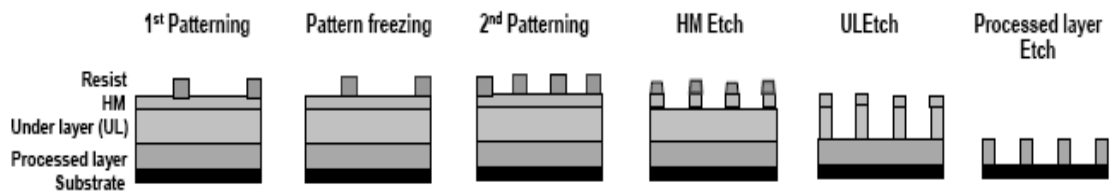


Fig. 2.24 Illustration of a double exposure process: (a) design, (b) first exposure mask, (c) second exposure mask, (d) printed pattern on wafer

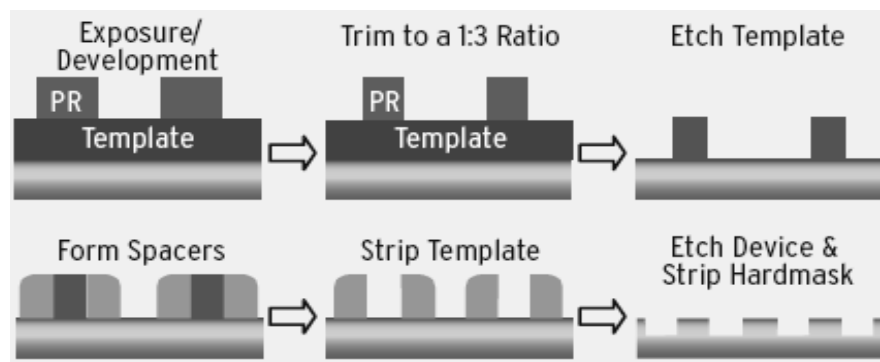
Double patterning approach achieved the desired pattern by two exposure processes. The difference between double patterning and double exposure is that in double patterning, there is an intermediate pattern transfer step between the two exposures (Terai et. al., 2008; Erdmann et. al., 2010; Koay et. al., 2010; Wong et. al., 2010). This additional step has overcome the resist memory effect in double exposure approach. Hence, the potential resolution limit of double patterning approach is below k_1 of 0.25. There are several different processes in double patterning approach, as shown in Fig 2.25.



(a)



(b)



(c)

Fig. 2.25 Typical double patterning processes: (a) Litho-etch-litho-etch (LELE), (b) Litho-freeze-litho-etch (LFLE), and (c) Self aligned double patterning (SADP)

In the litho-etch-litho-etch (LELE) process, the wafer is first exposed and developed. The developed image is then used to etch into a hardmask stack, the stack provides intermediate pattern transfer. Subsequently, the wafer is then recoated with photoresist and second pattern is exposed. Similarly, the second pattern is then transferred to the hardmask. The final image is then transferred to the underlying layer. For litho-freeze-litho-etch (LFLE) process, the image formed in photoresist after first exposure is subjected to a “freezing” process. Subsequently, second layer of resist is coated and second exposure and development are carried out. Finally, the resultant image is transferred to the underlying layer. Unlike LELE process, the LFLE process does not contain an intermediate pattern transfer step. Self align spacer double patterning (SADP) consist of only single exposure step. A sacrificial gate is formed at the beginning. Subsequently, spacers are deposited on both sides of the sacrificial gate. The sacrificial gate is then chemically removed. Finally, image is transferred from the spacer hard mask to the underlying layer.

The resolution limit of lithography process can be further stretched via a thorough optimization through intensive mathematical algorithm, known as computational lithography. Researchers have demonstrated possibility of achieving low k_1 patterning using computational lithography approach. Pixelated phase shift mask is one of the resultant approaches through application of computational lithography. The improvement is achieved by using a sophisticated mask model and allowing mask feature to be described in pixel form, as shown in Fig. 2.26.

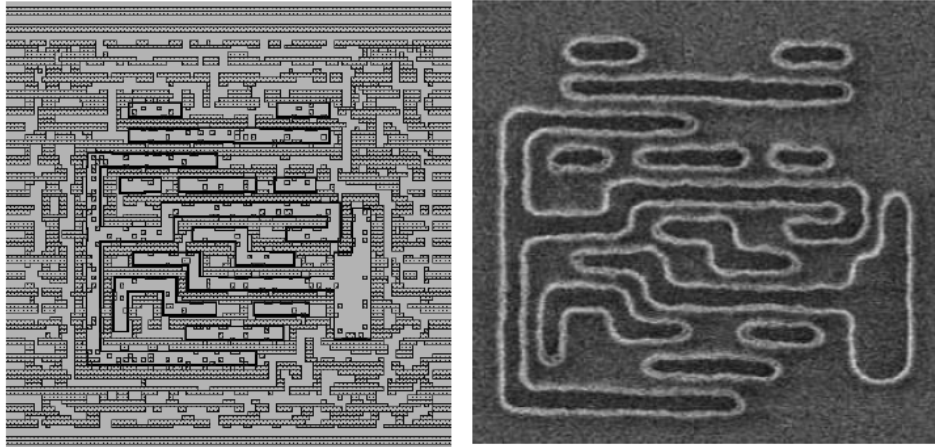


Fig. 2.26 Pixelated mask for advanced logic patterning

Source mask optimization (SMO) is another approach of computational lithography (Singh et. al., 2007, 2008; Deng et. al., 2010; Melville et. al.,2010). Essentially, SMO is the process of simultaneous optimization of illumination source and mask features. The illumination source resulted from optimization can be a freeform illumination source, as seen in Fig. 2.27. The segmentation of mask is done simultaneously with source optimization to enable optimal imaging performance.

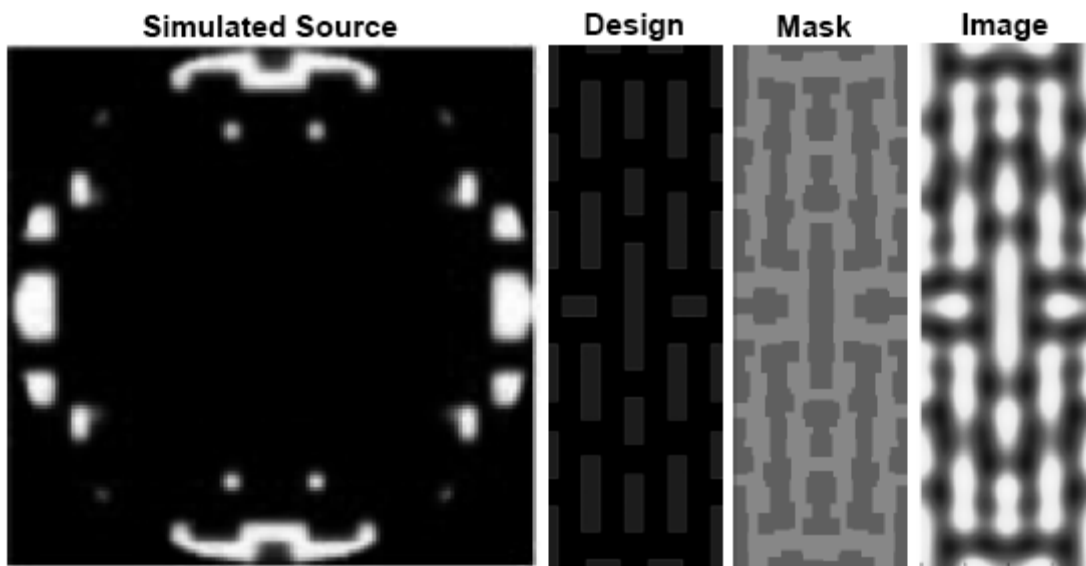


Fig. 2.27 Free form illumination based on source mask optimization

Apart from the above mentioned methods, researchers are looking at alternative assist features for resolution enhancement. Evanescent wave assist feature is one of the latest approaches for resolution enhancement (Lafferty et. al., 2007). By strategically positioning assist feature in sub wavelength period near the main feature, the evanescent wave at interface is guided towards the mask opening and help in improving image contrast (Fig. 2.28).

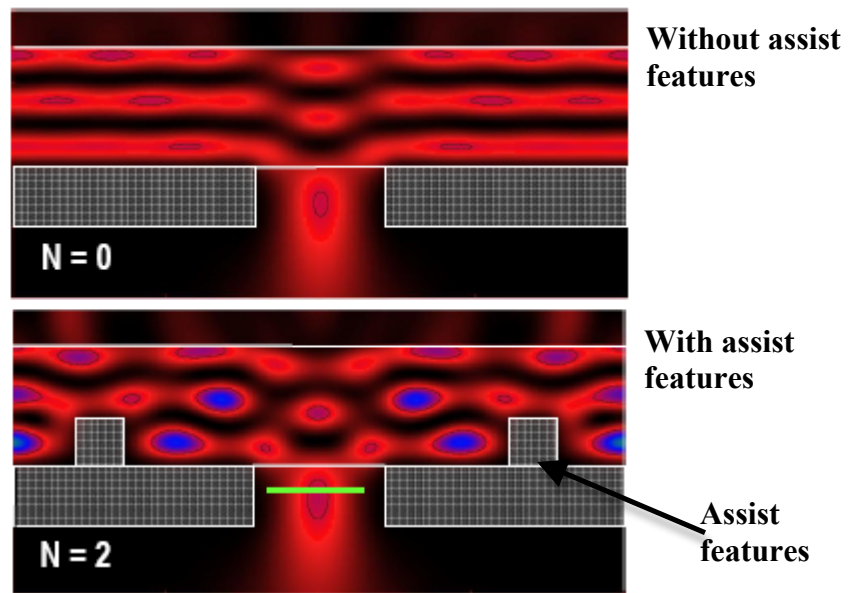


Fig. 2.28 Schematic diagram of evanescent wave assist features

2.3 Optical imaging theory

2.3.1 Fraunhofer diffraction

Diffraction of light is the fundamental phenomenon that is responsible for image formation in optical lithography. Generally, the deviation of light from rectilinear propagation is known as diffraction (Hecht, 2002). Diffraction can be accounted for by considering the wave nature of light. In 1690, Dutch physicist Christian Huygens first described the interpretation of physical principle in his Treatise on Light. This has become the famous Huygens' principle: every point in a propagating wave front serves as the source of spherical secondary wavelets, such that the wave front at some later time is the envelope of these wavelets, as shown in Fig. 2.29 (Goodman, 1996). Huygens' principle is independent of wavelength considerations. In 1818, Augustin Jean Fresnel had later added the concept of interference discovered by Thomas Young into the original Huygens principle. Huygens-Fresnel Principle states that every unobstructed point of a wavefront, at a given instant, serves as a source of spherical secondary wavelets with the same frequency as that of primary wave. The amplitude of the optical field at any point beyond is the superposition of all these wavelets considering their amplitudes and relative phases.

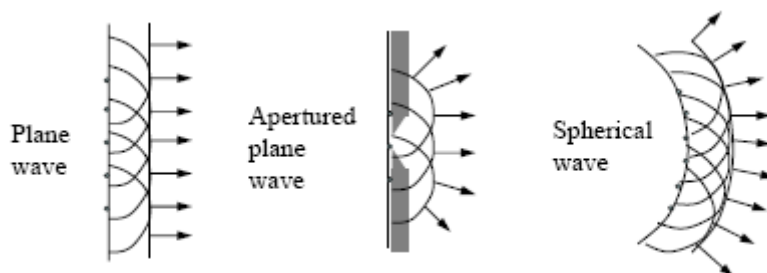


Fig. 2.29 Illustration of Huygens' principle

Following Huygens-Fresnel Principle, the occurrence of diffraction depends on the relative size of aperture. When the wavelength of incident light is in the order of aperture, the unobstructed point in the aperture acts as secondary source and the waves will spread out at large angles into the region beyond obstruction. If the incident wavelength is much smaller than the aperture, diffraction effect can only be observed within a short distance behind the aperture and beyond this region, shadow begins. The phase differences for secondary wavelets will be too large for constructive interference to occur. Thus only dark region can be observed after some distance behind the aperture. This explains the occurrence of shadow when light ($\lambda \approx 400 - 700 \text{ nm}$) is shined on a lamp post but when sound wave ($\lambda \approx 60 \text{ cm}$) passes through lamp post, it would bend.

In 1860, Maxwell identified light as an electromagnetic wave and formulated the vector equations for describing the behaviors of light as well as other form of electromagnetic waves. the ideas of Huygens-Fresnel Principle were then put on a firmer mathematical foundation by Gustav Kirchhoff, with two assumptions about the boundary conditions of the light incident on the surface of aperture. Kirchhoff's formulation is the first approximation to describe diffraction phenomenon mathematically and has yield amazingly accurate results compared to experimental observations. However, there are some internal inconsistencies in the assumptions which were proven by Poincare in 1892 and Sommerfeld in 1894. Sommerfeld eliminated the assumptions that resulted in inconsistencies by applying the theory of Green's function. This is so called the Rayleigh-Sommerfeld diffraction theory. Based on two different approximations to the distance between point of observation and diffraction aperture, diffraction pattern observed can be classified as Fresnel (near-field) and Fraunhofer (far-field) diffraction, as

shown in Fig. 2.30. For optical lithography, diffraction in the Fraunhofer or far-field region needs to be considered.

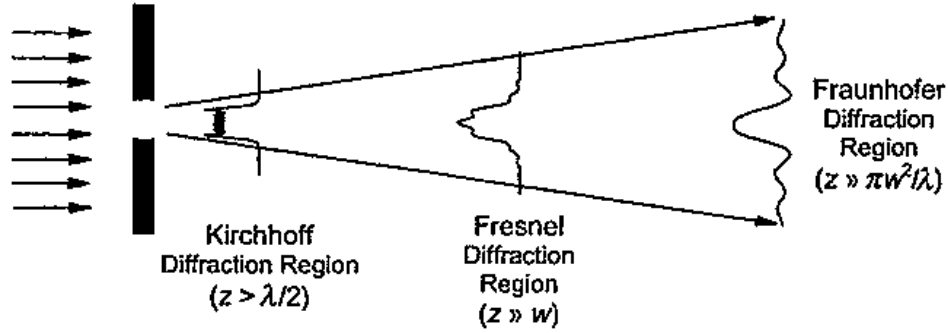


Fig. 2.30 Diffraction zone depends on distance from the slit

Fraunhofer diffraction integral can be expressed as:

$$M(f_x, f_y) = \int_{-\infty}^{\infty} \int_{-\infty}^{\infty} E_i(x, y) m(x, y) e^{-i2\pi(f_x x + f_y y)} dx dy \quad (2.20)$$

$E_i(x, y)$ is the electric field of the light incident on the mask, which is 1 if a unit amplitude normally incident plane wave is considered (Mack, 2008). $m(x, y)$ is mask transmission function. Mask transmission is the electric field distribution directly under the mask. Binary intensity mask is transparent at glass and fully opaque at chrome, thus $m(x, y)$ is 1 under the glass and 0 under the chrome. f_x and f_y are the spatial frequencies for x and y direction respectively. $M(f_x, f_y)$ is the mathematical expression of diffraction pattern result at the Fraunhofer diffraction region.

2.3.2 Fourier optics for aerial image formation

Eq. (2.20) is the Fourier transform of the mask function. Thus, the diffraction pattern (which is the electric field distribution as it enters the projection lens) is the Fourier transform of the mask pattern transmission. Fourier transform operation can be represented by F and the Fraunhofer diffraction pattern can be expressed as

$$M(f_x, f_y) = F\{E_i(x, y)m(x, y)\} \quad (2.21)$$

Fig. 2.31 shows the common Fourier transform pairs that are useful in lithography (Smith and Sheats, 1998).


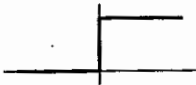


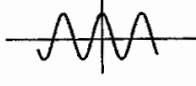
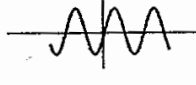
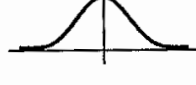
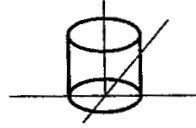
$g(x)$	Graph of $g(x)$	$G(f_x)$
$rect(x) = \begin{cases} 1, & x < 0.5 \\ 0, & x > 0.5 \end{cases}$		$\frac{\sin(\pi f_x)}{\pi f_x}$
$step(x) = \begin{cases} 1, & x > 0 \\ 0, & x < 0 \end{cases}$		$\frac{1}{2}\delta(f_x) - \frac{i}{2\pi f_x}$
Delta function $\delta(x)$		1
$comb(x) = \sum_{j=-\infty}^{\infty} \delta(x - j)$		$\sum_{j=-\infty}^{\infty} \delta(f_x - j)$
$\cos(\pi x)$		$\frac{1}{2}\delta\left(f_x + \frac{1}{2}\right) + \frac{1}{2}\delta\left(f_x - \frac{1}{2}\right)$
$\sin(\pi x)$		$\frac{i}{2}\delta\left(f_x + \frac{1}{2}\right) - \frac{i}{2}\delta\left(f_x - \frac{1}{2}\right)$
Gaussian $e^{-\pi x^2}$		$e^{-\pi f_x^2}$
$circ(r) = \begin{cases} 1, & r < 1 \\ 0, & r > 1 \end{cases}$ $r = \sqrt{x^2 + y^2}$		$\frac{J_1(2\pi\rho)}{\pi\rho}$ $\rho = \sqrt{f_x^2 + f_y^2}$

Fig. 2.31 Common Fourier transform pairs

The transmission function of mask patterns can be found by convolution. For example, transmission for a one dimensional line and space patterns can be found by convolution of an isolated line with line width equal to mask critical dimension (CD) and a comb function with period equals to mask pitch. Critical dimension (CD) is defined as the line width of the feature. Pitch is defined as the sum of line width and space width for a repeating pattern, it is period of the patterns. The convolution theorem for Fourier transform:

$$F \left\{ \iint g(\xi, \eta) h(x - \xi, y - \eta) d\xi d\eta \right\} = G(f_x, f_y) H(f_x, f_y) \quad (2.22)$$

$G(f_x, f_y)$ and $H(f_x, f_y)$ are the Fourier transform for $g(x, y)$ and $h(x, y)$ respectively.

Therefore, the Fourier transform for a convolution of two functions is the just the multiplication of each individual transforms. Hence, diffraction for some common mask patterns can be obtained by appropriate combination of functions listed in Fig. 2.31. For example, the mask function $m(x)$ for one dimensional line and space patterns with line width d and pitch p is the convolution of a *rect* function and a *comb* function: (Airy, 1835)

$$m(x) = \text{rect}(x/d) \otimes \sum_{n=-\infty}^{\infty} \delta(x - np) \quad (2.23)$$

Fourier transform for $m(x)$ can be found with reference to Fig. 2.31:

$$M(f_x) = F\{m(x)\} = \frac{d}{p} \sum_{n=-\infty}^{\infty} \text{sinc}(\pi d f_x) \delta\left(f_x - \frac{n}{p}\right) \quad (2.24)$$

In Eq. (2.25), it can be seen that the diffraction pattern distribution is discrete, defined by the delta function $\delta(f_x - \frac{n}{p})$ and n is integer. n is known as the diffraction order. As pitch becomes smaller, the diffraction order will become more spread out at the diffraction plane before diffracted light enter the projection lens. As shown in Fig. 2.32, light passes through the mask will be diffracted and travels towards the projection lens. The size of the projection lens is limited and there will be some maximum angle of diffraction θ_{\max} beyond which the light will not be captured by the lens. A convenient way to represent the size of lens is by numerical aperture (NA), defined as multiplication of refractive index of surrounding medium n and the sine of the maximum half-angle of diffracted light that can enter the lens $\sin \theta_{\max}$.

$$NA = n \sin \theta_{\max} \quad (2.3)$$

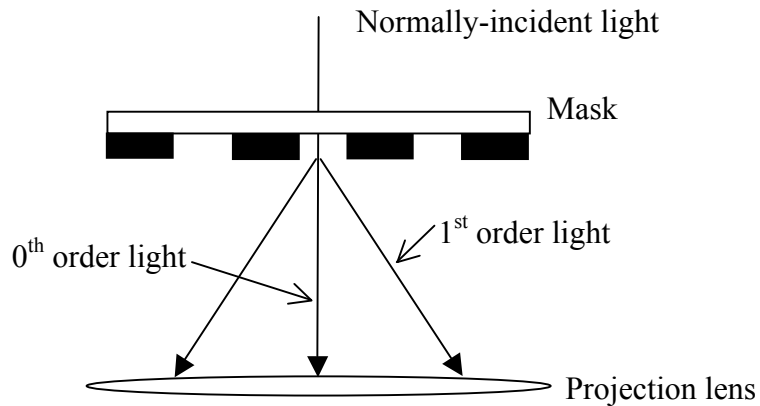


Fig. 2.32 Diffraction of light passing through mask collected at projection lens

As shown in Fig. 2.33, spatial frequencies f_x and f_y can also be defined as

$$\begin{aligned} f_x &= \frac{\sin \theta_x}{\lambda} = \frac{x}{\lambda z} \\ f_y &= \frac{\sin \theta_y}{\lambda} = \frac{y}{\lambda z} \end{aligned} \quad (2.25)$$

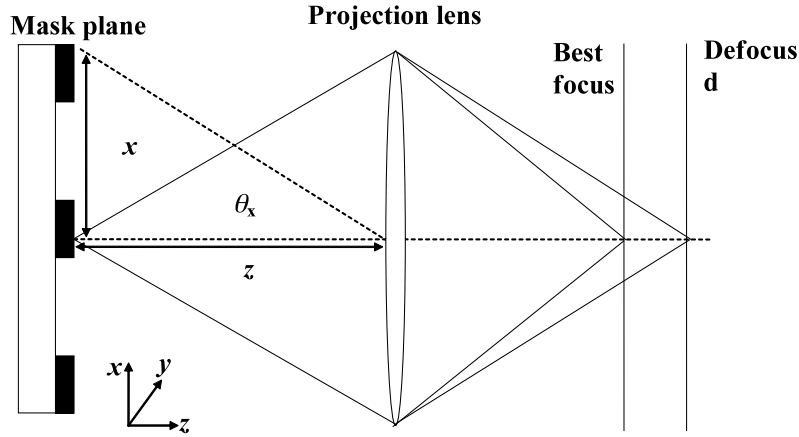


Fig. 2.33 Definition of spatial frequencies in relation with lithography system

Numerical aperture is an important parameter for determining the smallest pattern an imaging system can define. More diffracted light will be captured for a lens with larger NA and smaller pitch can be resolved. The projection lens collects diffraction pattern from mask and performs inverse Fourier transform for image reconstruction at the wafer plane. Therefore, the electric field $E(x', y')$ at wafer plane can be expressed as:

$$E(x', y') = F^{-1} \{M(f_x, f_y)P(f_x, f_y)\} \quad (2.26)$$

F^{-1} is the symbol for inverse Fourier transform operation. $P(f_x, f_y)$ is the pupil function

for projection lens system defined by

$$P(f_x, f_y) = \begin{cases} 1 & \text{if } \sqrt{f_x^2 + f_y^2} < \frac{\text{NA}}{\lambda} \\ 0 & \text{if } \sqrt{f_x^2 + f_y^2} > \frac{\text{NA}}{\lambda} \end{cases} \quad (2.27)$$

The above pupil function is that for ideal lens function and it has the behavior of a low-pass filter. Spatial frequencies beyond that of $\frac{NA}{\lambda}$ will not be captured through the projection lens. Substituting Eq. (2.24) and (2.27) into Eq. (2.26) will yield the electric at wafer plane a one dimensional line and space pattern:

$$E(x') = \frac{d}{p} \sum_{n=-\infty}^{\infty} \text{sinc}\left(\frac{\pi nd}{p}\right) e^{i\frac{2\pi nx}{p}} \quad (2.28)$$

In Eq. (2.28), it can be seen that the resulting image is a summation of diffracted light. When n is 0, there is no variation in amplitude of the electric field and thus resulted in a constant electric field and no image is formed. In order to form an image, the projection lens has to captured at the least zero order and first order light.

Image intensity is the square of electric field:

$$I(x') = |E(x')|^2 = \left| \frac{d}{p} \sum_{n=-\infty}^{\infty} \text{sinc}\left(\frac{\pi nd}{p}\right) e^{i\frac{2\pi nx}{p}} \right|^2 \quad (2.29)$$

2.3.3 Partial coherent imaging theory

Coherent illumination is assumed in previous discussion. For coherent illumination, light incident on mask in only one direction. However, actual lithography tools use a more complicated illumination, which light strikes the mask from a range of angles. This illumination is known as partial coherent illumination. In order to characterize the range of angles a partial coherent illumination contains, the partial coherence factor σ is often used. σ is defined as the condenser lens NA (sine of the half angle of the illumination cone) divided by the projection lens NA (Lin, 1980; Wong, 2001; Mack, 2008):

$$\sigma = \frac{NA_{\text{condenser lens}}}{NA_{\text{projection lens}}} = \frac{\text{source diameter}}{\text{lens diameter}} \quad (2.30)$$

For a partially coherent light source, the angle of incident is tilted from normal incidence. The effect is a shift of diffraction pattern in spatial frequencies domain with respect to the projection lens aperture. Refer to Fig. 2.34, if the angle of incidence on mask is θ' the diffraction pattern would shift by $f_x' = \sin \theta' / \lambda$. Partial coherent illumination enables the capture of diffraction order from smaller pitch mask pattern compare to coherent illumination. As shown in Fig. 2.35, for the case of on-axis coherent illumination, the first order light cannot be captured by the projection lens and the pitch is not resolvable. However, for partial coherent illumination, since the diffraction pattern is shifted, part of the first order light is captured and the pitch can be resolved. It can also be seen from Fig. 2.35 that the diffraction pattern for a partial coherent illumination is broaden since the illumination consist of a range of angle of incidence compare to a single point source from that of a coherent illumination.

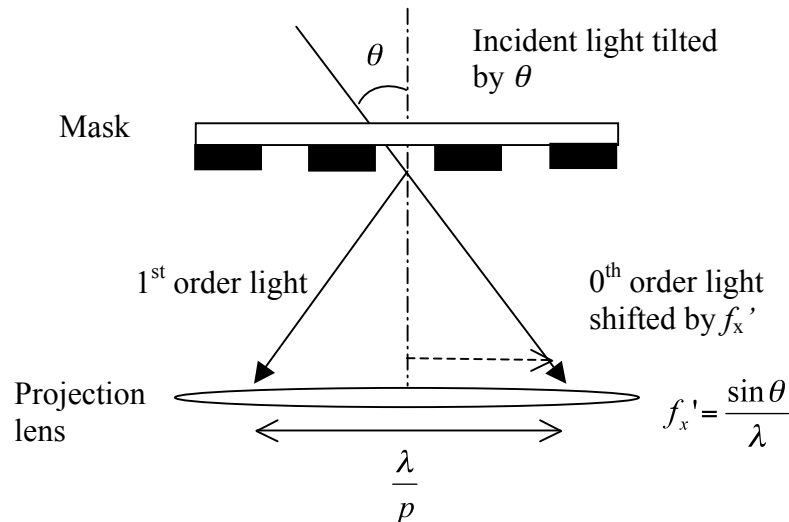
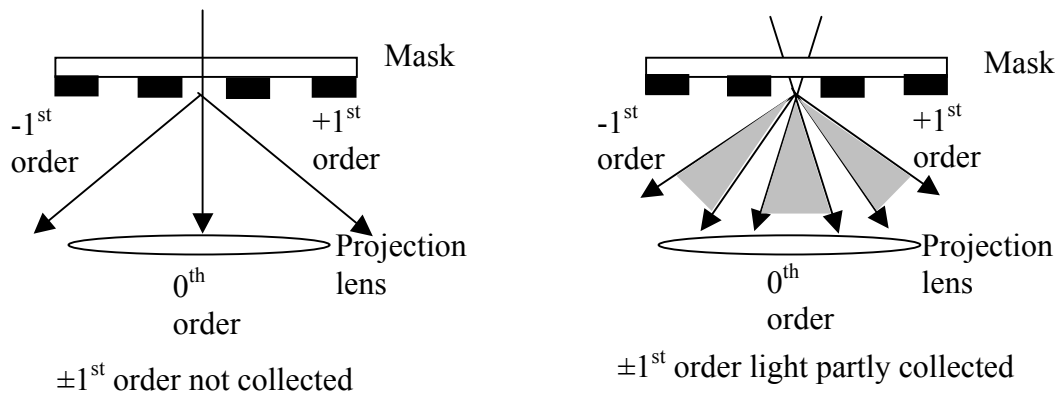


Fig. 2.34 Effect of tilted incident light on the distribution of diffraction order



Coherent illumination

Partial coherent illumination

Fig. 2.35 Diffraction order distribution for coherent and partial coherent illuminations

The application of partial coherent illumination has reduced the theoretical resolution limit of a lithography system. In the extreme case, the zero order and first order passes through the two opposite edges of projection lens:

$$p = \frac{\lambda}{2NA} \tag{2.31}$$

Assume equal line and space,

$$R = 0.25 \frac{\lambda}{NA} \tag{2.32}$$

Therefore, in partial coherent imaging, the theoretical resolution limit is half of that of coherent imaging.

Köhler illumination uses the condenser lens to form an image of the source at the entrance of projection lens. The mask is placed just behind the condenser lens exit pupil (the image of lens aperture seen from the image on plane). This arrangement has ensured that all diffraction pattern produced by a mask will be projected to the same spot at the entrance of projection lens. It has also provided uniform image intensity all over the mask.

An arbitrary partial coherent illumination shape can be described as extended source, where the source shape is divided into a collection of individual point sources. Each point source is a spatially coherent illumination and the image resulted from each point source at the wafer plan can be found by Eq. (2.28). Two point sources from a partially coherent light source do not interact coherently with each other. The resultant image from two or more point sources can be considered by adding the contribution from each point source incoherently.

In general, there are two approaches in considering partial coherent imaging. The first method is known as Abbe's method (Abbe, 1873). According to Abbe's method, the image is determined by calculating the coherent aerial image from each point on the source and then integrating the intensity over the source. For a partial coherent source with intensity at each point described by source function $S(f_x', f_y')$, the image can be found by (Mack, 2008):

$$I_{Total}(x, y) = \frac{\iint (x, y, f_x', f_y') S(f_x', f_y') df_x' df_y'}{\iint S(f_x', f_y') df_x' df_y'} \quad (2.33)$$

The pupil space can also be related to σ through relationship below:

$$\sigma_x = \frac{f_x \lambda}{NA}, \quad \sigma_y = \frac{f_y \lambda}{NA}$$

Equation (2.33) can be written as:

$$I_{Total}(x, y) = \frac{\iint (x, y, \sigma_x', \sigma_y') S(\sigma_x', \sigma_y') d\sigma_x' d\sigma_y'}{\iint S(\sigma_x', \sigma_y') d\sigma_x' d\sigma_y'} \quad (2.34)$$

An alternative approach for partial coherent imaging is known as Hopkins approach. In Hopkins approach, the order of integration is changed. The source and pupil function are

integrated first to obtain a transmission cross coefficient (TCC) (Hopkins, 1953). It has the property of pupil function and the source shape and image for different masks can be calculated easy by pre-calculating the TCC. Transmission cross coefficient is the product of source function, projection lens pupil function and its conjugate:

$$TCC(f_x) = \int P(f_x + f_x')P^*(f_x''+f_x')S(f_x')df_x' \quad (2.35)$$

The image intensity can be represented by:

$$I_{Total}(x) = \int \int TCC(f_x)M(f_x)M^*(f_x'')e^{i2\pi(f_x-f_x'')}df_xdf_x'' \quad (2.36)$$

Therefore, the image is directly proportional to TCC which is the interaction between the pupil function that is displaced as shown in Eq. (2.36). The higher the overlapping between the displaced pupil function, the higher TCC is and thus the image intensity.

2.3.4 High numerical aperture (NA) vector imaging

It is established that light is an electromagnetic wave that consists of interdependence electric (E) and magnetic (B) field. The electric and magnetic field oscillate at certain characteristic frequency and travel at speed of light. They are at right angle to each other and propagate in the direction that is perpendicular to both fields. Both fields have their phase, magnitude and direction. The direction of electric field, also known as polarization, determines the amount of interference between two light. Light can be conveniently described as the sum of any two basis directions. The most convenient basis directions are transverse electric (TE) and transverse magnetic (TM), their direction are as indicated in Fig. 2.36. For the TE case, the electric field is pointing out of the page whereas for TM case, the electric field is pointing in the page (Mack, 2008).



Fig. 2.36 TE and TM polarization of electric field

The vector method of describing a propagating electric field can be written as

$$\vec{E} = A e^{i(\vec{k} \cdot \vec{r} + \omega t)} \quad (2.37)$$

Where A is the amplitude of the electric field, \vec{k} is the propagation vector and \vec{r} is the positional vector.

The amount of interference between two light depends on the relative direction of the electric fields. For TE case, the resultant field is equivalent to the scalar sum of two light. While for TM case, the resultant field decreases if the relative angle between two traveling light becomes larger. As NA of lithography system becomes larger, the polarization effect of light has to be incorporated in the calculation of image formation.

The resultant electric field between two wave \vec{E}_1 and \vec{E}_2 can be written as

$$\vec{E} = \vec{E}_1 + \vec{E}_2 \quad (2.38)$$

The vector effect of electric field has to be considered in the image formation when light exit from the projection lens and interfere to form image at the resist stage.

Chapter 3 Theoretical analysis

This chapter provides the theoretical development work that forms the basis of several studies conducted. Influence of mask defects on lithography process is described using image perturbation model. It allows factors such as defect sizes, proximity to main feature, transmission and phase to be considered. The optimization of OAI is performed based on overlapping ratio between the 1st and 0th order light at the pupil plane. Modified OAI source shapes are proposed to achieve optimum overlapping ratio for different pitch range. Furthermore, the advantages of patterning contact holes with circular apertures on masks are discussed based on the far field diffraction pattern.

3.1 Influence of mask defect on image

Interference between two neighboring partial coherent beams can be described based on the mutual coherence function (Born and Wolf, 1974). Consider two points P1 and P2, the interference at point Q (Fig. 3.1) under partial coherent illumination can be written as

$$I(Q) = I_1(Q) + I_2(Q) + 2\mu(P_1, P_2)\sqrt{I_1(Q)}\sqrt{I_2(Q)} \quad (3.1)$$

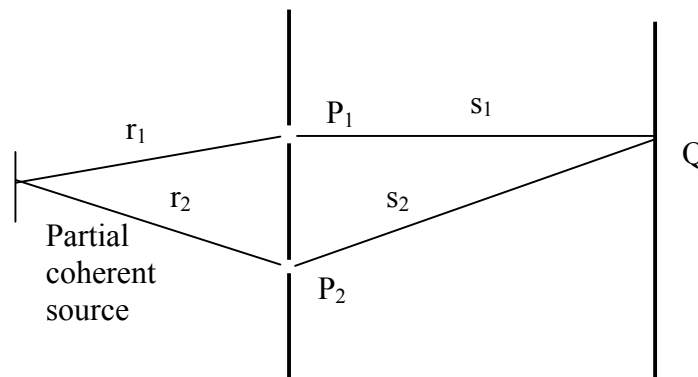


Fig. 3.1 Interference between two neighboring partial coherent beams

$\mu(P_1, P_2)$ is the mutual coherence function, representing the degree of coherence between these two points. The extreme values of $\mu(P_1, P_2)$ are 1 and 0. If $\mu(P_1, P_2)$ has the extreme value of unity, P_1 and P_2 are coherent. If $\mu(P_1, P_2)$ has the extreme value of zero, no interference effect is observed, P_1 and P_2 are incoherent. If $\mu(P_1, P_2)$ has value that is between these extreme values, P_1 and P_2 are partially coherent. From the van Cittert-Zernike theorem (Born and Wolf, 1974), the mutual coherence between P_1 and P_2 is the absolute value of the normalized Fourier transform of the intensity function of the source.

The integral to obtain mutual coherence can be written as

$$\mu(P_1, P_2) = \frac{1}{\sqrt{I(P_1)}\sqrt{I(P_2)}} \int_{\sigma} I(S) \frac{e^{ik(r_1-r_2)}}{r_1 r_2} dS \quad (3.2)$$

In above, $I(S)$ is the intensity function of the source and the integration is carried out over the extent of source. $I(P_1)$ and $I(P_2)$ can be obtained as

$$I(P_1) = \int_{\sigma} \frac{I(S)}{r_1^2} dS, \text{ and } I(P_2) = \int_{\sigma} \frac{I(S)}{r_2^2} dS$$

Essentially, Eq. (3.2) represents the Fourier transform of the source intensity function.

The situation of a main feature and a neighboring defect (Fig. 3.2) shows much resemblance of the case discussed above. Therefore, the interaction between a main feature and a neighboring defect can be described based on the concept of mutual coherence above (Neureuther et. al., 1987; Mastromarco et. al., 1988; Huynh et. al., 1988). This allows a qualitative assessment on the behavior of defect on imaging and identification of critical defect parameters which results in defect printability. Denoting

the image of a main feature as I_f and the image generated by a defect as I_d , the composite image I_c can be approximated by

$$I_c = I_f + I_d \pm 2\mu_{eff}\sqrt{I_f}\sqrt{I_d} \quad (3.3)$$

where μ_{eff} is the effective mutual coherence between the main feature and a neighboring defect. It characterizes the interaction between the main feature and a neighboring defect. If $\mu_{eff} = 1$, the defect has maximum interaction with the main feature and the composite image will be affected significantly. If $\mu_{eff} = 0$, there is no coherence between the defect and the main feature. If I_f is assumed to be much larger than I_d , which is normally the case since a defect is usually smaller than the main feature, the composite image depends only on I_f . However for partial coherent imaging in projection lithography, μ_{eff} is between 0 and 1 and a composite image is formed as a result of interaction between a defect and the main feature (Wong, 2001). Assuming a dark field mask, a positive value of $2\mu_{eff}\sqrt{I_f}\sqrt{I_d}$ is used for a transparent defect, and a negative value of $2\mu_{eff}\sqrt{I_f}\sqrt{I_d}$ for an opaque defect.

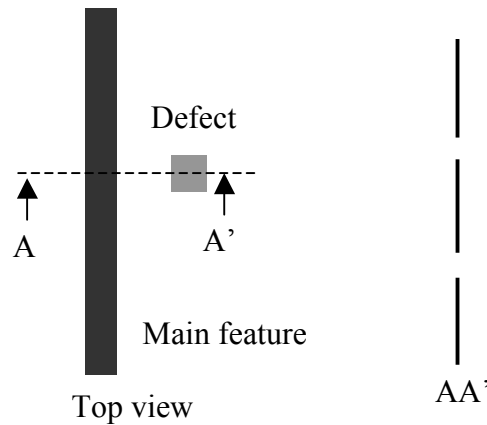


Fig. 3.2 Illustration of main feature and a neighboring defect on a mask

In Eq. (3.3), the image intensity of defect I_d can be approximated by the defect peak intensity,

$$I_d = T_d k A^2 = T_d k l^4 \quad (3.4)$$

where A is the area of a square defect, l is the length, k is a constant for an intensity of unity (Socha et. al., 1995) and T_d is the transmission. The intensity above is obtained by considering a square defect. The peak intensity is dependent on the total incident power on the defect, transmission and area of the defect.

The effective mutual coherence μ_{eff} in Eq. (3.3) can be expressed as (Born, 1972)

$$\mu_{eff} = 2 \frac{J_1(u)}{u} \quad (3.5)$$

where

$$u = \frac{2\pi d \sigma}{\lambda / \text{NA}} \quad (3.6)$$

and σ is the partial coherent factor of the illumination, d is the distance between the main feature and the defect, λ is the wavelength and NA is the numerical aperture.

Eq. (3.5) is derived based on a conventional partial coherent light source shape, expressions for other OAI source shapes can also be obtained readily. For example, the mutual coherence for an annular shape is equivalent to the difference between two conventional partial coherent source (Fig. 3.3).

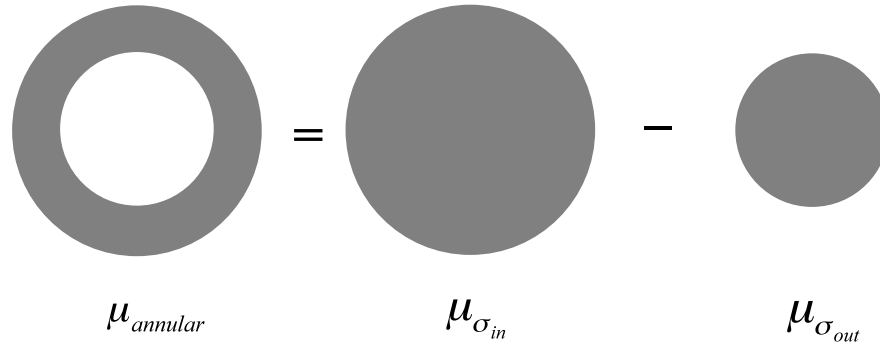


Fig. 3.3 Mutual coherence of an annular source

From Eq. (3.5) and (3.6), it can be seen that the degree of interaction between a defect and the main feature is dependent on the distance between them.

In Eq. (3.3), since $I_d = (E_d)^2$, $\sqrt{I_d}$ is equivalent to the electric field E_d of the defect. The effect of phase change for a defect is not included in Eq. (3.3). In order to consider the phase change, the electric field resulted from main feature and defect shall be considered. If a neighboring defect also results in a phase change of the electric field, its influence on the total electric field E_c is given as follows (Lam and Neureuther, 2003):

$$E_c = E_f - E_{op} + E_d \quad (3.7)$$

$$E_c = E_f - E_{op} + \sqrt{T_d k l^4} \cos \phi_d = E_f - l^2 (1 - \sqrt{T_d k} \cos \phi_d) \quad (3.8)$$

where E_{op} is the electric field due to an opaque defect, E_d is the electric field of the actual defect, and ϕ_d is the phase change caused by the defect. In above, the total electric field E_c is obtained by taking the electric field of the main feature, subtracting it with electric field of an opaque defect of the same size and adding back the electric field

resulted from the actual defect. The process ensures that the effect of phase change resulted by the defect considered is captured.

The composite image intensity is equivalent to

$$I_c = (E_c)^2$$

Thus, Eq. (3.1) can be re-written as

$$I_c = I_f + l^4(1 - \sqrt{T_d k} \cos \phi_d)^2 \pm 2\mu_{eff} E_f l^2(1 - \sqrt{T_d k} \cos \phi_d) \quad (3.9)$$

The model described above is helpful in understanding the interaction between the main feature and the defect. It provides a qualitative description of the defect behavior and allows comparison between contributions from different defect parameters.

In order to obtain a qualitative understanding of different defect parameters on the final CD variation, threshold imaging condition is assumed. In threshold imaging situation where image pattern is formed when image intensity is higher than certain level, the relationship between CD and image intensity can be described as

$$CD \propto \frac{I}{\left. \frac{dI}{dx} \right|_{I_{th}}}$$

The effect of image intensity on the CD can be obtained from the following expression,

$$\Delta CD \propto \frac{\Delta I}{\left. \frac{dI}{dx} \right|_{I_{th}}} = \frac{l^4(1 - \sqrt{T_d k} \cos \phi_d)^2 \pm 2\mu_{eff} E_f l^2(1 - \sqrt{T_d k} \cos \phi_d)}{\left. \frac{dI}{dx} \right|_{I_{th}}} \quad (3.10)$$

Since the defect is small compared to main feature, the square of the electric field would be negligible and the square term $l^4(1 - \sqrt{T_d k} \cos \phi_d)^2$ in Eq. (3.9) can be ignored. Hence, the change in the CD can be re-written as

$$\Delta CD \propto \frac{\Delta I}{\left. \frac{dI}{dx} \right|_{I_{th}}} = \frac{\pm 2\mu_{eff} E_f l^2 (1 - \sqrt{T_d k} \cos \phi_d)}{\left. \frac{dI}{dx} \right|_{I_{th}}} \quad (3.11)$$

From Eq. (3.10), the CD variation can be expressed as follows:

$$\Delta CD \propto \frac{l^2 (1 - \sqrt{T_d k} \cos \phi_d)}{p d\sigma} \quad (3.12)$$

where p represents the pitch of the feature. Since the mask error enhancement factor (MEEF) is generally larger for a smaller pitch (Mack, 2007), the CD variation due to presence of defect is inversely related to the pitch.

3.2 Resolution enhancement

The partial coherence setting of OAI has a direct implication on DOF of a lithography process. In the following discussion, the relationship between partial coherence setting, pattern density, and DOF is studied. A useful figure of merit for comparing the effectiveness of different partial coherence settings is developed.

In lithography, the illumination source applied is partially coherent and light incidents at an angle on the mask (Fig. 3.4). This results in the shift of the position (spatial frequencies shift) of the diffraction pattern in the diffraction plane. As shown in Fig. 3.4, the shift in spatial frequencies is given by

$$f_x' = \frac{\sin \theta_i}{\lambda} \quad (3.13)$$

In above, θ_i is the incident angle on the mask, from Eq. (2.30),

$$\sin \theta_i = \sigma_i \text{NA} \quad (3.14)$$

where σ_i is the partial coherence factor corresponds to the incident angle.

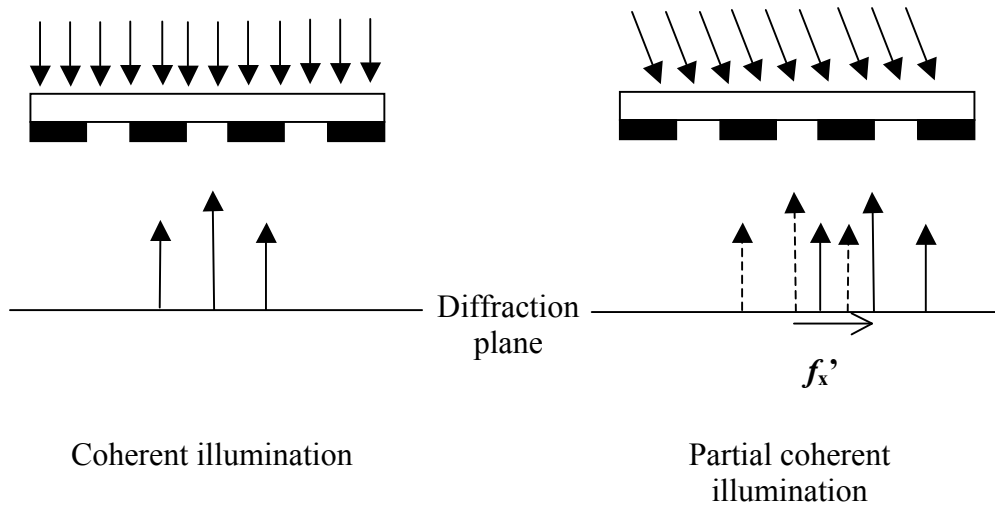


Fig. 3.4 Spatial frequencies shift due to partial coherent illumination

Fig. 3.5 illustrates the distribution of the diffraction orders after the mask as a result of partially coherent light incidents at an angle θ_i on the mask. The angular separation of diffraction order remains unaffected but it is tilted by an angle which is equivalent to θ_i .

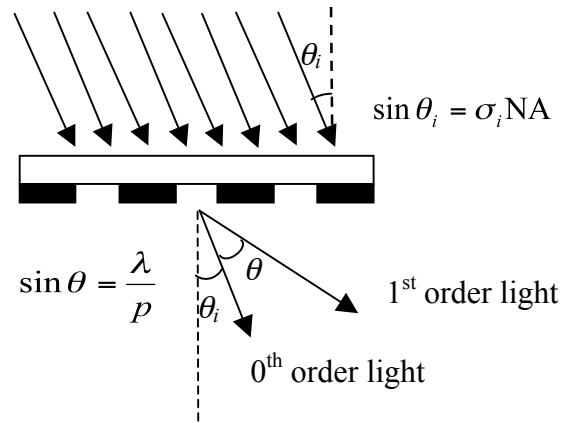


Fig. 3.5 Diffraction orders distribution of a mask subjected to partially coherent light

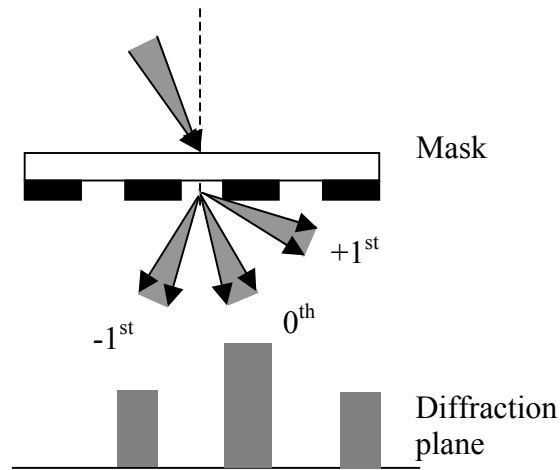


Fig. 3.6 Diffraction orders distribution for OAI

As seen from Fig. 3.4 and 3.5, tilting the illumination incident angle on mask causes a shift in diffraction pattern. Since OAI consist of a range of incident angle, a range of shift in diffraction order is expected and this result in the broadening of diffraction pattern, as seen in Fig. 3.6. Typical diffraction pattern at the projection lens pupil plane for an annular OAI is shown in Fig. 3.7. It is seen that the diffraction pattern appears as annular rings with 0th order light at the center of the lens pupil, and 1st order light at the edge of the lens pupil. This is because the optical settings used for lithography system is known

as Köhler illumination (Fig. 3.8), in which the condenser lens is used to form an image of the source at the projection lens pupil and the mask is placed at the exit pupil of the condenser lens. This ensures that the mask is illuminated with converging spherical waves so that the image of identical pattern at different field on a mask can be converged to the same point at the projection lens pupil. Besides, the illumination intensity on the mask is uniform since each source point illuminates the mask.

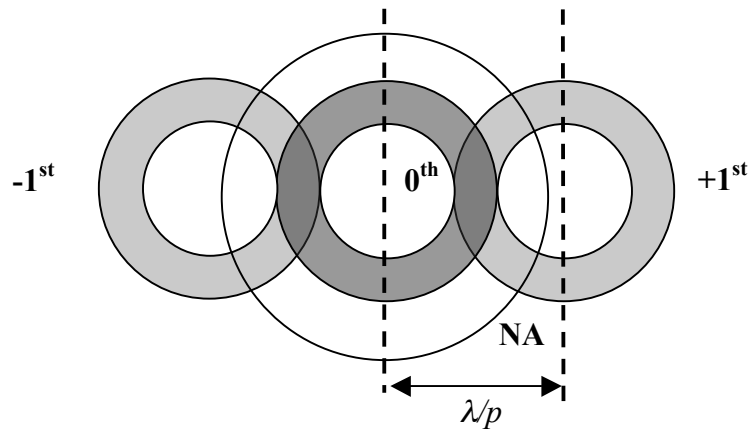


Fig. 3.7 Typical diffraction pattern observed at projection pupil plane for annular OAI

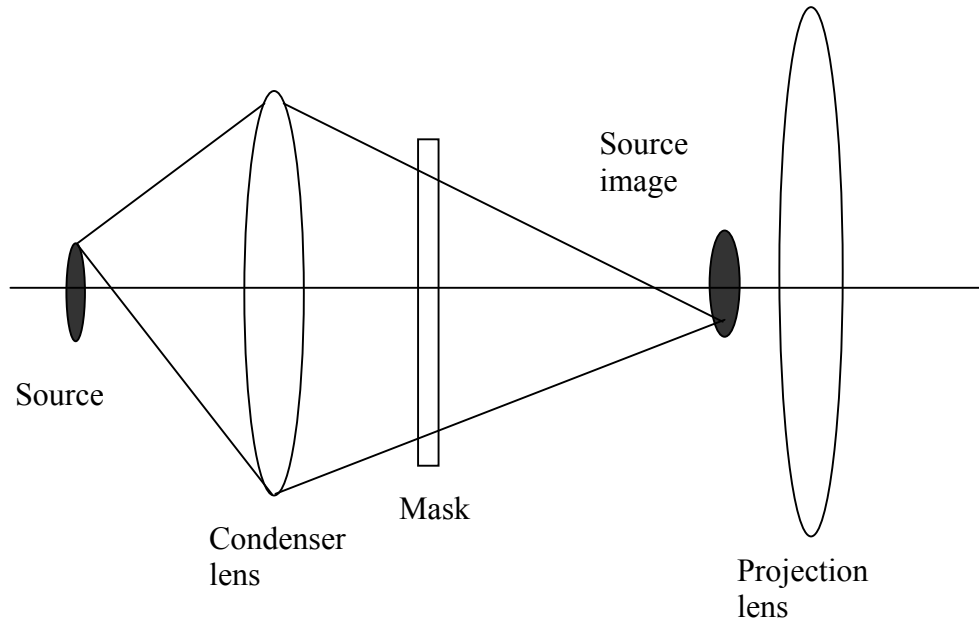


Fig. 3.8 Schematic diagram of Köhler illumination

Thus, the application of partial coherent OAI helps lowering the resolution limit of lithography system by enabling the partial capture of 1st order light which would not be possible in the case of conventional on axis illumination. Nevertheless, certain partial coherent setting is only beneficial for particular pitch and will degrade the image contrast for other pitches. Therefore, the optimization of partial coherent setting for OAI is essential to achieve resolution enhancement for smaller features while maintaining reasonable process windows for larger features. In the following discussion, the relationship between partial coherent settings for OAI and image formation is analyzed. Based on the understanding, a useful metric is developed for OAI optimization. Furthermore, a new concept for OAI source shape is proposed to improve through pitch imaging performance.

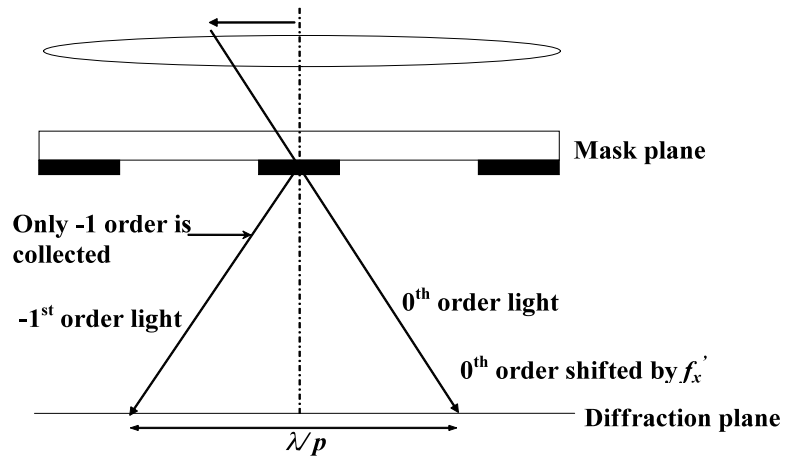


Fig. 3.9 Diffraction order of binary mask illuminated by an off-axis source point

The optimization of partial coherent settings for OAI is discussed based on the imaging of a periodic line and space pattern on binary intensity mask. Diffraction orders of a binary mask illuminated by an off-axis source point located at a distance x from the origin is shown in Fig. 3.9. For a small pitch only the 0^{th} and -1^{st} order diffracted light fall on the projection lens pupil plane.

The spatial frequencies f_x and f_y relative to the mask plane (x,y) are defined in Fig. 3.10 and are given by

$$f_x = \frac{\sin \theta_x}{\lambda} = \frac{x}{\lambda z}, \quad f_y = \frac{\sin \theta_y}{\lambda} = \frac{y}{\lambda z}$$

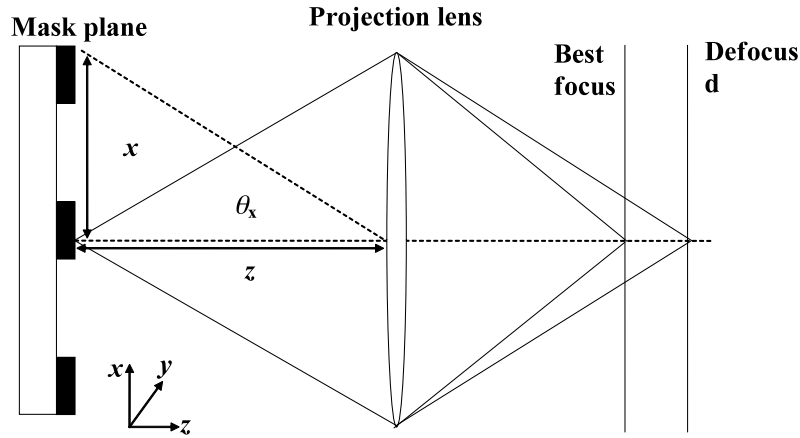


Fig. 3.10 Definition of spatial frequencies f_x and f_y

The electric field at image plane (x', y') is the inverse Fourier transform of the mask diffraction spectrum multiplied by the pupil function $P(f_x, f_y)$.

$$E(x') = F^{-1} \{ M(f_x) P(f_x, f_y) \} \quad (3.15)$$

The pupil function $P(f_x, f_y)$ is defined below

$$P(f_x, f_y) = \begin{cases} 1 & \text{if } \sqrt{f_x^2 + f_y^2} < \frac{\text{NA}}{\lambda} \\ 0 & \text{if } \sqrt{f_x^2 + f_y^2} > \frac{\text{NA}}{\lambda} \end{cases} \quad (3.16)$$

The electric field at the image plane can be obtained as

$$E(x') = \frac{d}{p} \sum_{n=-\infty}^{\infty} \text{sinc}\left(\frac{\pi n d}{p}\right) e^{i \frac{2\pi n x}{p}} \quad (3.17)$$

The electric field at image plane is the sum of plane waves reaching it. On axis source point is assumed in above derivation. For an off axis source point, the diffraction pattern is shifted by f_x' and for dense pitch, it can be assumed that only 0 and +1 or -1 diffraction order is collected at the pupil plane. For a source point located at $-x$ direction relative to

the origin, the diffraction pattern is shifted in $+f_x$ direction by f_x' and -1 diffraction order is collected, as shown in Fig. 3.9,

$$M(f_x) = \frac{d}{p} \sum_{n=-\infty}^{\infty} \sin c[\pi d(f_x - f_x')] \delta(f_x - f_x' - \frac{n}{p}) \quad (3.18)$$

For the case denoted in Fig. 3.9,

$$M(f_x) = a_0 \delta(f_x - f_x') + a_1 \delta(f_x - f_x' + \frac{1}{p}) \quad (3.19)$$

a_0 and a_1 are the amplitudes of zero and first order respectively and they can be found through Eq. (3.18), depending on the pitch and width of the feature.

Electric field of the image due to the off axis point can be expressed as

$$E(x') = a_0 e^{i2\pi f_x' x'} + a_1 e^{i2\pi(f_x' - \frac{1}{p})x'} \quad (3.20)$$

The above expression for electric field in Eq. (3.20) is the image at the best focus plane.

The effect of defocus can be considered by adding a phase change to the phase term for the zero and first order plane waves that reach the wafer plane.

$$E(x') = a_0 e^{i2\pi f_x' x'} e^{i\Delta\phi_0} + a_1 e^{i2\pi(f_x' - \frac{1}{p})x'} e^{i\Delta\phi_1} \quad (3.21)$$

$$E(x') = e^{i2\pi f_x' x'} e^{i\Delta\phi_0} [a_0 + a_1 e^{i(\Delta\phi_1 - \Delta\phi_0)} e^{-i2\pi \frac{x'}{p}}]$$

The phase change resulted by defocus, d is denoted by $\Delta\phi_0$ and $\Delta\phi_1$. They are as follow:

$$\Delta\phi_0 = \frac{2\pi}{\lambda} d[1 - \sqrt{1 - (\lambda f_x')^2}] \quad \Delta\phi_1 = \frac{2\pi}{\lambda} d[1 - \sqrt{1 - \lambda^2(\frac{1}{p} - f_x')^2}]$$

The image intensity is the square of the electric field. It is directly proportional of the square of the bracket terms.

$$I(x') = |E(x')|^2 = \left| e^{i2\pi f_x' x'} e^{i\Delta\phi_0} [a_0 + a_1 e^{i(\Delta\phi_1 - \Delta\phi_0)} e^{-i2\pi \frac{x'}{p}}] \right|^2 \quad (3.22)$$

$$I(x') = \left| e^{i2\pi f_x' x'} e^{i\Delta\phi_0} \right|^2 [a_0^2 + 2a_1 a_0 \cos(2\pi \frac{x'}{p} - \Delta\phi_1 + \Delta\phi_0) + a_1^2]$$

For a symmetric OAI, there will be two source points located at $+f_x'$ and $-f_x'$. The resultant image $I_r(x')$ is formed by an average of images from each source point at the defocus plane d is given by

$$I_r(x') = \frac{I(x', f_x') + I(x', -f_x')}{2}$$

$$I_r(x') = \left| e^{i2\pi f_x' x'} e^{i\Delta\phi_0} \right|^2 [a_0^2 + 2a_1 a_0 \cos(2\pi \frac{x'}{p}) \cos(\Delta\phi_1 - \Delta\phi_0) + a_1^2] \quad (3.23)$$

$$\text{where } \Delta\phi_0 = \frac{2\pi}{\lambda} d [1 - \sqrt{1 - (\lambda f_x')^2}] \quad , \quad \Delta\phi_1 = \frac{2\pi}{\lambda} d [1 - \sqrt{1 - \lambda^2 (\frac{1}{p} - f_x')^2}]$$

p is feature pitch and a_0 and a_1 are the amplitudes of 0th and 1st order diffraction respectively. (Mack, 2008)

Image contrast can be found by

$$C = \frac{I_{\max} - I_{\min}}{I_{\max} + I_{\min}} = \frac{2a_0 a_1 \cos(\Delta\phi_1 - \Delta\phi_0)}{a_0^2 + a_1^2} \quad (3.24)$$

From Eq. (3.24) it is seen that the image contrast is related to $\cos(\Delta\phi_1 - \Delta\phi_0)$, larger phase difference between 0th and 1st order will degrade the image contrast and reduce DOF. Maximum contrast can be achieved if $\Delta\phi_1 = \Delta\phi_0$, and the image contrast dependent only on the magnitude of a_0 and a_1 . This can be achieved if

$$f_x' = \pm \frac{1}{2p} \quad (3.25)$$

In terms of partial coherent setting, the location of source point in terms of σ_x can be obtained by applying

$$\sigma_x = \frac{f_x' \lambda}{NA} \quad (3.26)$$

σ is the partial coherence of illumination defined by

$$\sigma_x = \frac{NA_{\text{condenser lens}}}{NA_{\text{pupil lens}}}$$

However in a partial coherent OAI, there are other source points which are located at different positions. Hence, the DOF is limited for a particular illumination setting and pitch. It would be useful to relate the phase difference between the 0th and 1st order diffraction with the illumination setting. Assuming small incidence angle, the term $(\Delta\phi_1 - \Delta\phi_0)$ can be simplified using Taylor series expansion:

$$\Delta\phi_1 - \Delta\phi_0 = \pi d \lambda \left[\left(\frac{1}{p} - f_x' \right)^2 - f_x'^2 \right] = \frac{\pi d \lambda}{p} \left(\frac{1}{p} - 2f_x' \right)$$

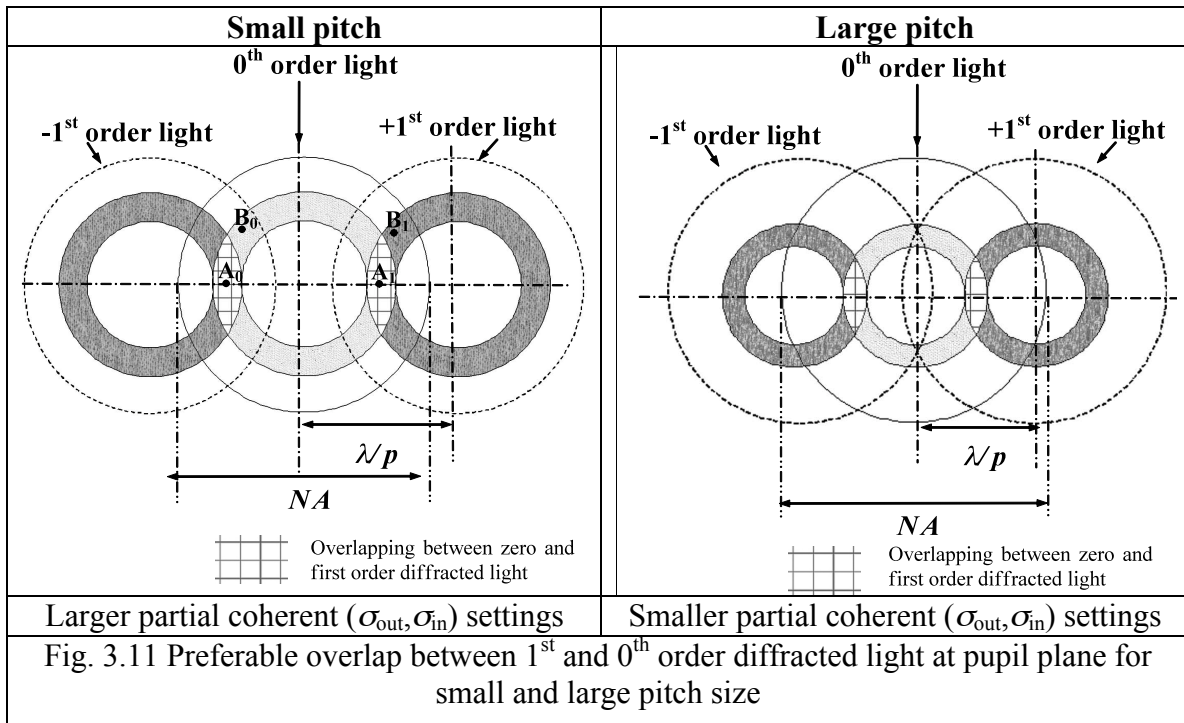
If f_x' is expressed as $f_x' = \frac{1}{2p} - \Delta f_x'$ and since $\Delta f_x' = \frac{\Delta\sigma_x' NA}{\lambda}$

$$\Delta\phi_1 - \Delta\phi_0 = \frac{2\pi d NA}{p} \Delta\sigma_x' \quad (3.27)$$

$\Delta\sigma_x'$ is the partial coherent difference between any two source points of interest. As it increases, the phase difference increases and the image contrast reduces. Since the contrast is directly related to the DOF, an increase in phase difference also results in a reduction in the DOF. If the entire illumination is considered, integration is carried out according to the shape of the source using Eqs. (3.23) to (3.27).

From Eqs. (3.23) and (3.27), it is seen that good image contrast is obtained if the phase difference between 0th and 1st diffraction order is small for all source points for a

particular illumination source. It can be seen from Fig. 3.11 that most OAI are symmetric about the origin. The phase difference between the 0th and 1st order light is minimized when they are distributed symmetrically about the origin of the pupil plane. As shown in Fig. 3.11, points A_0 (0th order) and A_1 (1st order) are symmetrical about the origin of the pupil plane and will provide good image contrast. Points B_0 (0th order) and B_1 (1st order) are not symmetric about the origin and will result in a large phase difference during image formation. It is seen that symmetrical distribution of the 0th and 1st order light will result in a larger overlapping region between the 0th and 1st order light at the pupil plane.



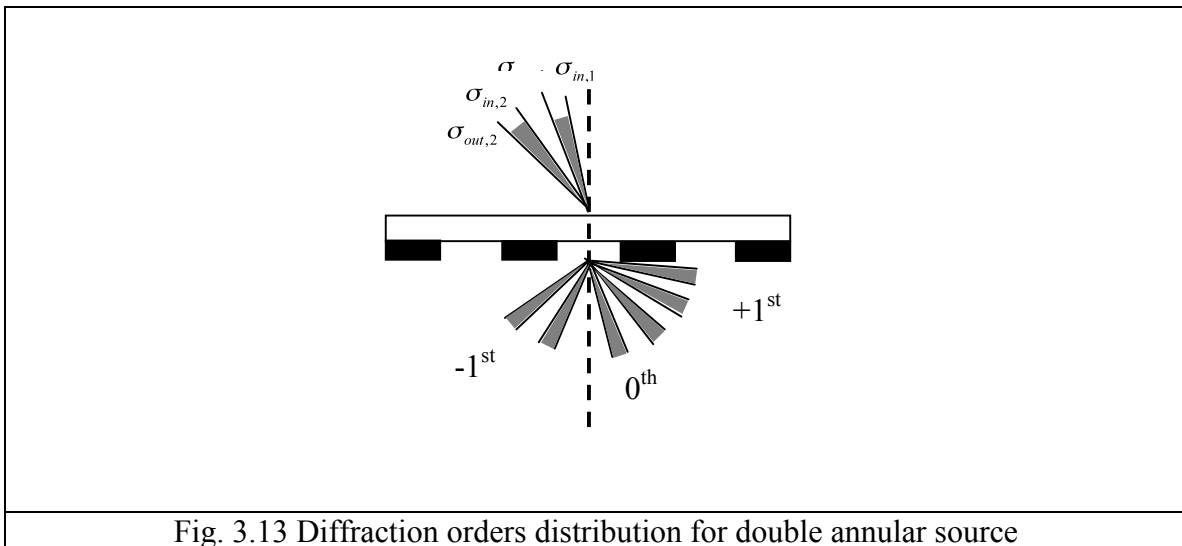
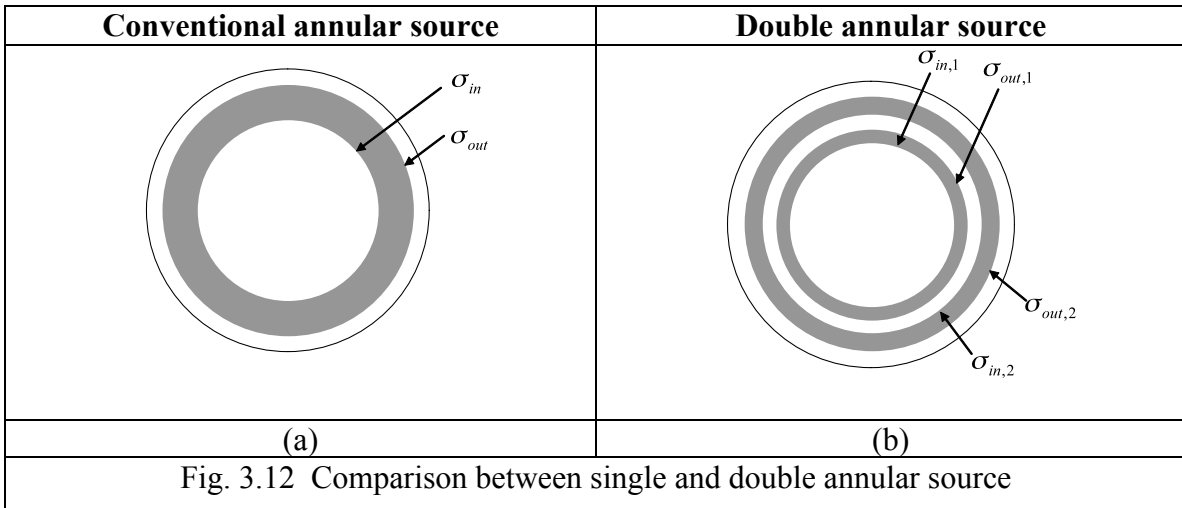
Some studies have proposed the use of an overlap ratio η given by the ratio between the 1st (and higher) order light and 0th order light as a metric for illumination optimization (Chua et. al., 2004; Chua et.al.,2008), given by:

$$DOF \propto \eta = \frac{A_{overlap}}{A_{zero}} \quad (3.28)$$

where A_{overlap} is the area of overlap between 1st (and higher) order and 0th order light at the pupil plane and A_{zero} is the area of 0th order light collected at the pupil plane. For a dense pitch, only the 1st and 0th order is collected and η is thus proportional to the area of overlap between the 1st and 0th order at the pupil plane. At the smallest pitch, the illumination is optimized such that maximum overlap occurs. As the pitch increases, the first order light would move towards the center of the pupil plane. The area of overlap and thus the DOF will reduce with increasing pitch. Therefore, it can be deduced that the overlap factor η is inversely proportional to the pitch. For larger pitch, higher order diffracted light is collected at the pupil plane. Higher order diffracted light would help to restore some of the lost image contrast due to reduced overlap between 1st and 0th order light. Hence, it is also desirable to increase the overlap between higher order with 0th order light for better image contrast and DOF.

From above, it has been established that by increasing the overlap area between 0th order and 1st order light, enhancement in image contrast can be achieved. However, the application of OAI often resulted in forbidden pitch phenomenon because illumination settings are optimized for the smallest pitch. At larger pitch size, the overlapping reduces and results in image contrast degradation. A new OAI configuration is proposed in order to resolve the forbidden pitch image contrast degradation and achieve uniform through pitch imaging performance. Figure 3.12a shows a conventional annular OAI light source and Fig. 3.12b shows one conventional annular OAI superposed on another, thus allows a double annular OAI. The partial coherent illumination size for inner annular is denoted as $\sigma_{\text{out},1}$ and $\sigma_{\text{in},1}$; that for the outer annular is denoted as $\sigma_{\text{out},2}$ and $\sigma_{\text{in},2}$. The choice of each partial coherent value depends on the pitch range to be patterned. The outer annular

can be set to an optimum partial coherent value for the smallest pitch while the inner annular can be used to improve the image contrast and DOF at the forbidden pitch. The diffraction orders distribution after light passes through the mask resulted by double annular OAI is shown in Fig. 3.13. Figure 3.14 shows qualitatively the improvement on overlap ratio at the forbidden pitch. With the proposed illumination, the inner annular provides additional overlapping area at the forbidden pitch and improves image contrast.



Convetional annular source shape	Modified double annular source shape
----------------------------------	--------------------------------------

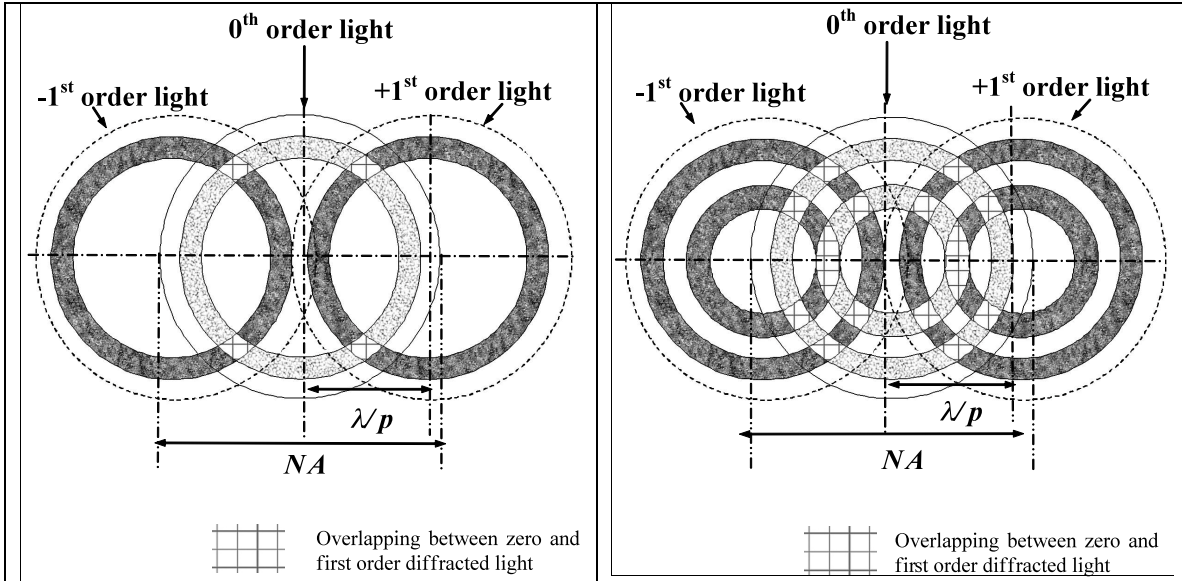


Fig. 3.14 Improvement of overlapping area at pupil plane using a double annular source

The main advantage of the proposed double annular sources over the conventional single annular source is a reduction in the phase difference between the 0th and 1st order light. For a single annular source of large annular thickness ($\sigma_{out} - \sigma_{in}$), the phase difference between the 0th and 1st order light is large, resulting in reduced image contrast and DOF. This problem can be alleviated by the double annular sources which is similar to a large annular source with a gap in between the inner and outer annular. This results in a smaller annular thickness ($\sigma_{out} - \sigma_{in}$) and hence an improvement in contrast and DOF. The double annular sources also allow the inclusion of additional optimum source point at the forbidden pitch region.

3.3 Effect of changing mask openings shape on imaging

The Fraunhofer diffraction field of a square hole with sides a is given by (Hecht, 2002)

$$E(f, g) = C \operatorname{sinc}(kf) \operatorname{sinc}(g) \quad (3.29)$$

In Eq. (3.29), C is the constant depends on the source and point of observation, k is the wave propagation number equivalent to $\frac{2\pi}{\lambda}$, f and g are the spatial frequencies in x and y directions respectively. The *sinc* function above is given by $\operatorname{sinc}(a) = \frac{\sin a}{a}$.

The Fraunhofer diffraction field of a circular hole with radius r is given by

$$E(w) = D \frac{2J_1(krw)}{krw} \quad (3.30)$$

In Eq. (3.30), w is the spatial frequencies in polar coordinates such that $w = \sqrt{f^2 + g^2}$ and J_1 is the Bessel function of the first kind. D is the constant depends on the source and point of observation.

The aerial images formed by square and circular hole are found by inverse Fourier transform of Fraunhofer diffraction fields in Eq. (3.29) and (3.30). The aerial image intensity of square and circular hole are given by

$$I_{\text{square}}(x, y) \propto [\operatorname{sinc}(kx) \operatorname{sinc}(ky)]^2 \quad (3.31)$$

$$I_{\text{circular}}(r) \propto \left[\frac{J_1(kr)}{kr} \right]^2 \quad (3.32)$$

The normalize intensity of square and circular hole are plotted in Fig. 3.15. Both intensity plots show a center and subsequent secondary peaks. However, it is seen that J_1 that represents circular hole intensity has a broader center peak and lower secondary peaks compared with *sinc* of a square hole. The fraction of total input energy that is bound within the second minima for J_1 is 91% but that for a *sinc* function is 10% less. This is because a circular hole has more gradual transition of shape at the corners than a square

hole. The spatial frequency at the corner is thus lower for a circular hole and thus more energy can be collected at lower diffraction order.

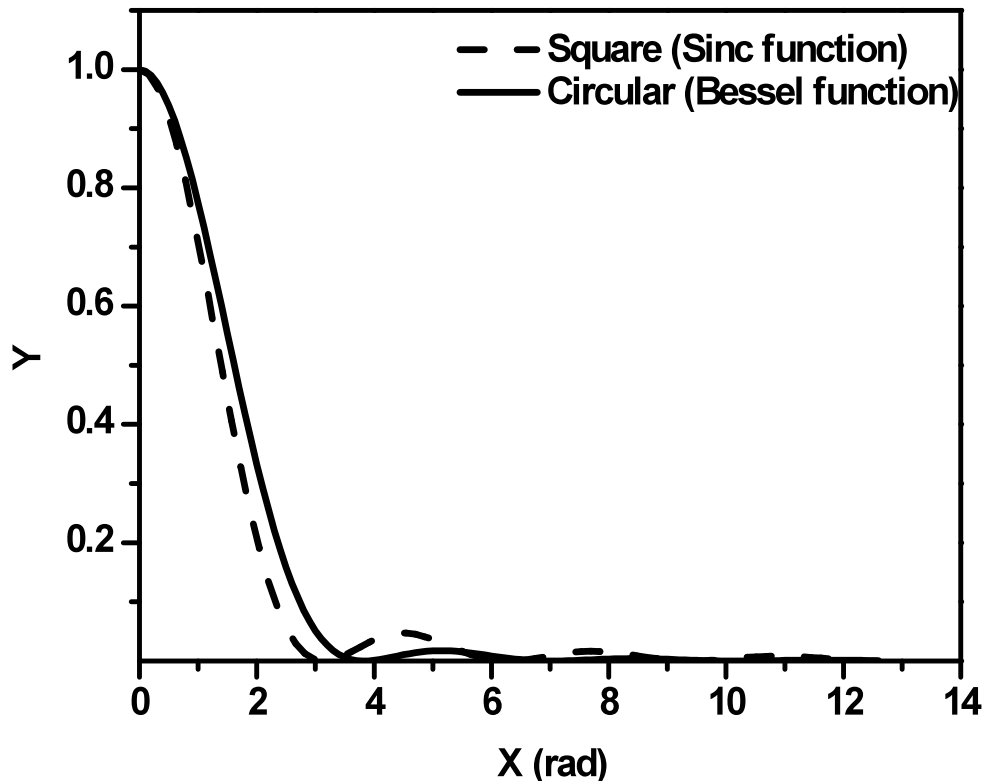


Fig. 3.15 Normalized intensity plot for circular and square aperture along positive x – axis

In lithography, the light diffracted from mask is not entirely collected at the pupil plane due to limitation of numerical aperture (NA) of the lens. Higher order light at larger spatial frequency is filtered and optical information is loss in this low-pass frequency filtering process. Conventional optical proximity correction (OPC) approach involves targeting a square contact hole but printed pattern is circular due to corner rounding as a result of this frequency filtering process. As the dimension of contact holes reduces, more light is diffracted towards higher spatial frequency and thus compromised image contrast. The process windows enhancement resulted from conventional OPC approach is limited and side lobes printing is encountered more frequently.

From Eq. (2.22) and (2.23), it is seen that the far field diffraction pattern of a mask with repeating features with regular period is a convolution of a function describing the shape of an isolated feature and a comb function describing the pitch. Thus, the mask function that represents circular contact holes array is convolution of a *circ* function and *comb* function in x and y directions, given by (Goodman, 1996)

$$m(x,y) = \text{circ}\left(\frac{q}{r}\right) \otimes \sum_{n=-\infty}^{\infty} \sum_{m=-\infty}^{\infty} \delta(x - np)\delta(y - mp) \quad (3.33)$$

In Eq. (3.33), $\text{circ}\left(\frac{q}{r}\right)$ is a function that characterizes a circular aperture with radius r and q is the position in radial direction, $q = \sqrt{x^2 + y^2}$. $\text{comb}(x - np)\text{comb}(y - mp)$ is a collection of delta directions function in the x and y directions, with a distance of p which is the pitch of the array. n and m are positive integers.

The Fraunhofer diffraction field of circular hole array is the Fourier transform of Eq. (3.33), given by

$$M(f, g) = \sum_{j,k=0}^{\infty} \left(\frac{r}{p}\right)^2 \frac{2\pi J_1(krw)}{krw} \delta\left(f - \frac{j}{p}\right) \delta\left(g - \frac{k}{p}\right) \quad (3.34)$$

In Eq. (3.34), $\delta\left(f - \frac{j}{p}\right)\delta\left(g - \frac{k}{p}\right)$ is the delta function which represents the locations of diffraction orders.

Similarly, the mask function that represents the regular square hole array is given by

$$m(x, y) = \text{rect}\left(\frac{d}{a}\right) \otimes \text{comb}(x - np) \text{comb}(y - mp)$$

where a is the side length of the hole, and $d = \sqrt{x^2 + y^2}$

Thus, the diffraction pattern for square contact holes array is similar to Eq. (3.34), given by

$$M(f, g) = \sum_{j,k=0}^{\infty} \left(\frac{a}{p}\right)^2 \text{sinc}(kf) \text{sinc}(kg) \delta\left(f - \frac{j}{p}\right) \delta\left(g - \frac{k}{p}\right) \quad (3.35)$$

Therefore, the diffraction order distribution is discrete and the magnitude is defined by envelope of Bessel or sinc function depending on the type of aperture.

Bessel function and sinc function in positive spatial frequencies are plotted in Fig. 3.16. It can be observed that the Bessel function has more gradual drop from the center peak than the sinc function. From above, the diffraction order of contact holes array is characterized by respective envelope functions. For circular holes array, the drop is more gradual with a Bessel function envelope and this contributes to higher magnitude of diffraction orders collected compared with that collected from conventional square holes array with a sinc function.

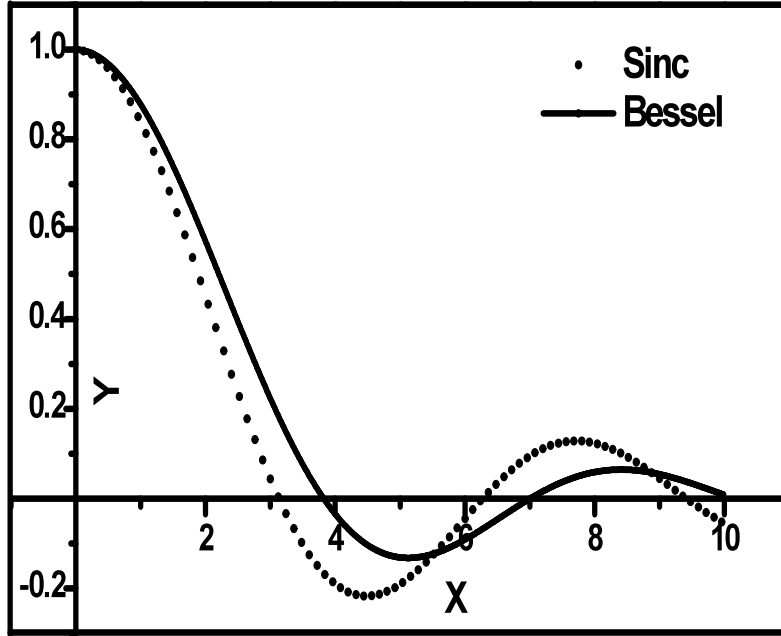


Fig. 3.16 Comparison between Bessel and sinc function envelope

Consider the final image in the x direction and assuming only 0th and 1st order diffracted light is captured at the projection pupil plane, the aerial image intensity after inverse Fourier transform is in the form (Mack, 2007)

$$I(x) = a_0^2 + a_1^2 + 2a_0a_1 \cos\left(\frac{2\pi x}{p}\right) \quad (3.36)$$

In Eq. (3.36), it is seen that the aerial image intensity is directly related to a_0 and a_1 , which are the amplitude of 0th and 1st order light respectively. The image contrast is given by

$$Contrast = \frac{I_{\max} - I_{\min}}{I_{\max} + I_{\min}} \propto \frac{2a_0a_1}{a_0^2 + a_1^2} \quad (3.37)$$

From Eq. (3.37), it is seen that the image contrast is directly related to the product of a_0 and a_1 .

For a circular hole with diameter equal to half of the pitch, the value of a_0 and a_1 can be calculated from Eq. (3.34), substituting $r = \frac{p}{4}$, $\lambda = 193$ nm,

$$a_0 = 0.39$$

$$a_1 = 0.18$$

For square contact hole with side lengths equal to half of the pitch, the corresponding a_0 and a_1 are obtained from Eq. (3.35), substituting $a = \frac{p}{2}$, $\lambda = 193$ nm,

$$a_0 = 0.25$$

$$a_1 = 0.1$$

From the calculation above, it has been shown that circular holes array results in higher a_0 and a_1 . Therefore, the image contrast is expected to be enhanced by the implementation of circular hole.

In order to correct imaging error for non array contact holes pattern, radial segmentation approach with application of circular aperture is proposed. In this new segmentation approach, the parameters (Fig. 3.17) to be considered when determining the dimensions of an aperture on mask are as follows:

r : the radius of the circular openings on mask,

Δr : the radial extension of the segment applied on the circumference of a circular opening

θ_r : opening angle of the segment applied on the circumference of a circular opening

The radius of the opening is dependent on the target CD that is desired.

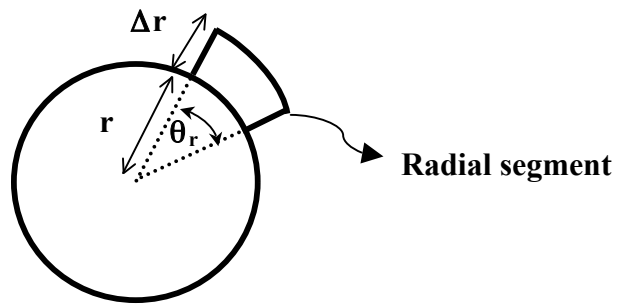


Fig. 3.17 Illustration of radial segmentation approach

Chapter 4 Experimental and simulation work

The details of simulation and experiment work are presented in this chapter. The equipment for experimental CD measurement and procedures in determining the process window is introduced. Furthermore, the details of experimental and simulation conditions is provided in the later part of this chapter.

4.1 Linewidth and process windows measurement

4.1.1 Linewidth measurement

Experimental measurement of CD is accomplished using a Scanning Electron Microscope (SEM). A schematic diagram of SEM is shown in Fig. 4.1. CD-SEM is an essential tool in wafer fab that is used for wafer fabrication process monitoring. It has the advantage of providing high throughput measurements and can be fully automated.

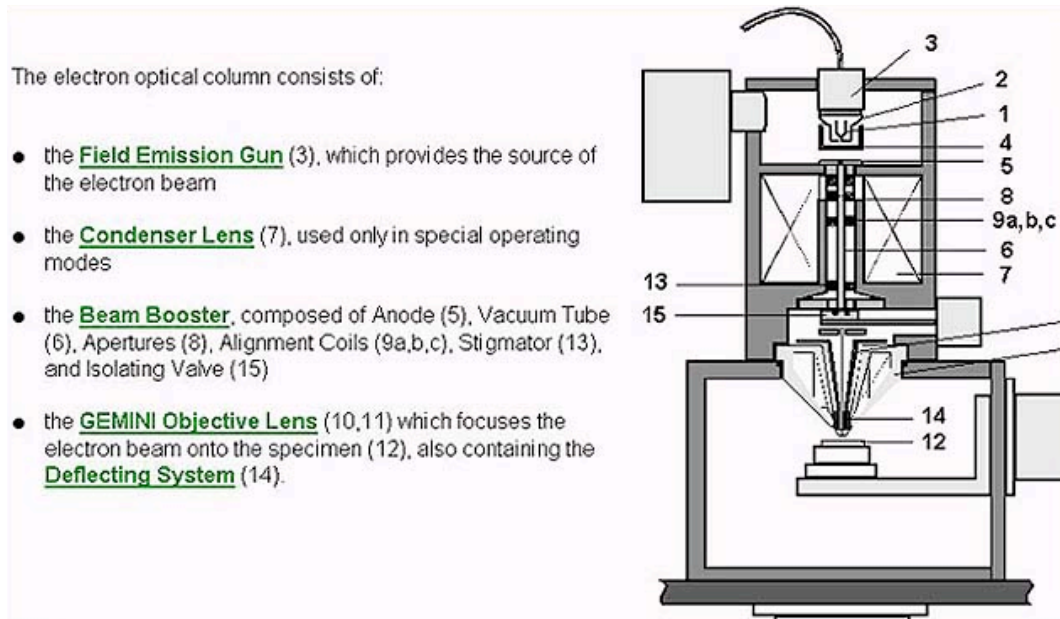


Fig. 4.1 Schematic diagram of a SEM (<http://www.hkbu.edu.hk/~csar/semidiagram.jpg>)

4.1.2 Focus exposure matrix

During the wafer fabrication process, the final resist profile on wafer varies with dose and focus settings. Focus exposure matrix (FEM) is the performance indicator for the robustness of a lithography process. A FEM wafer can be obtained by exposing different dies on the wafer with different dose and focus condition. Fig. 4.2 shows a typical FEM wafer split: the exposure dose is varied along horizontal direction, and focus is varied along vertical direction

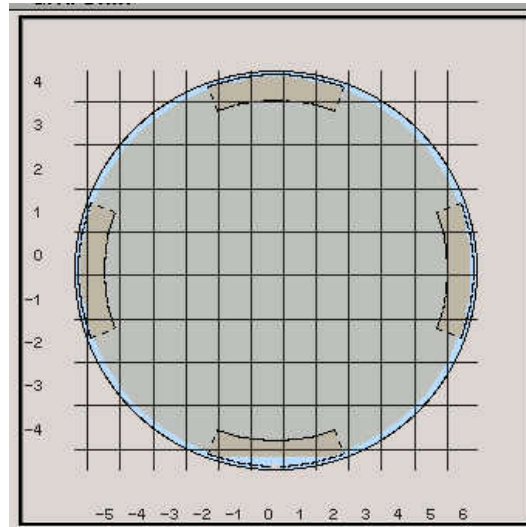


Fig. 4.2 Wafer split for FEM experiment

From the FEM experiment, bossung plot which shows the changes of CD with respect to different focus and dose conditions. An example of bossung plot is shown in Fig. 4.3.

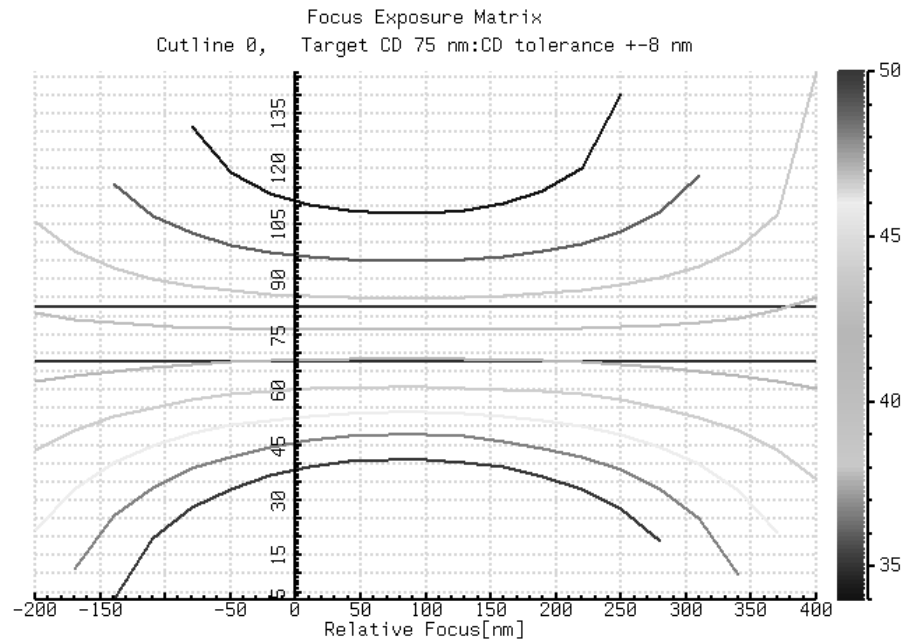


Fig. 4.3 Illustration of a typical Bossung plot

The process window can then be obtained by plotting the linewidth against dose and focus, as shown in Fig. 4.4a. Process window is the allowable variation in exposure dose and focus conditions for a lithography process. Fig. 4.4b shows the plot of exposure latitude against depth of focus plot which illustrates the changes in depth of focus (DOF) with respect to exposure dose fluctuation. The DOF discussed in this thesis is specified at 5 % exposure latitude.

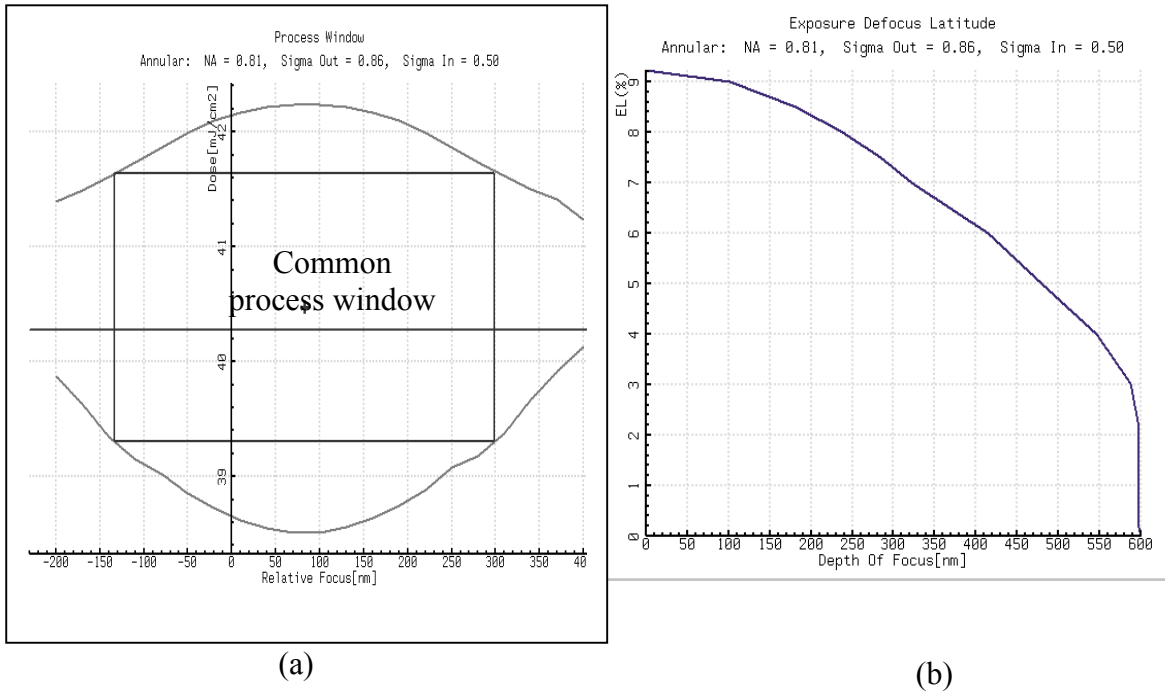


Fig. 4.4 Illustration of (a) Common process window ; (b) Exposure latitude against depth of focus

4.1.3 Lithography exposure tool

The experimental exposure in this study is conducted on the ASML 1400i, a commercially available immersion lithography system. The schematic diagram of this lithography system is shown in Fig. 4.5. The highest NA achievable using this tool is 1.2 and the average throughput per hour is around 150 wafers per hour.

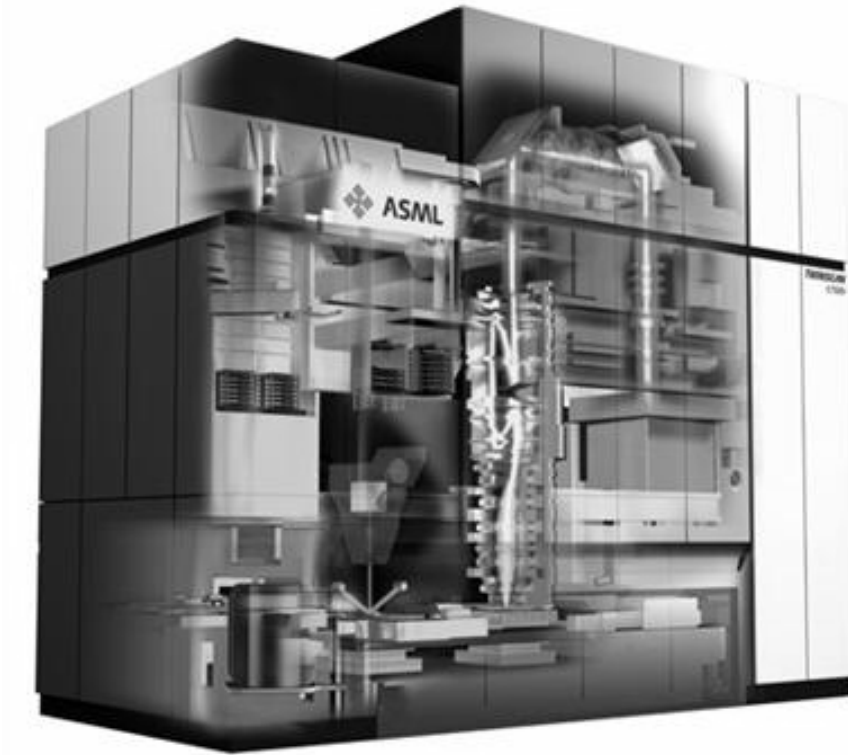


Fig.4.5 Lithography exposure tool (ASML)

4.2 Mask design

A 6% attenuated phase shifting mask (AttPSM) with programmed defects is used for the experimental study. Square defects which vary from 10 nm to 50 nm in size were placed at specific locations on the mask. They were inserted adjacent to a main feature as well as in the mid point between two neighboring features at an active and polysilicon layer of a standard 45nm static random access memory (SRAM) cell. The defects are of the same transmission and phase shift as the main feature. The experimental conditions are shown in Table 4.1. The comparison between two masking layers allows observation of the interaction defect printability with pattern density. Furthermore, exposures are done using Quasar off-axis illumination, with NA of 1.10 and $(\sigma_{in}, \sigma_{out})$ of (0.65 , 0.86). The

locations of defects relative to the main features are shown in Fig. 4.6. Measurement of the CD is carried out using a CD-SEM.

Table 4.1 Experimental conditions for programmed defect mask exposure

Location of defect	Active layer defect		Polysilicon layer defect	
	Mid-point defect (Location A)	Adjacent defect (Location B)	Mid-point defect (Location C)	Adjacent defect (Location D)
Defect sizes (1X)	10 – 50nm	10 – 50nm	10 – 50nm	10 – 50nm
OAI	Quasar	Quasar	Quasar	Quasar
NA	1.1	1.1	1.1	1.1
$\sigma_{in}, \sigma_{out}$	0.65 , 0.86	0.65 , 0.86	0.65 , 0.86	0.65 , 0.86

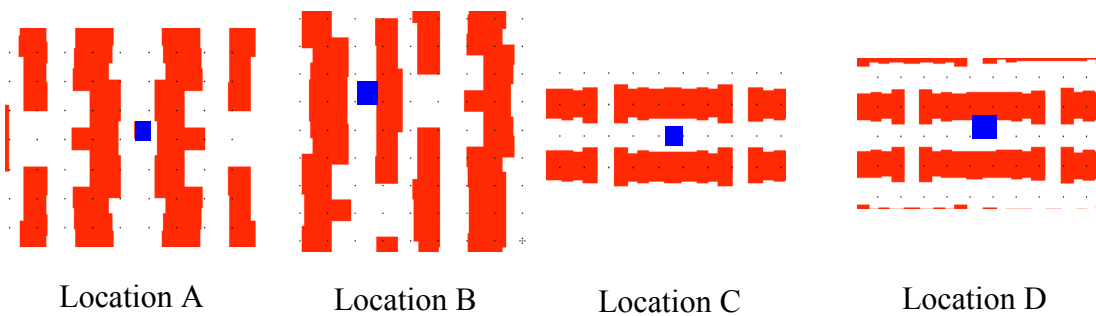


Fig. 4.6 Location of programmed defect relative to main features

4.3 Simulation work

The simulation work in this study is carried out using a lithography simulation tool known as LithoCruiser™, developed by ASML. LithoCruiser™ contains database and model of actual lithography steppers, which allows a user to develop process setups that are feasible with existing steppers. Meanwhile, it also provides the flexibility to develop and study novel process components such as illumination source shapes and non conventional mask feature shapes through customized data entries. It is a versatile tool that can be used to conduct research study, process development and manufacturing

optimization. LithoCruiser™ simulation provides detailed information about lithography process under study such as the process window, aerial image intensity, CD uniformity distribution and diffraction order distribution at pupil plane.

The model for LithoCruiser™ is based on vector imaging theory that is capable of describing the image formation in the high NA regime in the latest stepper accurately. The image formation is based on Abbe formation for incoherent imaging which calculates aerial image by the integral of image formed by individual source point over entire illumination source.

4.3.1 Effect of progressive defect growth on imaging

A 6% AttPSM mask is used in the simulations using Lithocruiser™. The effect of pitches, illumination settings, defect transmission and defect phase are studied. The simulation conditions are shown in Table 4.2. This study is aimed to compare and identify the relative significance of these factors to the printability of a defect. By varying each factor at a time, the influence on the CD errors caused by the defect is observed and compared. The locations of the defects relative to the line and space pattern are shown in Fig. 4.7. Two types of defect: mid-point defect and adjacent defect are simulated. It provides observation on the influence of defect proximity to main features.



Fig 4.7 Location of simulated defect relative to main features

Table 4.2 Summary of simulation conditions for defect study

	Mid-point defect	Adjacent defect
Location of defect	Location 1	Location 2
Defect sizes (1X)	10 – 40nm	10 – 40nm
Pitch	140 , 160 , 180 , 220nm	140 , 160 , 180 , 220nm
OAI	Annular	Annular
NA	0.95	0.95
$\sigma_{in}, \sigma_{out}$	0.71 , 0.94	0.71 , 0.94

4.3.2 Modified OAI for resolution enhancement at forbidden pitch

A simulation is carried out to verify the impact of the modified illumination in minimizing the DOF and CD fluctuation at the forbidden pitch region. The CD and DOF performance obtained from conventional illumination and the proposed modified illumination are chosen as they usually exhibit a large range of fluctuation at the forbidden pitch. The mask pattern used in this study is one dimensional line and space with a target CD of 45 nm with pitches ranging from 130 nm to 500 nm on a 6% attenuated phase shift mask (AttPSM). A minimum pitch size of 130 nm is chosen based on the 2007 ITRS roadmap specification. Imaging performance including CD, DOF and overlap ratio η for a double annular source is compared with that of a conventional annular OAI with σ_{in} and σ_{out} optimized to the smallest pitch of 130 nm. This enables a fair comparison between optimum imaging performance of a conventional shape and the proposed modification. Optical proximity correction including biasing and SRAF are applied according to the mask design rules for pitches other than the smallest pitch. Table 4.3 summarizes the illumination conditions used in this study. The pitch range and OPC

applied are summarized in Table 4.4. The OPC is applied for in both the conventional and double annular sources.

A simulation is carried out to examine the feasibility of extending the concept of OAI modification to other types of source and the illumination conditions are summarized in Table 4.5. The requirements for OPC using the modified OAI are also investigated and Table 4.6 shows the illumination conditions employed for the line end shortening study.

Table 4.3 Summary of illumination conditions

Illumination Conditions	Source shape	NA	$\sigma_{out,1}, \sigma_{in,1}$	$\sigma_{out,2}, \sigma_{in,2}$
1	Double annular	1.12	0.60, 0.40	0.84, 0.67
2	Double annular	1.12	0.60, 0.50	0.84, 0.74
3	Double annular	1.12	0.60, 0.50	0.84, 0.67
Illumination Conditions	Source shape	NA	$\sigma_{out}, \sigma_{in}$	
4	Conventional annular	1.12	0.88, 0.68	

Table 4.4 Summary of pitch range (Target CD = 45 nm)

Pitch (nm)	OPC
130	No OPC
140	Biasing
150	Biasing
160	Biasing
170	Biasing
180	Biasing
190	Biasing
200	Biasing
220	Biasing
240	Biasing, SRAF
260	Biasing, SRAF
280	Biasing, SRAF
300	Biasing, SRAF

320	Biasing, SRAF
340	Biasing, SRAF
360	Biasing, SRAF
380	Biasing, SRAF
400	Biasing, SRAF
450	Biasing, SRAF
500	Biasing, SRAF

Table 4.5 Illumination conditions for other sources

Source shape	NA	$\sigma_{out,1}$, $\sigma_{in,1}$	$\sigma_{out,2}$, $\sigma_{in,2}$
Double dipole	1.10	0.50 , 0.35	0.70 , 0.60
Double quadrupole	1.05	0.40 , 0.15	0.95 , 0.80
Source shape	NA	σ_{out} , σ_{in}	
Dipole	1.10	0.55 , 0.70	
Quadrupole	1.05	0.95 , 0.80	

Table 4.6 Illumination conditions for line end shortening study

Source shape	NA	$\sigma_{out,1}$, $\sigma_{in,1}$	$\sigma_{out,2}$, $\sigma_{in,2}$
Double dipole	1.1	0.55 , 0.40	0.90 , 0.78
Source shape	NA	σ_{out} , σ_{in}	
Dipole	1.1	0.70 , 0.95	

4.3.3 Circular mask openings and radial segmentation for contact holes patterning

A simulation is performed using LithocruiserTM to investigate the performance of circular apertures for contact hole patterning according to requirement for 45 nm technology node. The targeted critical dimension (CD) of the contact holes is 80 nm and illumination conditions are optimized with the smallest pitch of 130 nm. Dimensional biasing is

applied to circular apertures of other pitches to achieve a common process window. The mask used in the simulation is a 6% Attenuated phase shift mask (AttPSM). For comparison of the performance, square apertures with optimized conditions are also employed. It is noted that the optimized conditions for both square and circular aperture are similar. Table 4.7 summarizes the simulation conditions for this study.

To investigate the effectiveness of the radial segmentation, a simulation on a staggered contact hole pattern is also performed. A circular aperture with radial segmentation, as illustrated in Fig. 4.8, is compared with conventional square aperture with serifs of similar size added at the corner. The parameters used are as follows:

- r : radius of circular openings on mask
- Δr : radial extension of a segment on the circumference of a circular opening
- θ_r : opening angle of a segment on the circumference of a circular opening

The simulation conditions for the staggered contact hole pattern are listed in Table 4.8. The OPC feature size for the staggered contact hole pattern is summarized in Table 4.9. For a mask with a square aperture, square serifs are added to four corners of the aperture.

Table 4.7 Simulation conditions for a regular contact hole array

	Circular aperture	Square aperture
Illumination		Quadrupole
NA		1.12
σ_{in}, σ_{out}		0.6, 0.9
Pitch		130 – 500 nm

Table 4.8 Simulation conditions for a staggered contact hole array

	Conventional Square Apertures	Proposed Circular Apertures
OAI source shape		Quadrupole
Numerical aperture (NA)		1.26
Partial Coherence factor ($\sigma_{in}, \sigma_{out}$)		(0.6, 0.9)
Minimum d (nm)		100
Maximum d (nm)		200
OPC method	Serifs	Radial segmentation

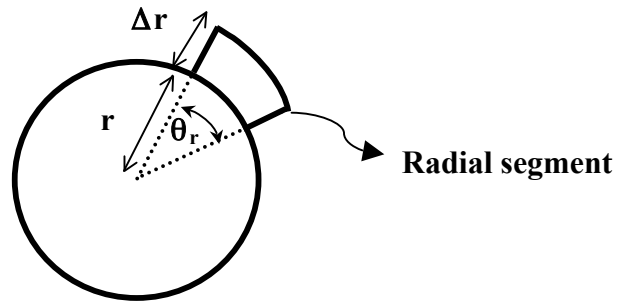


Fig. 4.8 Radial segmentation for staggered contact hole pattern

Table 4.9 OPC features size for staggered contact hole pattern

d (nm)	Conventional serifs width (nm)	Radial extension Δr (nm)
100	5	7.5
120	10	10
160	16	17.5
200	20	20

Chapter 5 Results and Discussion

The effects of mask transmission and phase change due to cleaning, and progressive growth of defects on process window are discussed in this chapter. Furthermore, the impacts of the proposed modified OAI on through pitch CD control and the process window are also presented. Finally, the consequence of contact hole patterning with circular apertures and radial segmentation approach is also examined.

5.1 Influence of mask defect

5.1.1 Resolution improvement by immersion lithography

The imaging performance between dry and immersion lithography is studied through a simulation of line and space patterning with a target CD of 45 nm. Figure 5.1 shows the CD through pitch for the dry and immersion lithography systems. For both systems, the annular illumination scheme is used with $\sigma_o = 0.86$, $\sigma_i = 0.61$ and $NA = 0.81$. These illumination conditions are optimized with the smallest pitch of 150 nm. In general, the CD through pitch performance is similar for both systems. Between 160 nm and 200 nm pitches, a 10 % CD fluctuation is observed. This can be attributed to the forbidden pitch phenomenon due to the application of OAI. While both dry and immersion lithography are able to resolve the pattern, the main difference is in the actual NA of the lens system.

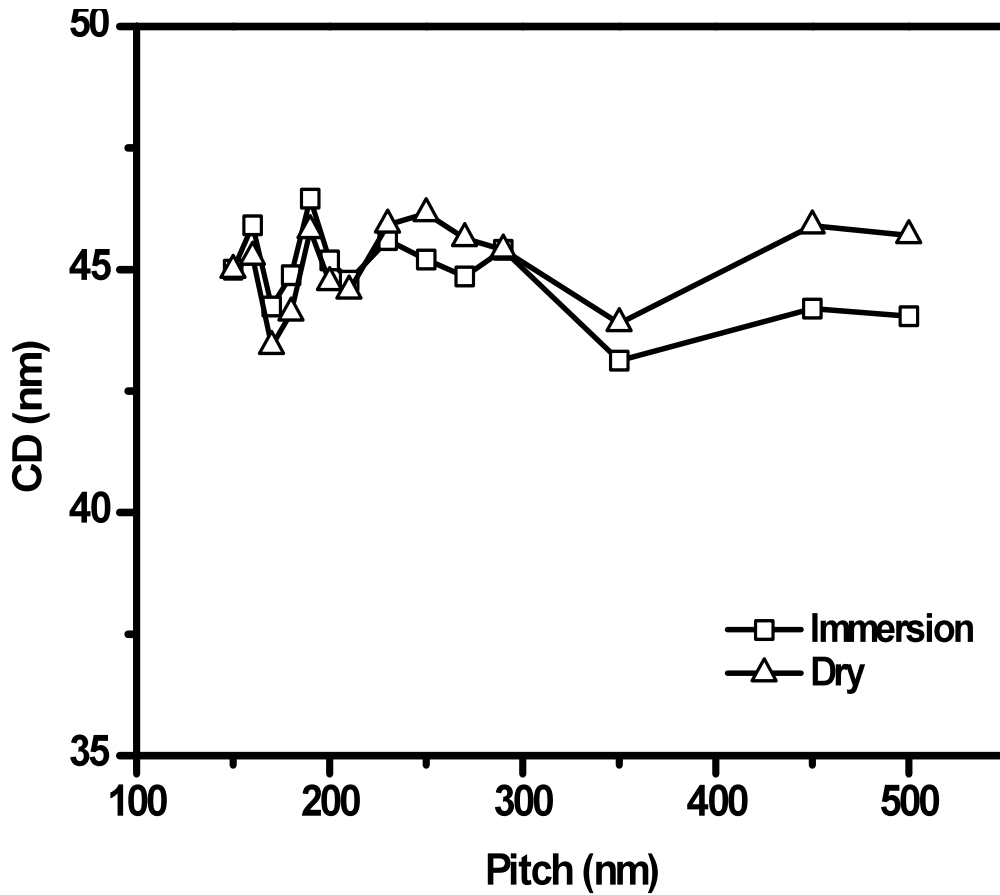


Fig. 5.1 Comparison between CD through pitch performance for immersion and dry lithography

To achieve similar CD resolution, the lens NA ($\sin \theta$) required for immersion lithography is only 0.56, compare with a NA ($\sin \theta$) of 0.81 for dry lithography system. Since the resolution limit of immersion lithography is scaled by the refractive index of the immersion medium, the effective wavelength of exposure is 135 nm (for water, $n = 1.44$). Hence, immersion lithography allows conventional lens to function at a higher NA value and improves the resolution significantly.

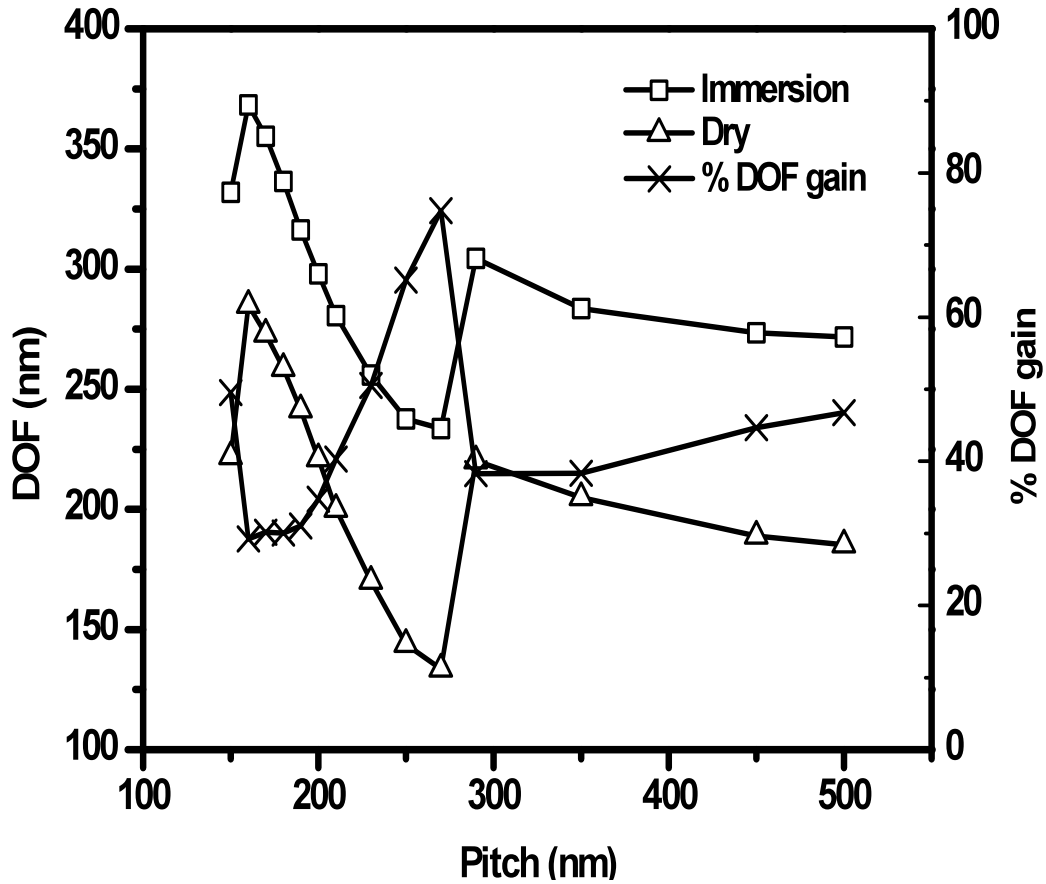


Fig. 5.2 Comparison of DOF through pitch between immersion and dry lithography

From Fig. 5.2, the CD through pitch performance indicates that both dry and immersion lithography systems are able to meet the resolution requirement. However, immersion lithography uses a smaller NA and is likely to reduce the optical path difference between any two interfering ray at the imaging plane. The reduction in the optical path difference is beneficial because it improves the DOF. Studies of the DOF through pitch for both systems to meet the 4 % exposure latitude requirement are plotted in Fig. 5.2. Since the same illumination conditions are applied in both immersion and dry lithography, the trend observed is the same for both cases. It is seen that the DOF attains a maximum value at lower pitches since the illumination settings are optimized. As the pitches

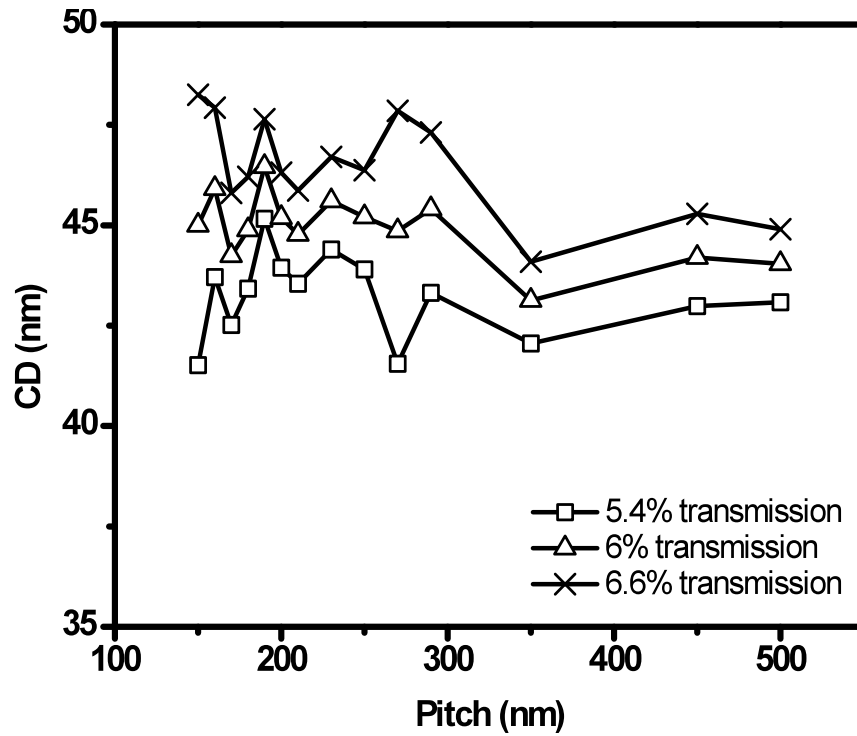
increase, the DOF degrades. However, at a pitch of 290 nm, the DOF improves due to the use of scattering bars which help to improve the image contrast. The improvement in the DOF with the implementation of the immersion system is around 40 % on the average. As shown in Eq. (2.2), DOF for dry lithography is inversely proportional to the square of NA. For a better resolution, the NA has to be increased. However this is at the expense of the DOF. Fortunately, the DOF for the immersion lithography as given in Eq. (2.15) is only inversely proportional to the square of $\sin\frac{\theta}{2}$ or the numerical half aperture (NHA) instead of the square of the NA. Hence due to smaller incident angle, the focus would be less sensitive to displacement at the wafer plane.

From this study, the immersion lithography together with an appropriate resolution enhancement scheme would be capable of fulfilling the resolution and DOF requirement of the 45 nm technology node.

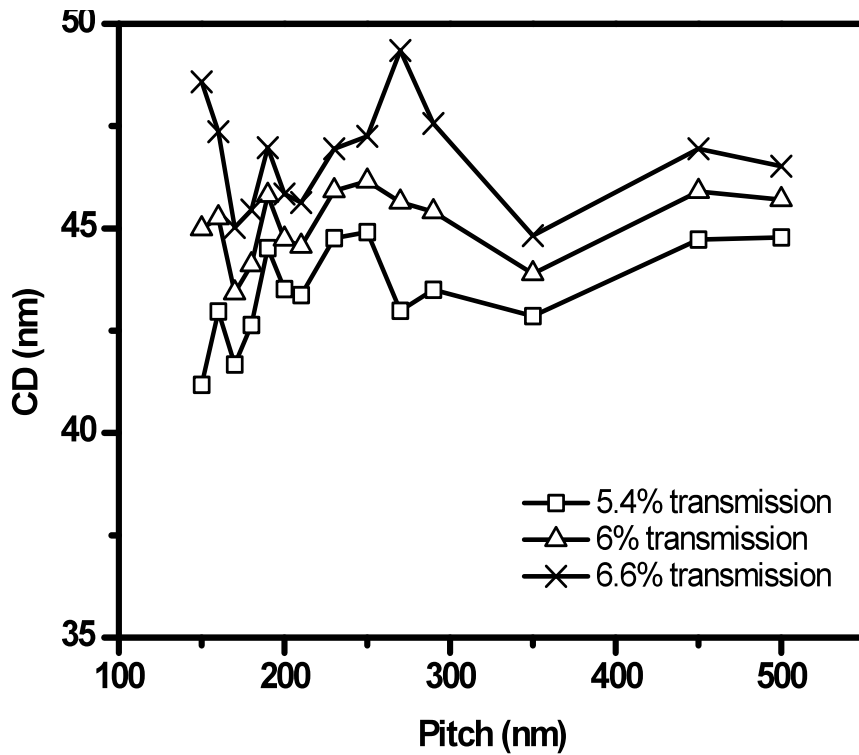
5.1.2 Critical factors in defect printability

5.1.2.1 Effect of changes in mask transmission

Mask cleaning often induces damages to the MoSi on a AttPSM and causes a change in transmission. To simulate the effect of a $\pm 10\%$ change in transmission, CD through pitch obtained at transmissions of 5.4 %, 6.0 % and 6.6 % are investigated and plotted as shown in Figs. 5.3a and 5.3b.



(a)



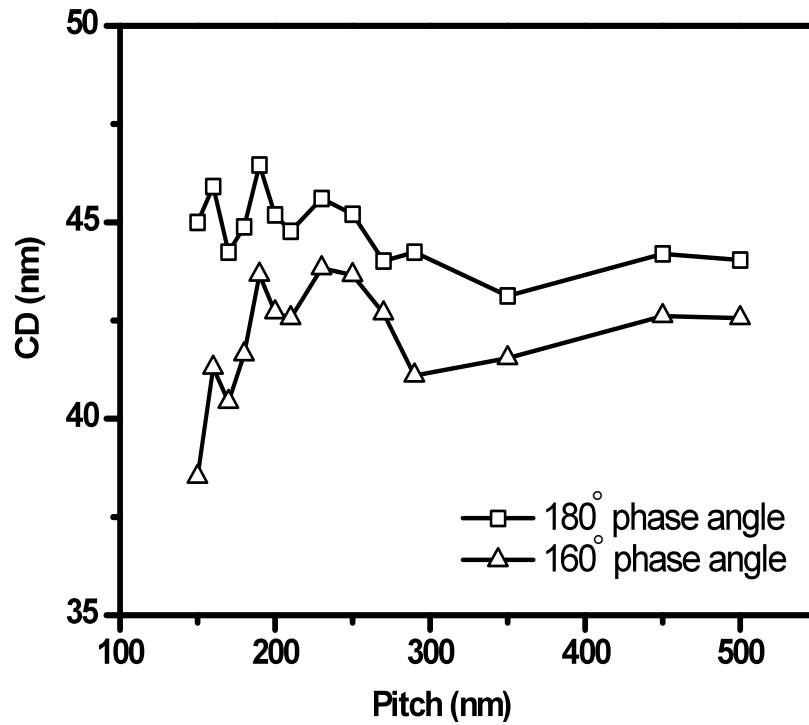
(b)

Fig. 5.3 Changes in CD as a result of mask transmission error (a) immersion ; (b) dry

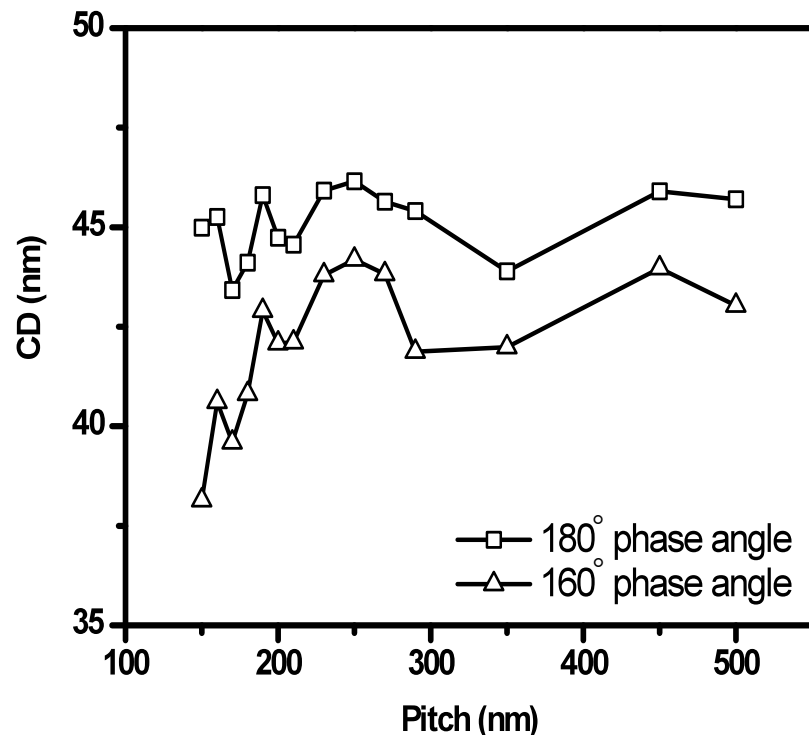
Under the same exposure conditions, simulated results show that an increase in transmission will increase the CDs and vice versa. As the transmission of the MoSi phase shifter increases to 6.6 %, the amplitude of the light passes through it increases. If the phase shifted light interferes with the light transmits through the quartz, the resultant amplitude is decreased (i.e. to below that of a 6 % transmission). As a result, the printed CD increases.

The change in CD due to a change in mask transmission is not constant for different pitches. Figure 5.3b shows that 150 nm and 270 nm pitches indicate the largest CD variation at 6.6 % transmission. At a pitch of 150 nm, the lithography system is near its resolution limit. Hence, the printed image is very sensitive to a change on the mask. As seen from Fig. 5.2, the DOF improves for larger pitches but degrades for pitches beyond 200 nm. This indicates that the image contrast is poorer for the intermediate pitch range from 200 nm to 270 nm. Thus, at 270 nm pitch, the DOF is the lowest and the poor image contrast increases its sensitivity to mask transmission error. When a scattering bar is inserted, the DOF uniformity for pitches of 290 nm and above is improved and it can be seen that the changes in the CD due to transmission shift fluctuates relative less.

5.1.2.2 Effect of changes in mask phase



(a)



(b)

Fig. 5.4 Changes in CD as a result of mask phase error (a) immersion ; (b) dry

During the cleaning process, the thinning of MoSi changes the phase angle of the light passing through it. Figs. 5.4a and 5.4b show the CD through pitch when the phase angle drops from 180° to 160° for both the dry and immersion systems. A smaller and wider CD spread is observed for the 160° phase angle.

From the results obtained above, it can be seen that the sensitivity of the lithography process to the overall mask transmission and phase change is strongly dependent on the pattern density. At a small pitch size near the resolution limit of the lithography system, the sensitivity is higher. It is to be noted that there are also some intermediate pitches which show high sensitivity because of poor image contrast due to the through pitch fluctuation of the image contrast resulted from the application of the OAI.

5.1.2.3 Effect of pattern density

The progressive growth of mask defect or haze is one of the most commonly encountered issues in 193 nm lithography. Understanding of defect interaction with mask main features is helpful on defect disposition. Figure 5.5 shows the experimental and simulated results for an active layer of SRAM cell. The variation in CD for defect size ranging from 15 nm to 50 nm is shown. In general, the simulation agrees well with the experimental results. However, there is a noticeable scatter of experimental results at 30 nm and 50 nm defect size due to uneven resist profile at these locations, which results in a large difference between the two sets of results. Nonetheless, the difference in CD between the simulated and experimental results is less than 10 % at these defect sizes. It is seen that as the defect size increases, the CD variation for the main feature increases. For an adjacent defect, the variation in CD with a 50 nm defect shows a 12 % increase compared to a 15

nm defect. It is also seen that to limit the CD variation to 10 %, the defect size should be below 35 nm. For a mid-point defect, an increase in a defect size from 15 nm to 50 nm would result in a 3 % increase in the CD variation. It is also seen that the adjacent defects show a more significant influence on the CD variation than the mid-point defects.

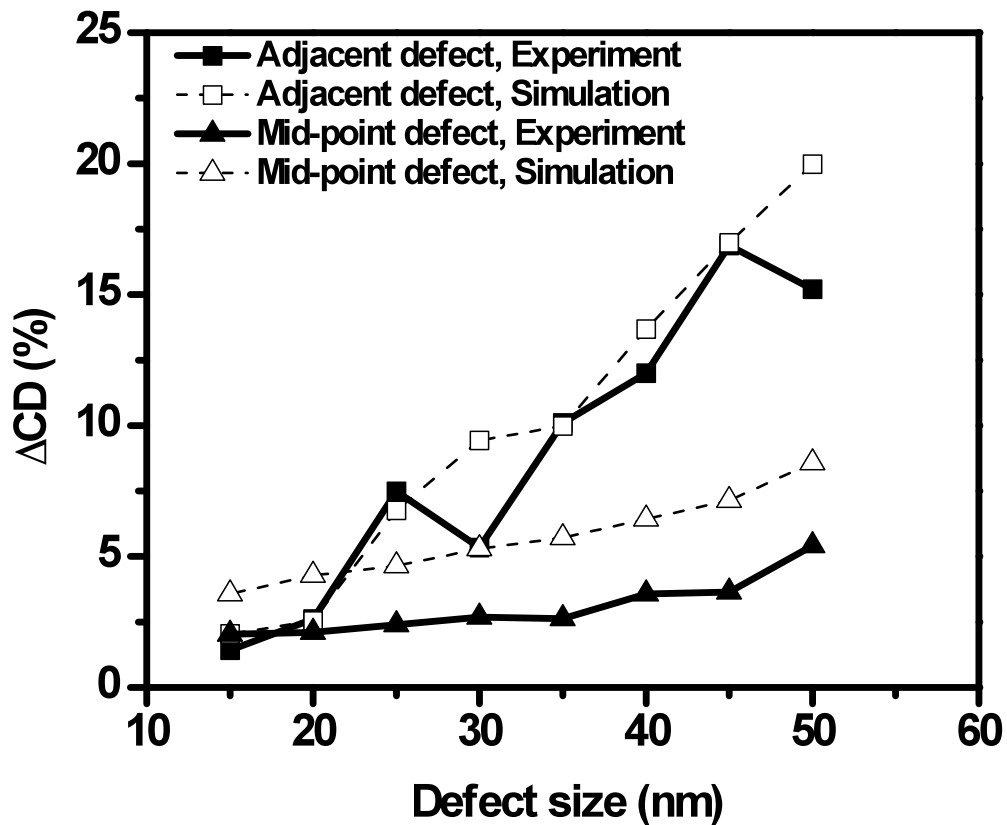


Fig. 5.5 CD variation for an active layer with adjacent and mid-point defects

Figure 5.6 shows the CD variation of the experimental and simulated results for a polysilicon layer of a SRAM cell. Similar to the results shown in Fig. 5.5, a larger defect size would result in a larger CD variation. For an adjacent defect, the experimental results show that the CD variation increased by 20 % as the defect size increases from 15 nm to 50 nm. Similar results are obtained from simulation though there are some noticeable discrepancies. This is because a calibrated threshold resist model is used, which does not

capture the post bake and development process. However, the maximum CD difference between the experimental and simulated results is within 10 %. For a mid-point defect, the experimental results also show an increase in CD variation with an increase in defect size. This is also evident from the simulation results. There are again some discrepancies between the experimental and simulated results. This is due to the fact that resist post back and development are not captured in the threshold resist model used. It is also seen that there are some scatter in the experimental results. This is due to uneven resist profile at those points. Nevertheless, the maximum CD difference between the experimental and simulated results is within 10 %. As seen in the results, adjacent defects show a more significant effect on the CD variation than mid-point defects.

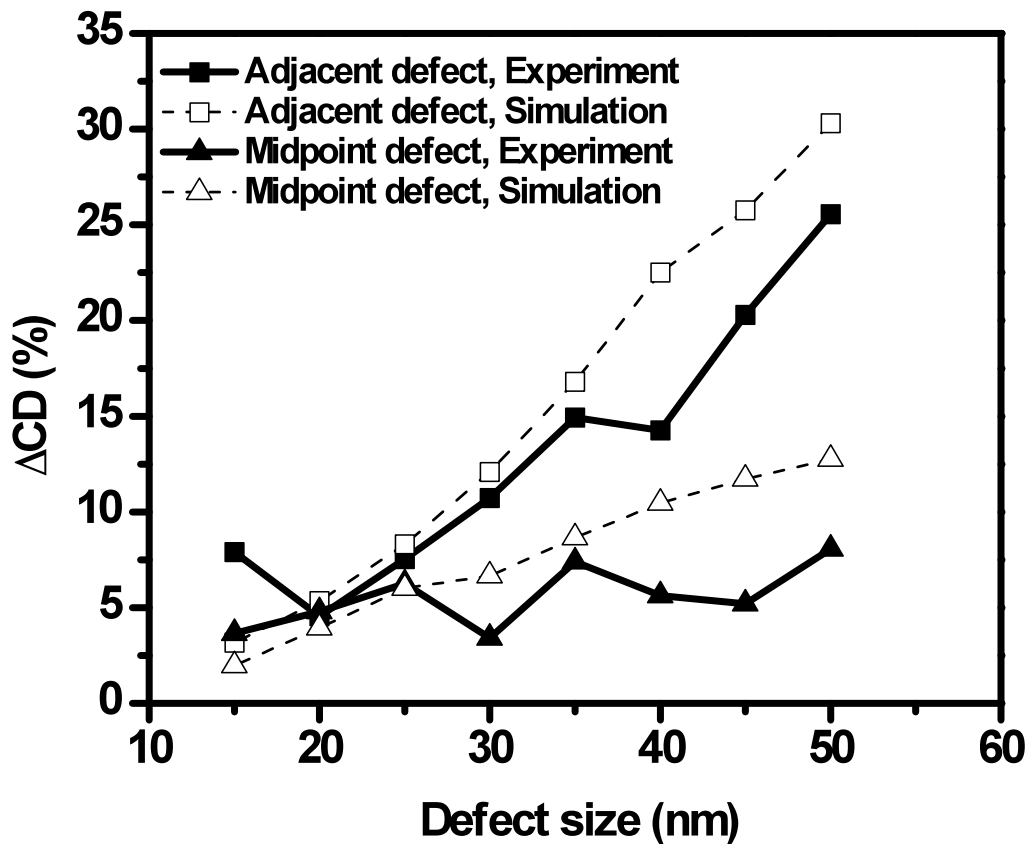


Fig. 5.6 CD variation for a polysilicon layer with adjacent and mid-point defects

The CD variation caused by an adjacent defect for an active and a polysilicon layer is shown in Fig. 5.7. The results show an increase in CD as the defect size increases and the maximum CD variation of the polysilicon layer is 10 % higher than that of the active layer. The results also show that a polysilicon layer would experience a larger CD change than an active layer. This is due to the smaller pitch of the polysilicon layer.

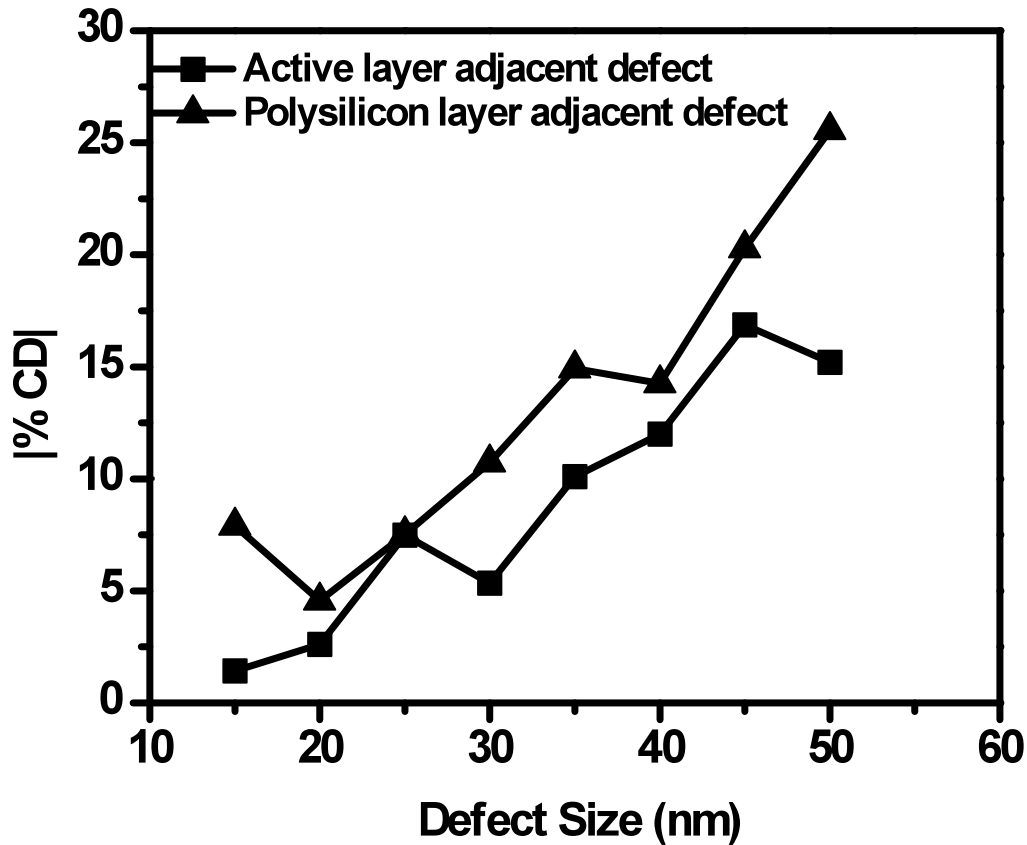


Fig. 5.7 Comparison of experimental CD variations for an active and polysilicon layer with adjacent defect

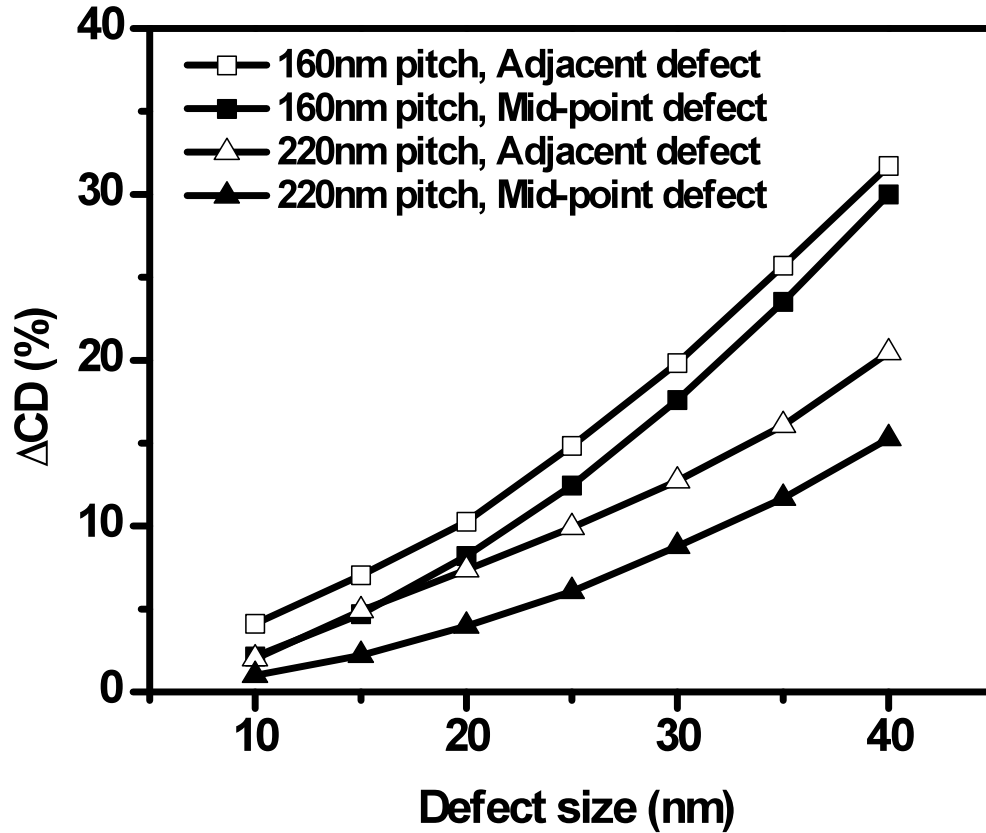


Fig. 5.8 Simulated CD variation of 160 nm and 220 nm pitch with adjacent and mid-point defects ($T_d = 6\%$, $\phi_d = 180^\circ$)

Figure 5.8 shows the simulated CD variation for 160 nm and 220 nm pitch with defect sizes ranging from 10 nm to 40 nm. The defects are assumed to be similar to process related defects which have 6 % transmission and 180° phase shift. Generally, it can be seen that as defect size increases, the CD variation increases. For an adjacent defect, the maximum CD variation of a 40 nm defect is about 35 % at a pitch of 160 nm. The critical defect size defined as more than 10 % of the CD variation is 20 nm. For the 220 nm pitch, the maximum CD variation is 24 % at a defect size of 40 nm and the critical defect size is 25 nm. From the results, it is seen that the maximum CD variation of the 160 nm pitch is 11 % higher than that of the 220 nm pitch. Also, it is observed that the 220 nm

pitch has a larger critical defect size than the 160 nm pitch. For a mid-point defect, the maximum CD variation for a 160 nm pitch and 40 nm defect size is about 32 % and the critical defect size is 25 nm. While for a 220 nm pitch, the maximum CD variation is about 14 % and the critical defect size is 35 nm. Hence, patterns with smaller pitches would result in higher defect printability. In addition, as can be seen from the results shown in Fig. 5.5 and Fig. 5.6, adjacent defects have a more significant influence on the CD variation than mid-point defects.

Figure 5.9 shows the simulated CD variation for defects with 0° phase and 0 % transmission. Similar to the results shown in Fig. 5.6, increasing the defect size results in an increase in the CD variation. For an adjacent defect, the CD variation of 160 nm pitch is 10 % higher than that of a 220 nm pitch and the critical defect size for a 160 nm pitch is 20 nm while that of a 220 nm pitch is 25 nm. Hence, a smaller pitch would suffer a higher CD degradation with the presence of a haze defect. For a mid-point defect, the maximum CD variation of a 160 nm pitch is 15 % higher than that of a 220 nm pitch. The critical defect size for a 160 nm pitch is 25 nm and that for a 220 nm pitch is 35 nm. Similarly, patterns with smaller pitches result in higher CD variation. Likewise an adjacent defect results in a higher CD variation than a mid-point defect.

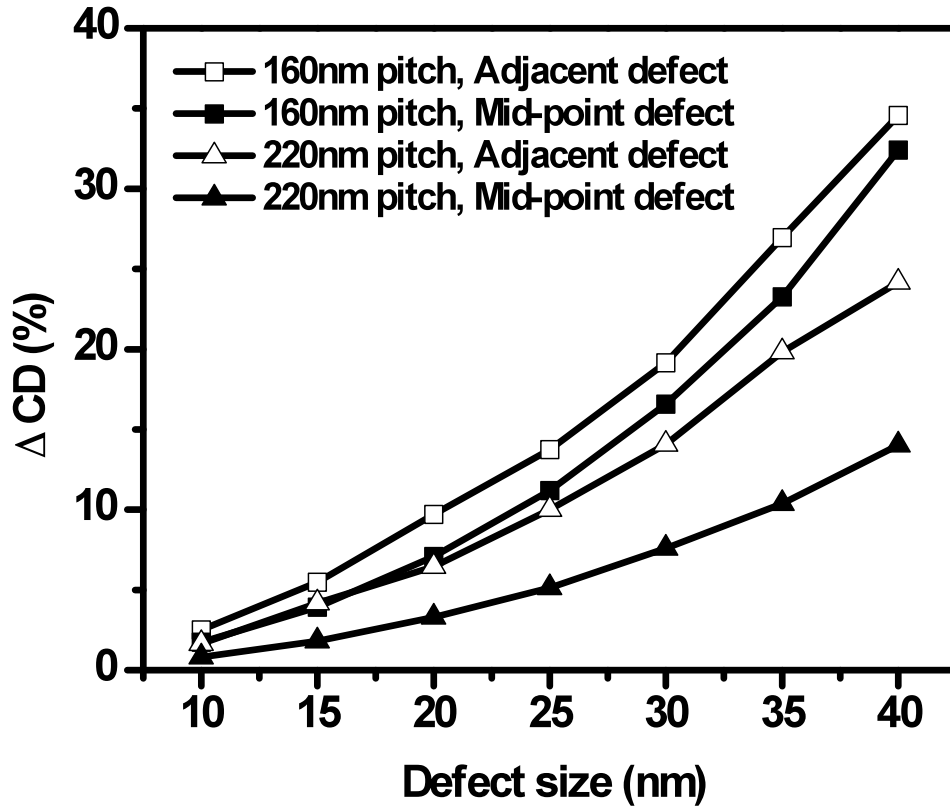


Fig. 5.9 Simulated CD variation of 160 nm and 220 nm pitch with adjacent and mid-point defects ($T_d = 0\%$, $\phi_d = 0$ degree)

From the results above, it can be observed that in the presence of a defect, the CD variation increases with smaller pattern density and defect that is closer to the main feature would result in a more severe degradation in the CD. Larger defects have a more significant influence on the CD variation.

5.1.2.4 Effect of transmission

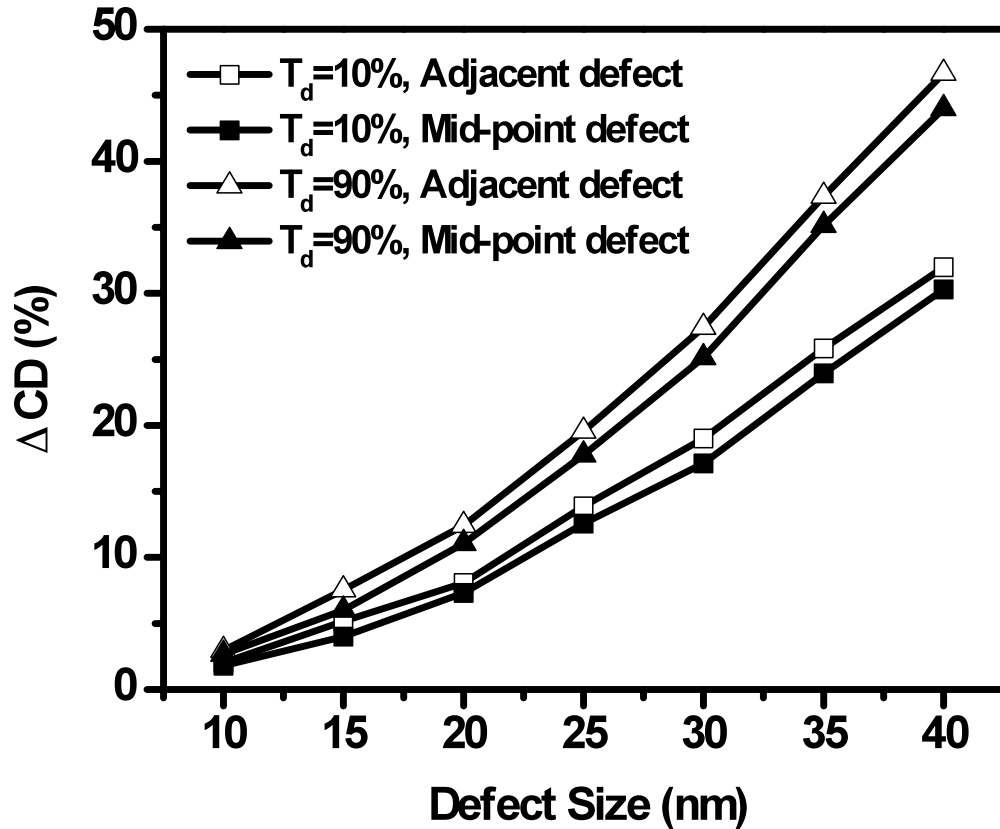


Fig. 5.10 Simulated CD variation of 180 nm pitch with adjacent and mid-point defects and different transmissions ($\phi_d = 180^\circ$)

Figure 5.10 shows the simulated results of CD variation of a 180 nm pitch for defects with 180° phase shift for both types of defect at different levels of transmission. It is seen that the CD variation increases with defect size. For an adjacent defect, a lower transmission would result in a smaller CD variation. The results also show that the difference in CD variation between the two levels of transmission (10 % and 90 % transmissions) increases with the defect size. For a defect size of 15 nm with 90 % transmission the CD variation is 2 % higher than that with 10 % transmission. However, for a defect size of 40 nm, the corresponding CD variation increases to 15 %.

Nonetheless, the change in transmission level does not cause a shift in the critical defect size. For a mid-point defect, the characteristics behavior show similar trend and the transmission level also does not cause a shift in the critical defect size.

Figure 5.11 shows the simulated CD variations of 180 nm pitch for defects with different levels of transmission. The simulated defects contain no phase shift, which closely resemble thin haze defects. In general, it is observed that as the defect size increases, CD variation increases. For an adjacent defect, a defect at 90 % transmission results in a low CD variation of only about 1 %. While a lower transmission (10 %) would result in a larger CD variation. For a midpoint defect, the behavior is similar to that of an adjacent defect with a 1 % CD variation at 90 % transmission. This is also evident from Eq. (3.12) which indicates a higher CD variation with lower transmission. In general the influence of an adjacent defect on the CD variation is also more prominent than that of a mid-point defect. For a 40 nm defect with 0 % transmission, the CD variation of mid-point defect is about 2 % less than that of an adjacent defect. However, defects with a higher transmission of 90 % do not show significant difference in the CD variation. This is due to the 0° phase shift assumption and thus defects with 90 % transmission are almost transparent.

From the results above, it can be seen that for process induced defects that have a 180° phase shift, a higher level of transmission would result in higher CD variations. However, for haze defects with 0° phase shift, CD variations increase with lower levels of transmission.

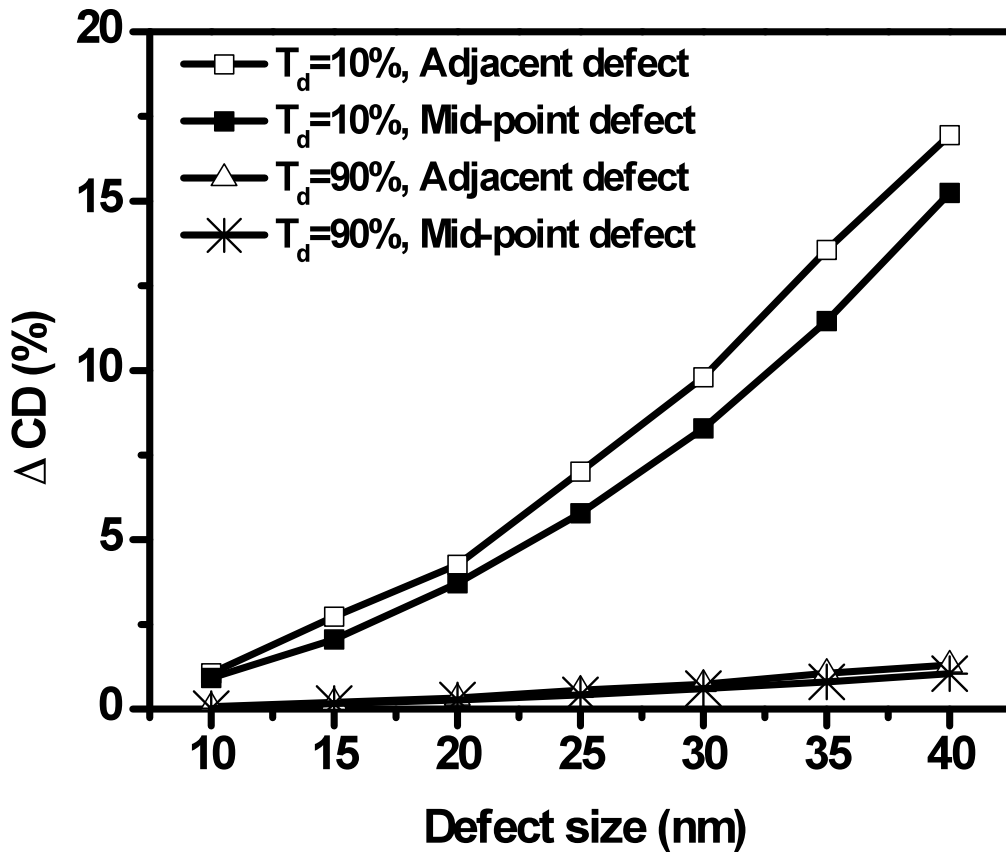


Fig. 5.11 Simulated CD variation of 180 nm pitch with adjacent and mid-point defects and different transmissions ($\phi_d=0^\circ$)

5.1.2.5 Effect of phase shift

Figure 5.12 shows the simulated CD variation of a 180 nm pitch for an adjacent defect of various phase shifts at 10 % transmission. In general, CD variation increases with defect size and for a defect size an increase in phase shift would increase the CD variation. For a particular defect size (20 nm), the CD variation of a 180° phase shift is 4 % higher than that of a 0° phase shift. However as the defect size increases, the difference in CD variation is amplified. The results also show that the critical defect size increases with a reduction in phase shift.

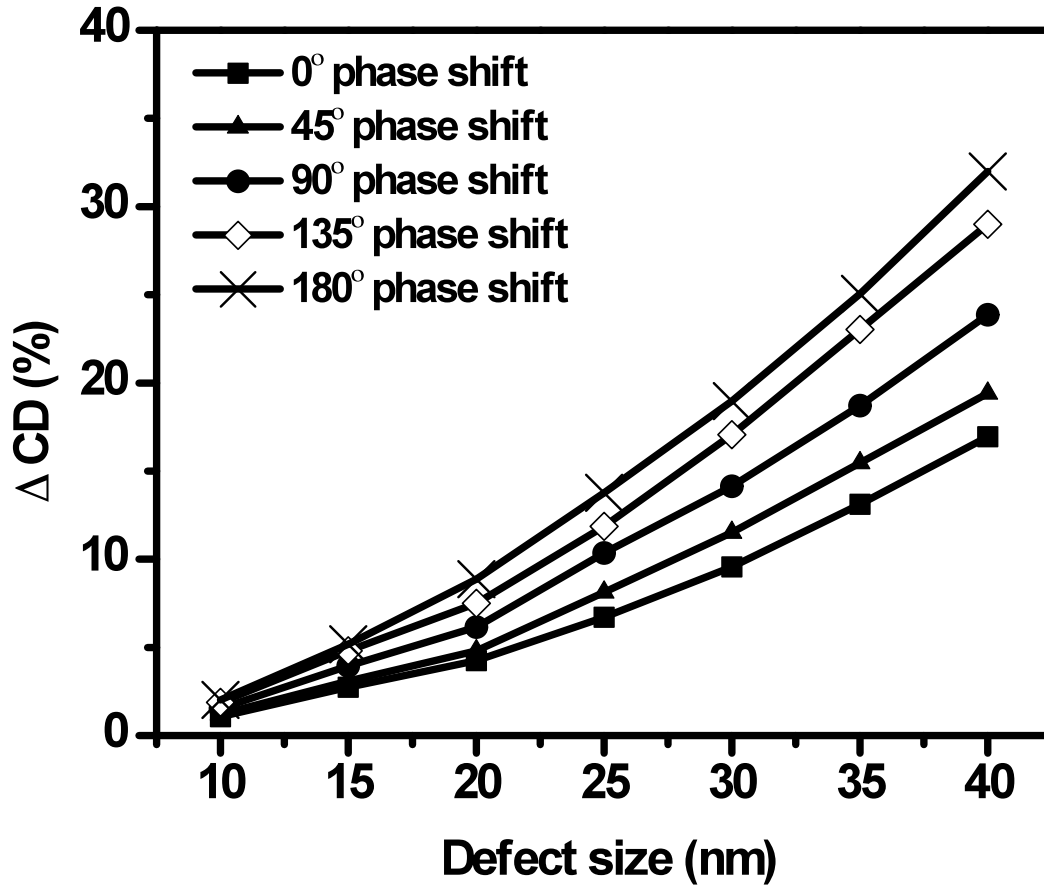


Fig. 5.12 Simulated CD variation of 180 nm pitch with adjacent defects and different phase shifts ($T_d = 10\%$)

Figure 5.13 shows the simulated CD variation of a 180 nm pitch for a mid-point defect of various phase shifts at 10 % transmission. The results are similar to that of an adjacent defect as shown in Fig. 5.12 and defects with a larger phase shift would result in a higher CD variation. A reduction in the phase shift would also result in an increase in the critical defect size.

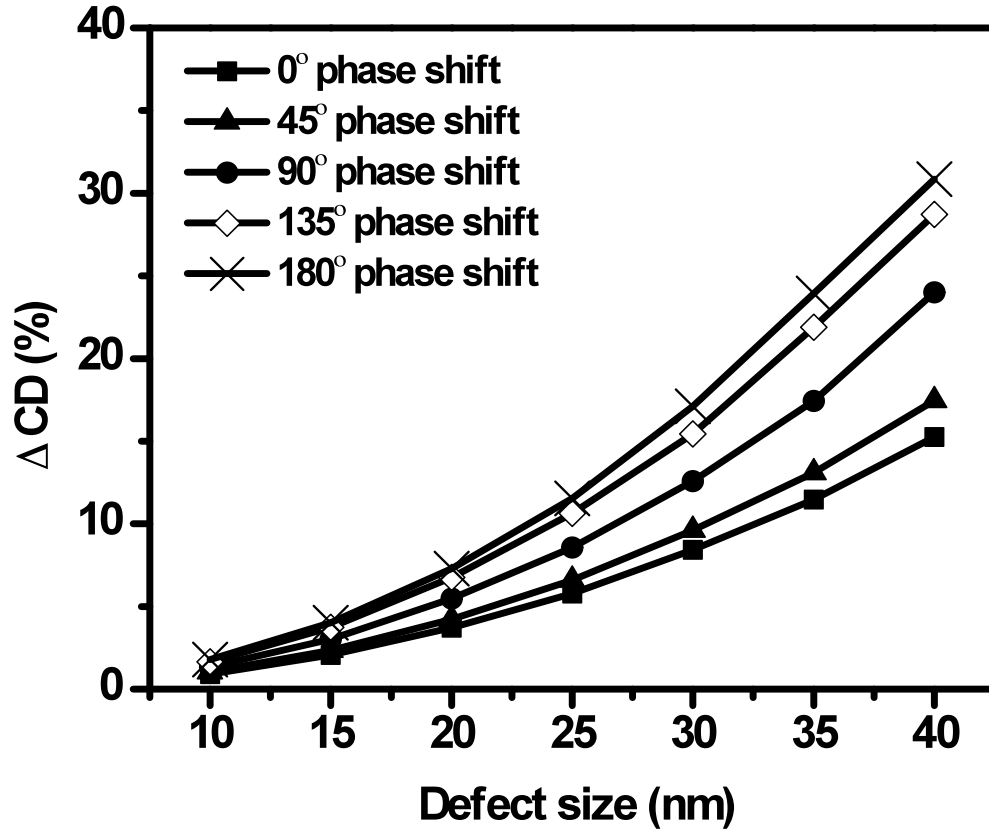


Fig. 5.13 Simulated CD variation of 180 nm pitch with mid-point defects and different phase shifts ($T_d = 10\%$)

5.1.2.6 Effect of partial coherence

Figure 5.14 shows the simulated CD variation of a 140 nm pitch of an adjacent defect with different partial coherence settings (σ_{in}). The defects are opaque and do not cause a phase shift. In general, the CD variation increases with defect size and a decrease in the partial coherence setting would increase the CD variation.

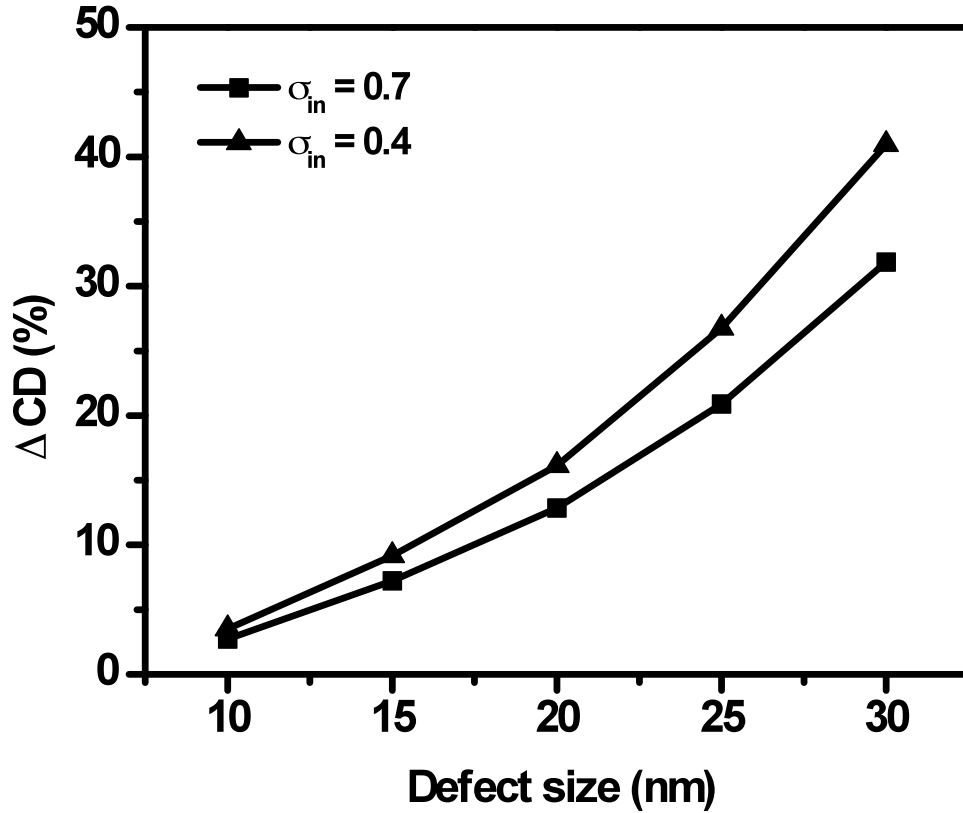


Fig. 5.14 Simulated CD variation of 140 nm pitch with adjacent defects and difference partial coherence settings (Annular OAI, $\sigma_{out} = 0.94$, $T_d = 0\%$, $\phi_d = 0^\circ$)

Figure 5.15 shows the simulated CD variation of a 140 nm pitch of a mid-point defect for different partial coherence settings (σ_{in}). Similarly the CD variation increases with the defect size and decreasing the partial coherence setting (σ_{in}) results in an increase of the CD variation. Hence a lower partial coherence setting would result in higher defect printability.

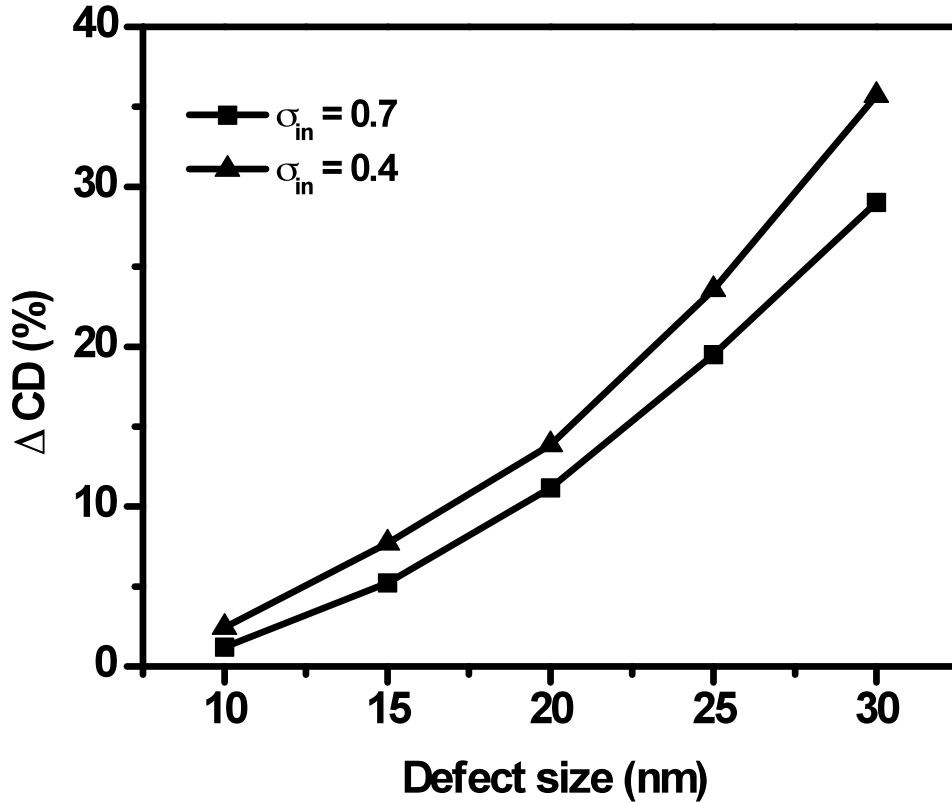


Fig. 5.15 Simulated CD variation of 140 nm pitch with mid-point defects and different partial coherence settings (Annular OAI, $\sigma_{out} = 0.94$, $T_d = 0\%$, $\phi_d = 0^\circ$)

5.1.3 Comparison of contributing factors

Table 5.1 shows a summary of the maximum difference in CD variation for each of the factors studied. Among all the factors considered, the defect size shows the most significant contribution to the CD variation of 27 %. This observation agrees well with Eq. (3.10), whereby the CD variation is a second order function of the defect size. The defect location is the second contributing factor and results in 20 % to the CD variation. The next factors (in order of significance) are the pitch, transmission, phase shift and partial coherence.

Table 5.1 Influence of different defect parameters

Rank		Maximum difference in ΔCD (%)
1	Defect size	27
2	Defect location	20
3	Pattern pitch	18
4	Defect transmission	17
5	Defect phase	15
6	Partial coherence	10

5.2 Illumination optimization for off axis illumination

5.2.1 CD, DOF and η for single and double annular sources

The proposed concept of customized illumination is investigated by simulating the printing of line and space pattern with different pitches. Annular OAI is one of the most common source shapes used in lithography for patterning of line and space pattern. By applying the proposed concept, a double annular source shape is obtained. The effect of a double annular source on CD fluctuation, DOF degradation, and overlapping ratio η is studied and compared with that of an optimized conventional annular source shape.

5.2.1.1 CD through pitch comparison

Figure 5.16 shows the CD through pitch performance of a conventional single annular and the proposed double annular sources with illumination setting conditions 3 and 4 as shown in Table 4.3. For the single annular source, there is a significant amount of CD fluctuation at pitches ranging from 170 nm to 200 nm. The CD decreases from 47 nm to 43 nm when the pitch increases from 170 nm to 180 nm; a variation of around 9% of nominal CD 45 nm. The largest CD of 47.3 nm occurs at a pitch of 200 nm pitch, which is around 5% of the targeted CD of 45 nm. From the CD through pitch characteristics, the forbidden pitch region is found to be around 170 nm to 200 nm due to the observed CD fluctuation in this region. As shown in Table 4.4, SRAF can not be applied for pitches in this region since the spaces in between the features are not large enough. Hence, only biasing on the features is applied. However, it is insufficient to achieve a uniform CD through pitch. SRAF can be inserted for pitches above 240 nm and the CD fluctuation is reduced due to improvement in image quality.

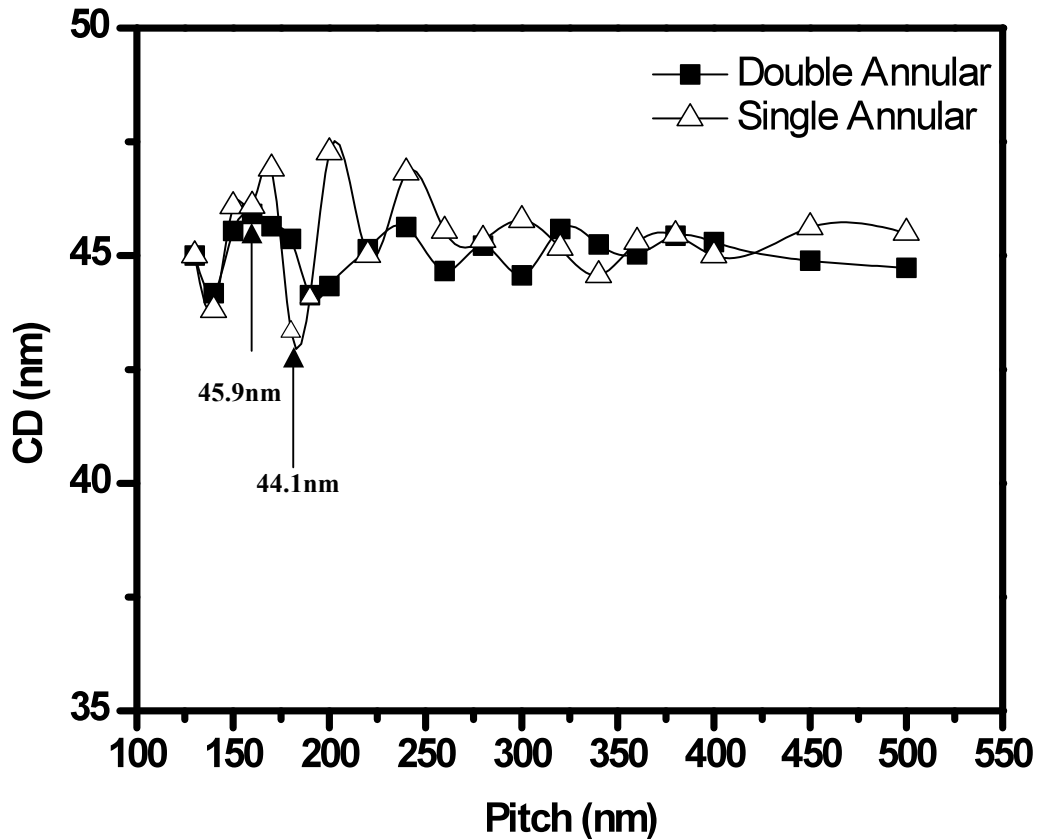


Fig. 5.16 CD through pitch for a double annular source (Condition 3) and conventional annular source (Condition 4)

Critical dimension through pitch for double annular source shows that the extent of the CD fluctuation is reduced at the forbidden pitch region of 170 nm to 200 nm. Overall, the CDs are well within $\pm 10\%$. The maximum CD deviation is 45.92 nm which occurs at a 160 nm pitch. The maximum CD fluctuation occurs from 180 nm to 190 nm and the CD decreases from 45.4 nm to 44.1 nm, which is around 3% of the target CD of 45nm. From the CD through pitch results, the double annular source shape is able to minimize the CD fluctuations and deviations at the forbidden pitch region. As in conventional annular source, only biasing is used for pitches less than 240 nm. This enables a comparison between the imaging performances resulting purely from the illumination source. As seen

in the results, though only biasing is applied at pitches from 170 nm to 200 nm, the double annular source shape is able to minimize the CD fluctuations resulting in a relatively uniform CD through pitch. The improvement in CD uniformity and control through pitch indicates that through application of the double annular source shape, CD fluctuation resulted from forbidden pitch effect can be minimized.

5.2.1.2 DOF through pitch comparison

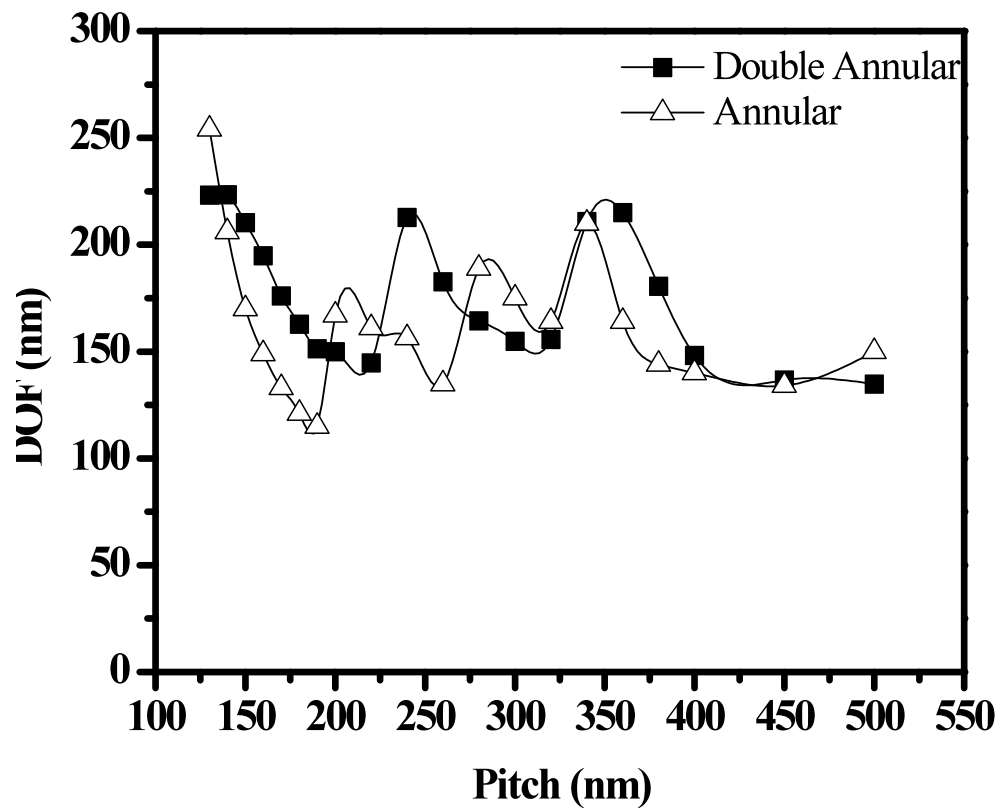


Fig. 5.17 DOF through pitch for double annular source (Condition 3) and conventional annular source (Condition 4)

Figure 5.17 shows the DOF through pitch for both annular and double annular sources with settings of condition 3 and 4 as shown in Table 4.3. For the conventional annular source, the DOF was reduced to below 150 nm for pitches ranging from 170 to 200 nm. This is not desirable and would affect the CD and DOF performance at the 170 nm to 200

nm range. Since SRAF insertion cannot be introduced, this region becomes the forbidden pitch region for the conventional annular source. As the illumination setting is optimized to the smallest pitch, the optimum source point moves further away from that of the smallest pitch according to Eq. (3.26). Consequently, the phase difference between the 0th and 1st order light at larger pitches increases and thus results in the degradation of image contrast and DOF. There is a pitch range in which the 0th and 1st order light interfere destructively and reduces the image contrast. This occurs in the 170 nm to 200 nm pitch range.

Better DOF is observed for double annular illumination than the single annular illumination. From 170 nm to 200 nm pitch range, the DOF is above 150 nm indicating an improvement in the forbidden pitch region. However, for pitches of 200 nm to 220 nm the DOF is smaller than that of single annular illumination. This is because the double annular illumination introduces additional background light (0th order light) and since 2nd order light is not collected, a reduction in the overlap ratio between the 0th and 1st occurs. Similarly, at the smallest pitch, DOF is lower for double annular source due to the influence of additional background light. From the DOF through pitch performance, it is seen that double annular source is effective in improving DOF of the forbidden pitch.

5.2.1.3 Overlap ratio η comparison

The effect of implementing double annular source on the overlapping of diffraction order is examined. Figure 5.18 shows a plot of overlap ratio η for pitches up to 190 nm. It can be observed that η has a direct relationship with DOF. For the conventional annular illumination, it can be seen that the η reduces rapidly as the pitch increases from 130 nm

to 170 nm (reduces from 0.3 to 0.15 for this range). This results in a decrease in DOF from 254 nm to 130 nm a 49% reduction. Consequently, the DOF is well below 150 nm for pitches ranging from 170 nm to 190 nm. It is seen that η should be maintained above 0.15 to achieve a DOF of at least 150 nm. Since the illumination setting is optimized for 130 nm, the overlap ratio η is the largest at this pitch and decreases as the pitch increases. For pitches ranging from 130 nm to 200 nm, only the 0th and 1st order light is collected in the pupil plane. As the pitch increases from 130 nm, the 1st order light moves towards the center of the pupil plane resulting in decreasing η . Beyond 200 nm, the 2nd order light is collected at the pupil plane resulting in an improvement in DOF. Sub-resolution assist features are inserted at the 240 nm pitch and it can be seen that the DOF is improved. The DOF reduces steadily beyond 240 nm pitch until an insertion of the second SRAF at 340 nm.

For the double annular illumination, from 130 nm to 170 nm pitch, there is a relatively smaller reduction of η compared to that of single annular illumination. In this region, the DOF decreases by 21% compared to 49% for the conventional annular illumination. The influence of forbidden pitch is reduced compared to that of conventional annular. In general, the reduction in η and DOF as the pitch increases from 130 nm to 190 nm is relatively smaller than that of single annular illumination. However, it is seen that the η and DOF at 130nm pitch is less than that of single annular source shape. This is due to additional 0th order light resulting in a smaller η as can be seen in Fig. 3.5. The η and DOF are better than that of single annular illumination at the forbidden pitch region. Overall, the DOF is maintained above 150 nm and the η does not decrease below 0.15. The results thus show that an addition of second annular improves the overlap ratio η at

the forbidden pitch and minimize the loss of DOF. The inner annular has provided an additional overlap between 0th and 1st order light in the pupil plane and thus improved the image contrast and DOF.

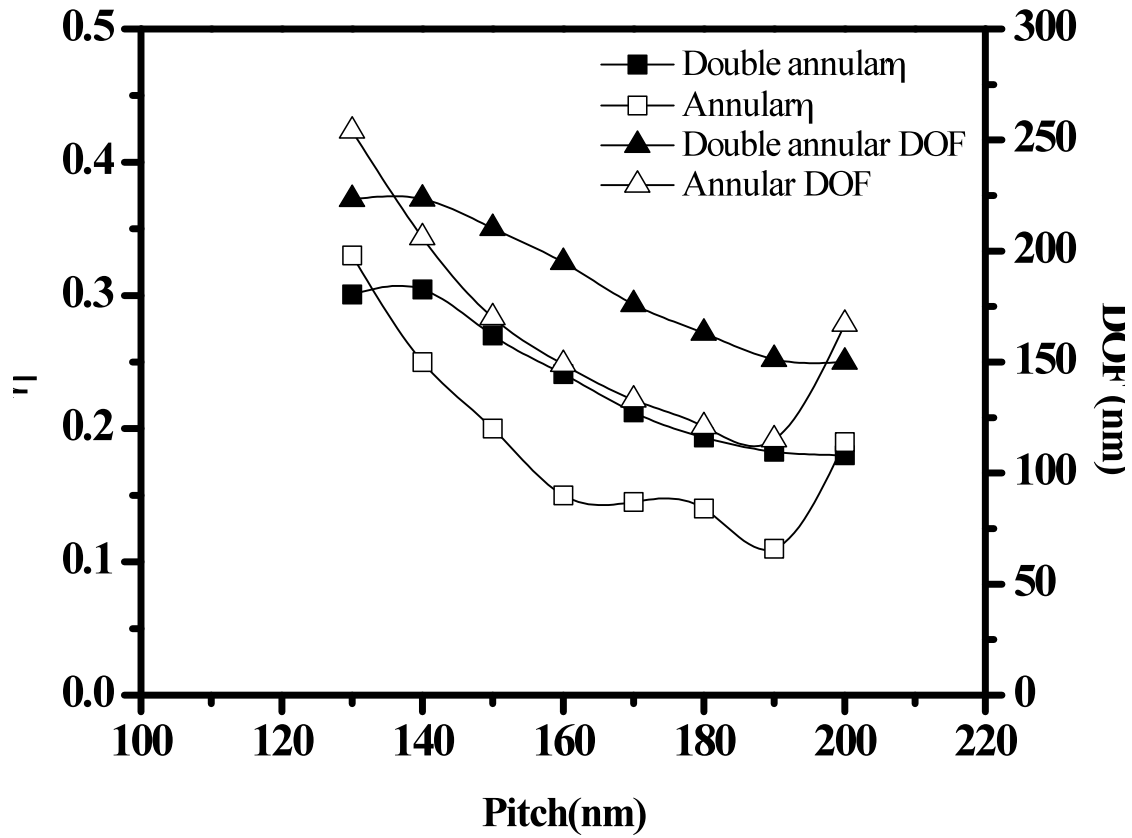


Fig. 5.18 Overlapping factor η and DOF for a double annular (Condition 3) and conventional annular (Condition 4)

5.2.2 Optimization based on η for double annular source shape

Figure 5.19 shows optimum values of σ calculated using Eq. (3.14) for pitches of 130 nm to 190 nm. The optimum source point shifts towards the center of the illumination plane as the pitch increases. Hence, for a single annular OAI a larger annular thickness ($\sigma_{out} - \sigma_{in}$) would be required to include optimum source points for every pitch.

However, a larger thickness will cause degradation in the DOF and η . Hence, conventional annular illumination can only be optimized up to a certain pitch. Biasing and SRAF are applied at other pitches so that images can be formed in a single exposure and η is maximized so that a large DOF can be obtained at the smallest pitch.

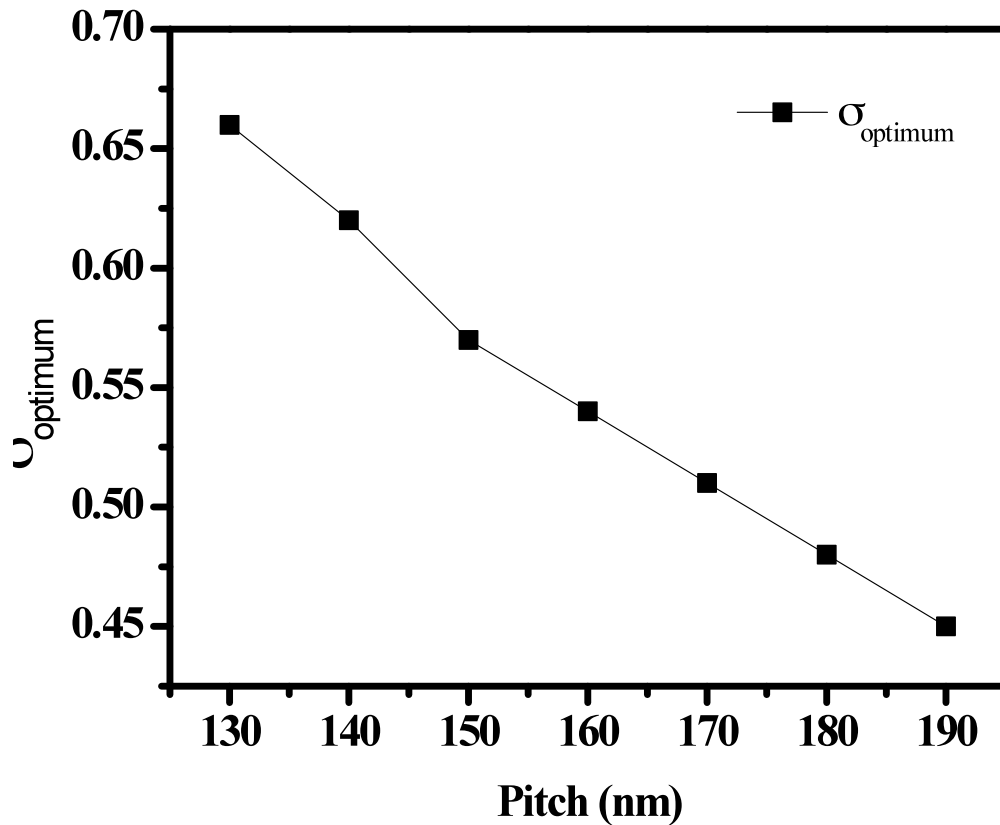


Fig. 5.19 Optimum partial coherent values for different pitches

In order to improve the η , it is desirable to have a larger partial coherent setting for smaller pitch size and smaller partial coherent setting for larger pitch size (as shown in Fig. 3.11). However, this can not be realized using the conventional OAI. Figure 5.20 shows the variation of DOF and η at 130 nm pitch for a single annular source with constant σ_{out} (0.88) and varying σ_{in} . The optimized value of σ_{in} is 0.68, which corresponds to an annular thickness of 0.2, resulting in a DOF of 253 nm and η of 0.33.

To include the optimum source points for pitches from 170 nm to 200 nm, the annular thickness can be increased by reducing σ_{in} . This would however decrease the DOF and η . For example, when σ_{in} is reduced to 0.48, η is reduced to 0.22 and DOF is also reduced to 184 nm, a 28% in the DOF. Thus, a single annular illumination with larger annular thickness will not improve the imaging performance.

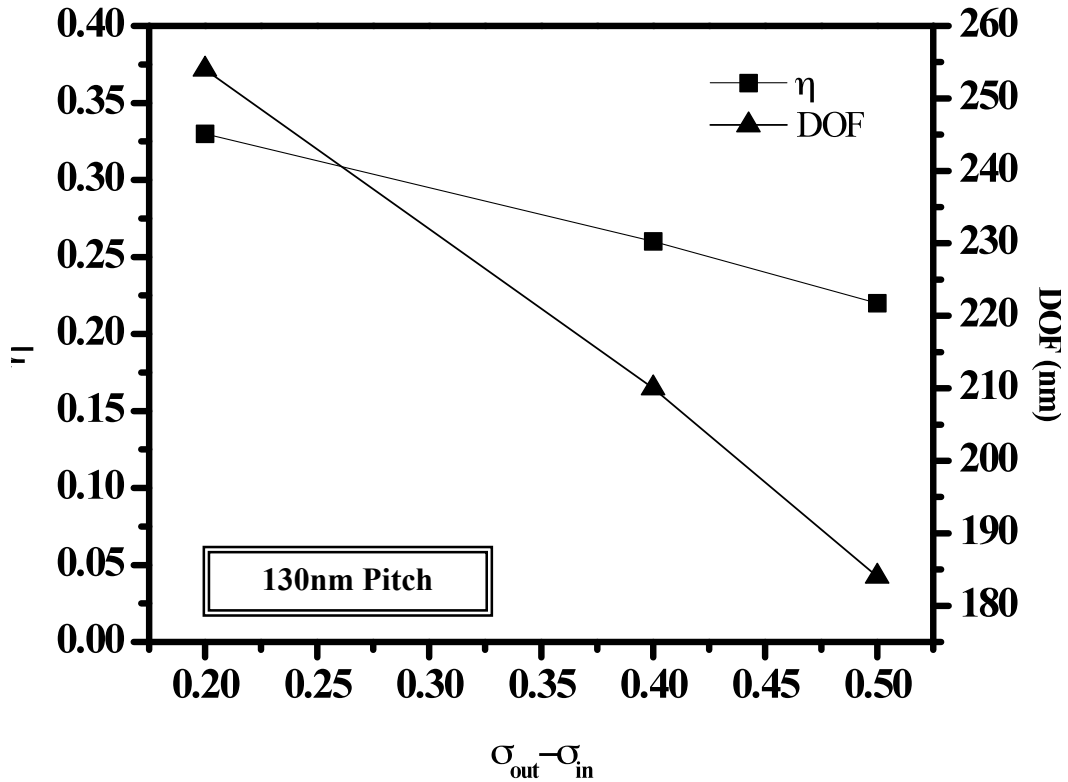


Fig. 5.20 DOF and η for different σ_{in} for 130nm pitch using an annular source shape (NA=1.12, σ_{out} =0.88)

Figure 5.21 shows variations of DOF and η for pitches of 130 nm and 170 nm under various illumination conditions as shown in Table 3.3. In condition 1, the thickness of inner annular is larger than the outer annular. The η and DOF at 130 nm pitch are 184 nm and 0.22 respectively. At 170 nm pitch, η and DOF decrease to 166 nm and 0.19. In condition 2, the thicknesses of inner and outer annular are equal. η and DOF at 130 pitch

are 0.28 and 216 nm respectively. At 170 nm pitch, η and DOF has reduced to 0.15 and 137 nm. In condition 3, the thickness of outer annular is larger than the inner annular. At 130 nm, the η and DOF are 0.3 and 223 nm respectively. The η and DOF values for a 170 nm pitch decreases to 0.21 and 176 nm. Condition 4 is the optimum illumination setting for a 130 nm pitch. The η and DOF values for a 130 nm pitch are 0.3 and 254 nm. At the forbidden pitch of 170 nm, the η and DOF values decrease to 0.15 and 130 nm.

For a 130 nm pitch, the maximum DOF is 254 nm as given by condition 4, which is a single annular. Condition 1 results in a DOF of 184 nm, 28% less than condition 4. The DOF at a 130 nm pitch for condition 2 is 216 nm, 15% less than that of condition 4. For condition 3, the DOF at a 130 nm pitch is 223 nm, around 12% less than that of condition 4. Therefore, condition 3 is preferred for a double annular illumination since it results in the least degradation in the DOF for a 130 nm pitch. For a 170 nm pitch, condition 4 results in a DOF of 130 nm. The DOF for this pitch for condition 1 is 166 nm, a 25% improvement. Condition 2 did not show improvement in the DOF at 170 nm since the resulting DOF is 137 nm. The DOF for a 170 nm pitch has improved by 32% using condition 3. Hence, condition 3 is able to provide the maximum improvement at the forbidden pitch of 170 nm. Using a double annular illumination with illumination setting at condition 3, the DOF at the forbidden pitch has improved by 32% compared with that of a single annular illumination while the DOF at a 130 nm pitch experiences only a 12% degradation.

In the pitch range studied, since the outer annular shows an overlap at the smallest pitch, the outer annular should be placed near the optimum partial coherent value for smaller

itches. The inner annular which improves the image contrast at the forbidden pitch of 170 nm should be placed at its optimum partial coherent value. Its thickness is controlled such that it does not degrade the DOF excessively at small pitches. From the results above, it is seen that condition 3 is desirable since it minimizes degradation in the DOF at the forbidden pitch and results in a minimum loss of DOF at smaller pitches.

The illumination setting for a double annular source depends on the pitch range to be patterned. A thicker outer ring is appropriate for a pattern with dense to medium dense pitch size (< 200 nm). However, if the pitch range is relatively large, a thicker inner ring should be adopted. An overlap factor of 0th and 1st order light can be used as a metric to examine the influence of an additional source point.

It is noteworthy that the proposed method to modify the OAI source is not limited to the current technology node. It can also be extended to smaller technology nodes. For other patterns, such as contact hole and metallization layer, partial coherent settings and OAI source can also be employed to achieve process window enhancement.

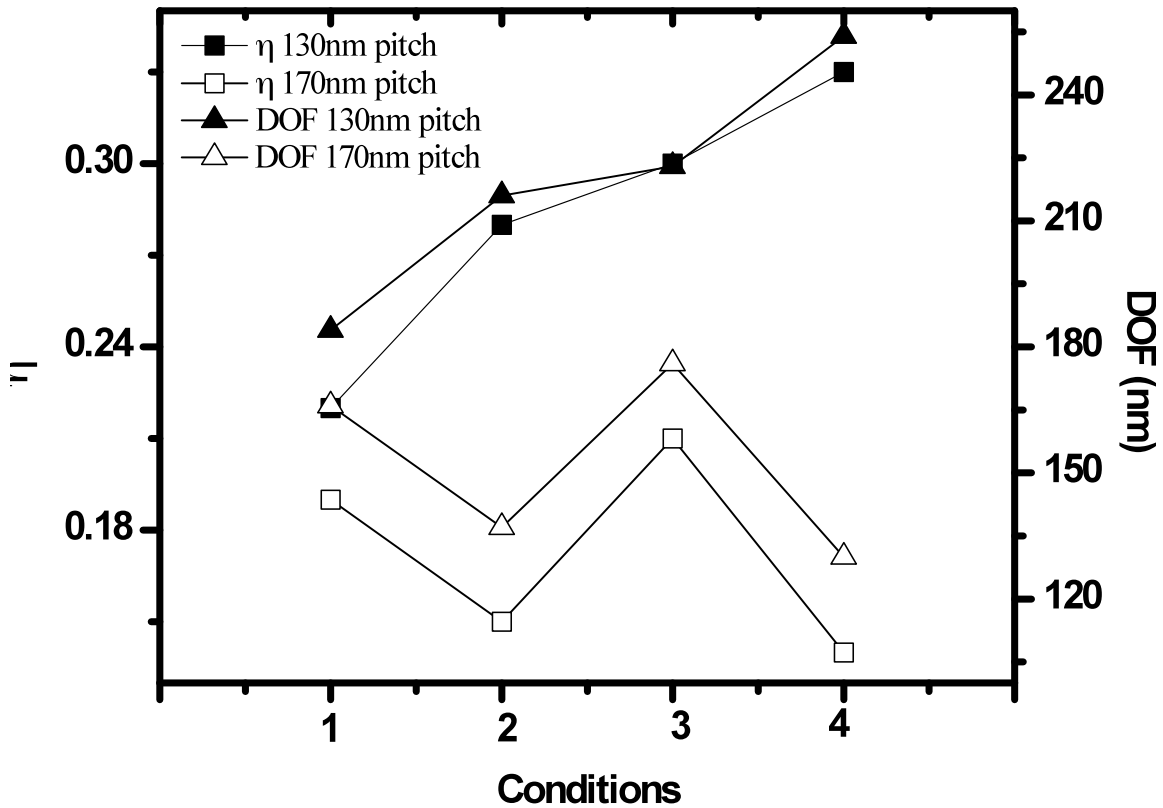


Fig. 5.21 Comparison of DOF and η for a double annular source using Conditions 1, 2 and 3

5.2.3 Extension to other source shapes

Apart from annular source shapes, the proposed concept can be applied to modify other OAI source shapes to achieve enhancement in CD uniformity and process windows robustness. Dipole illumination has the advantage of providing maximum overlapping between 0th and 1st order light and hence it can be implemented for one dimensional line and space pattern with very dense pitch. Figure 5.22 is the CD through pitch performance comparison between an optimized dipole and the proposed double dipole source shapes. Despite the improvement in CD uniformity, conventional dipole illumination still exhibits forbidden pitch phenomenon. Fluctuation of CD is observed between 150 nm

and 200 nm pitch. The maximum CD error is around 4 % and the CD fluctuation range is close to 10 % of nominal CD (45 nm). By implementing double dipole illumination, the maximum CD error has reduced to around 2 % and CD fluctuation range has also lowered to 4 %.

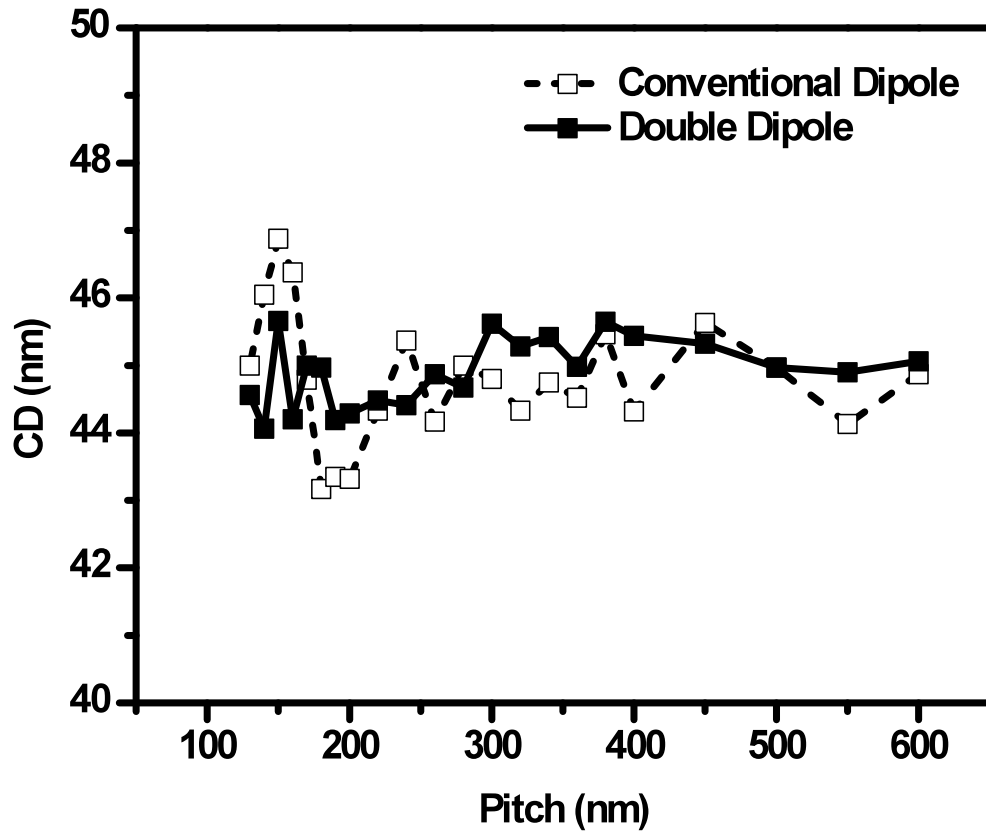


Fig. 5.22 CD through pitch performance comparison between conventional dipole and double dipole illuminations

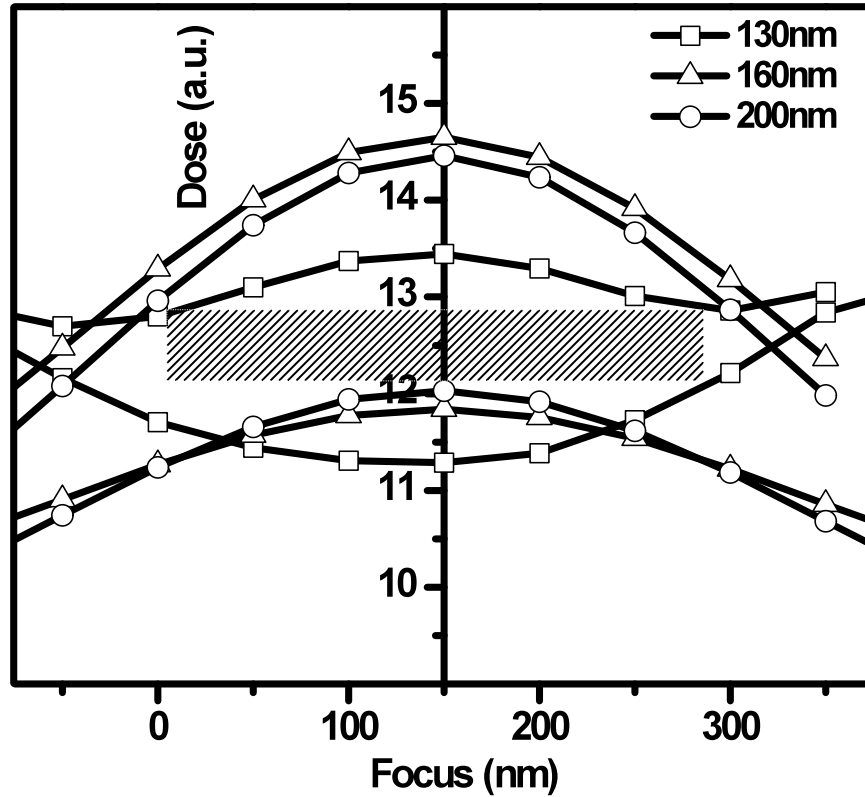


Fig. 5.23 Common process window between 130 nm, 160 nm and 200 nm pitch

From Fig. 5.22, the forbidden pitch range for conventional dipole is between 150 nm to 200 nm where the largest CD fluctuation is seen. By employing double dipole source shape, the CD fluctuation due to forbidden pitch effect is minimized. The common process window between 130 nm, 160 nm and 200 nm pitch is shown in Fig. 5.23. Common DOF at 5 % exposure latitude is around 280 nm. Therefore, there is no significant reduction of DOF near the forbidden pitch range when double dipole illumination is used. Hence, from the simulated CD through pitch and common DOF, the proposed idea can also be applied to dipole illumination to improve through pitch imaging performance.

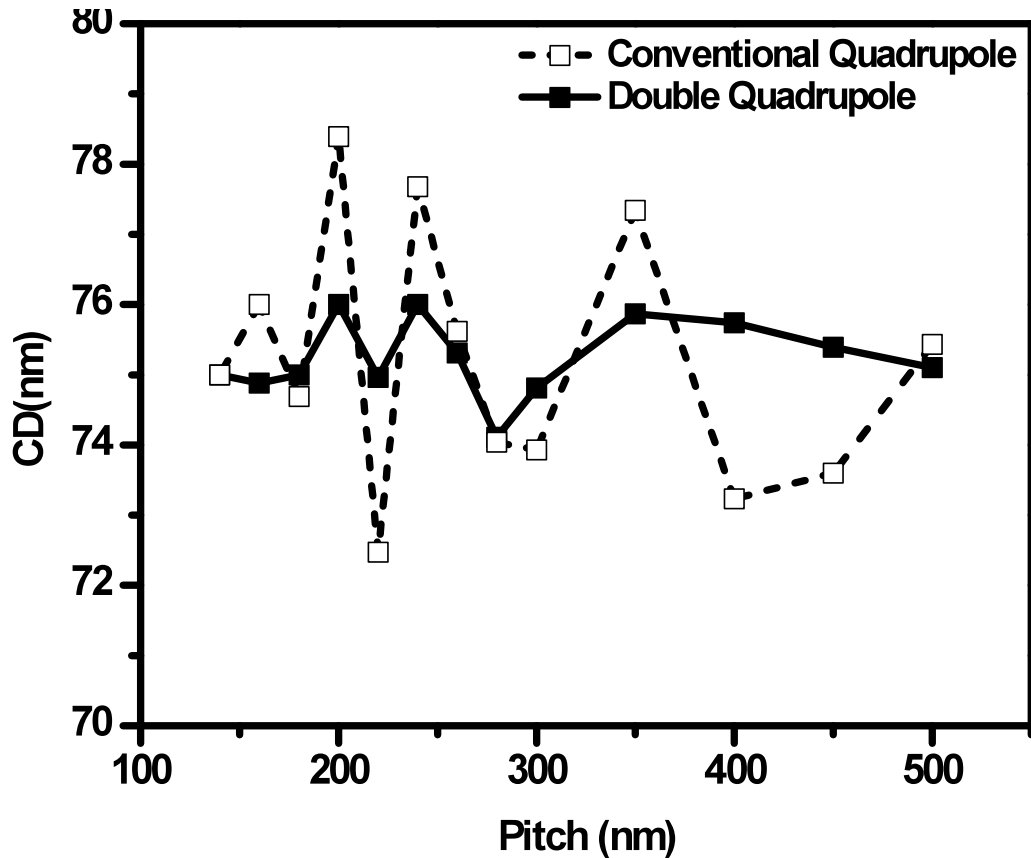


Fig. 5.24 Comparison between CD through pitch performance for conventional quadrupole and double quadrupole illuminations

Apart from line and space pattern, the feasibility of applying the proposed concept on contact holes array patterning is studied. The CD through pitch performance comparison between conventional quadrupole illumination and double quadrupole illumination is shown in Fig. 5.24. For conventional quadrupole illumination, the maximum CD error is 4 % at 200 nm pitch and the CD fluctuation range is around 8 % of nominal CD (75 nm). Improvement is observed as double quadrupole is applied. The maximum CD error is reduced to around 1 % and CD fluctuation range is lowered to 2.6 %.

The common process window for contact array with 130, 160 and 200nm pitch using is shown in Fig. 5.25. From Fig. 5.24, it is seen that the forbidden pitch is at 200 nm to 220

nm. By implementing double quadrupole illumination, common DOF at 5 % EL is around 180 nm. Thus, the effect of forbidden pitch is minimized. Compared to OAI source shape optimized using SMO, the proposed source shape has more general applications since it offers flexibility to change the partial coherent settings whereas source shape from SMO is pattern specific.

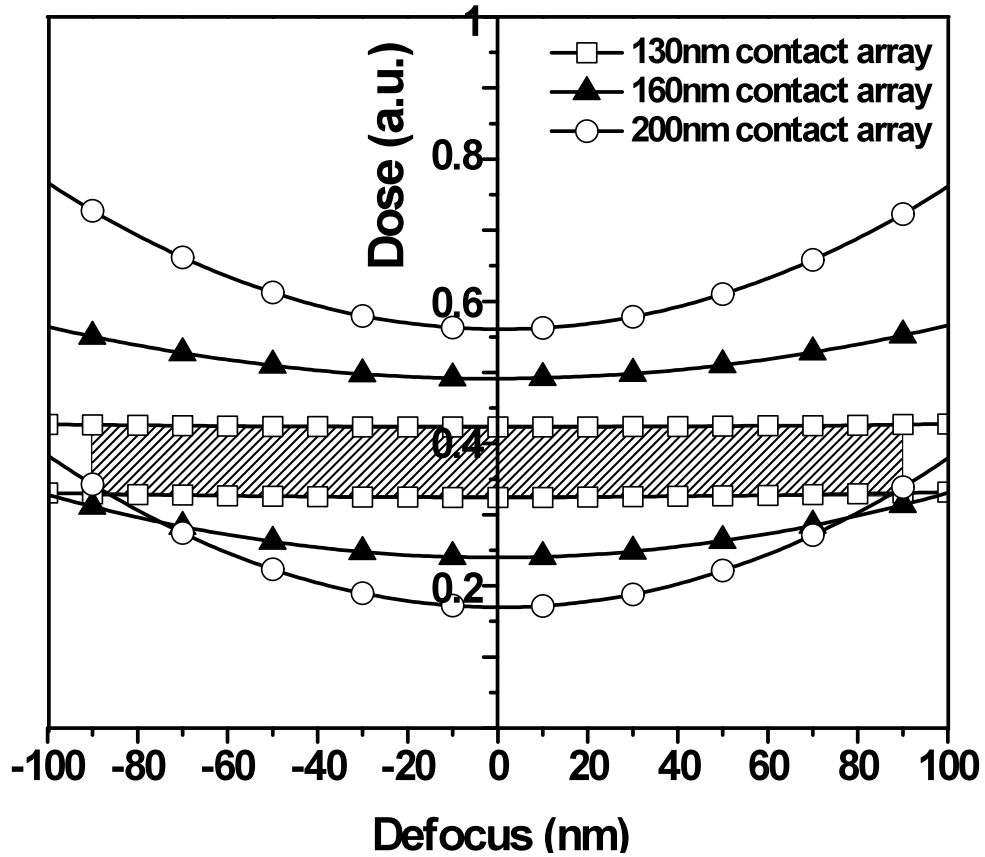


Fig. 5.25 Common process window (hatched area) for 130, 160 and 200nm pitch contact hole array

The simulation results shown in Fig. 5.25 has proven the capability of the proposed modification to mitigate the effect of forbidden pitch. In the study, a double dipole and quadrupole configurations are used. Similar to an annular illumination, there can be multiple poles depending on the pitch range to be patterned. The thickness of each pole

needs not be equal. Adjustment in the thickness can be done according to the pattern density to allow maximum benefit from this modification.

5.2.4 Optical proximity correction for modified OAI

5.2.4.1 Line end shortening on end to end structures

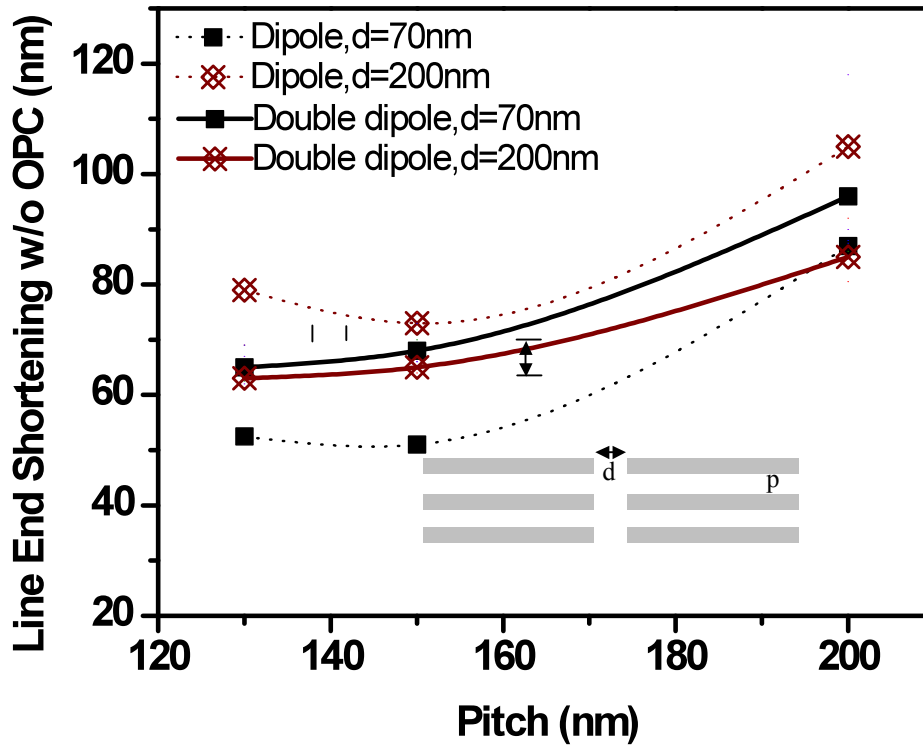


Fig. 5.26 Line end shortening for an end to end structure

The effectiveness of the proposed source on improving through pitch CD uniformity and process window at the forbidden pitch has been demonstrated. Apart from the CD and DOF consideration, the requirement for OPC is also examined. It is crucial that the proposed modification does not cause an increase in the size of the OPC features and violate the mask design rules. Line end shortening characteristics without OPC (no biasing and no hammerhead) for conventional dipole and double dipole OAI source

shapes are shown in Fig. 5.26. It can be observed from the plot that line end shortening for conventional dipole and double dipole sources have similar characteristics. Besides, both illuminations have similar amount of line end shortening. Patterns with larger pitch and line end separation suffer more line end shortening relatively as compared to patterns with smaller pitch and line end separation. This is because patterns with larger pitch and line end separation are relatively isolated compared to the dense patterns. Since illumination partial coherence settings and exposure dose are optimized to the smallest pitch, image quality will be poorer for larger pitch and line end shortening becomes more severe.

Conventional dipole illumination (dotted line) shows variation in line end shortening for different pitch and line end separations. The smallest line end shortening occurs at 130 nm pitch with a 70 nm line end separation, the amount of shortening is 53 nm. For the same amount of line end separation, line end shortening is 87 nm at 200 nm pitch. This indicates a 34 nm increase in line end shortening as pitch increases from 130 nm to 200 nm, which is equivalent to a 64 % increase. From simple line and space simulation, it is observed that the forbidden pitch is at 200 nm. Thus, it is expected that line end shortening is more severe at 200 nm due to poorer image contrast. In fact, line end shortening is most severe for 200 nm line end separation, the largest line end separation used in this study. At 130 nm pitch, line end shortening is 79 nm. The line end shortening increases to 105 nm at 200 nm pitch under this line end condition. This corresponds to an increase of 26 nm or 33 % with respect to 130 nm pitch. Consider constant pitch value, at 130nm pitch, the line end shortening has increased from 53 nm to 79 nm when the line end separation increases from 70 nm to 200 nm. This corresponds to a 49 % increase.

Meanwhile, line end shortening at 200 nm pitch increases from 87 nm to 105 nm when line end separation increases from 70 nm to 200 nm, which corresponds to a 21 % increase. Among the two factors considered in the simulation, i.e. line end separation and pitch, it can be observed from the results that the pitch has a more significant influence on line end shortening for an end to end structure.

Double dipole illumination (solid line) shows a similar trend with that of conventional dipole illumination. The smallest line end shortening occurs at 130 nm pitch at a 70 nm line end separation, with a 65 nm shortening observed. For similar line end separation, the line end shortening increases by 49 % to 96 nm at 200 nm pitch. For a 200 nm line end separation, the line end shortening is around 65 nm at 130 nm pitch and the shortening increases to 85 nm at 200 nm pitch, an increase of 30 %. Consider a constant pitch value at 130 nm, the line end shortening is relatively constant, it fluctuates less than 10% for different line end separations. Similarly, at 200 nm pitch, the range of fluctuation is also less than 10 % for line end separation between 70 nm and 200 nm. The results has also shown that the pitch has a stronger influence on line end shortening.

From the simulated results, double dipole illumination shows similar line end shortening compared with conventional dipole illumination. However, at the smallest pitch, line end shortening for double dipole illumination is larger than that of conventional dipole. The line end shortening is 53 nm for a conventional dipole illumination and 65 nm for a double dipole illumination, this represents a 22 % increase. The addition of a second dipole has degraded the image quality at a 130 nm pitch and results in a slight increase in the line end shortening. At a 200 nm pitch, the double dipole shows a smaller variation for different line end separation as compared to the conventional dipole. However, a

second dipole improves the image quality at 200 nm pitch and the line end shortening becomes relatively stable. Therefore, it is seen that a double dipole illumination has similar line end shortening characteristics with a conventional dipole illumination. However, a double dipole illumination provides a better control over the conventional dipole in terms of linewidth CD and DOF. The implementation of a double dipole illumination is feasible in this case since it does not induce additional line end shortening and is capable of maintaining stable CD and DOF performance.

The OPC hammerhead feature size for line end pattern with 130 nm and 200 nm pitch is shown in Fig. 5.27. As the line end separation increases, the width of the hammerhead required increases. Furthermore, as the pitch increases, the width of the hammerhead that is required also increases. It is also seen that the width of the hammerhead required for both conventional and double dipole sources are similar. Thus, the proposed modifications to the OAI does not result in an increase in the OPC feature size needed for mask manufacturing.

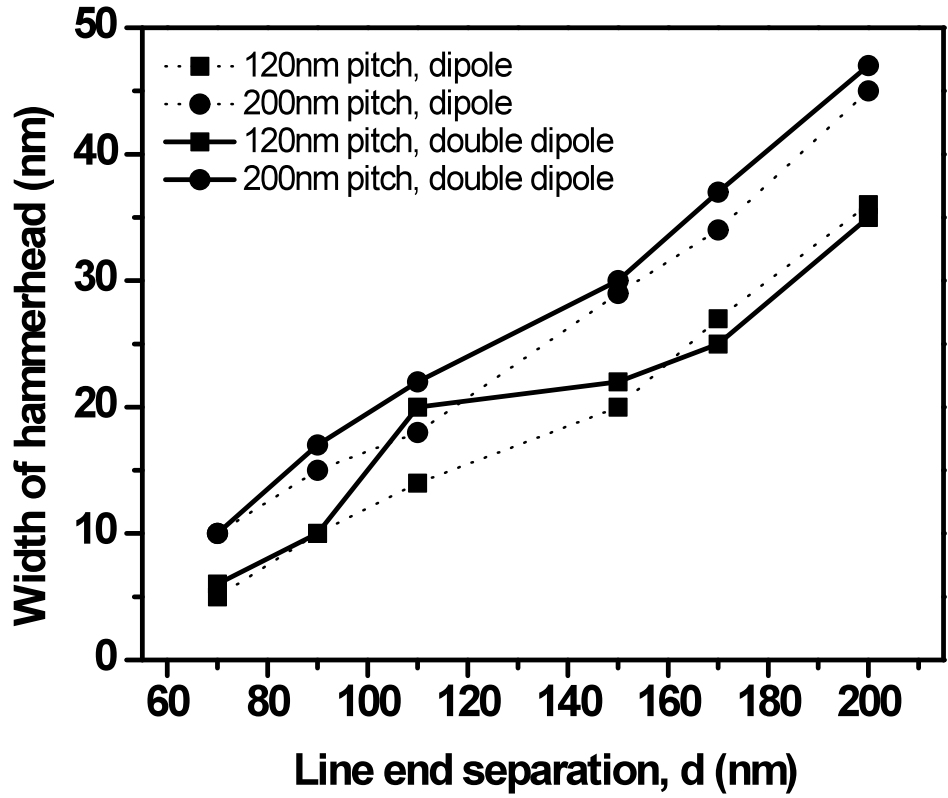


Fig.5.27 OPC feature size comparison between dipole and double dipole illumination for an end to end structure

5.2.4.2 Line end shortening for staggered structure

Figure 5.28 shows the line end shortening without OPC (no biasing and no hammerhead) for a staggered structure with different pitch and line end separations. In general, the line end shortening is more serious for a pattern with a larger pitch and line end separation. Since similar partial coherent settings are used for the staggered structure, a similar shortening trend is observed. Within the pitch range studied, the line end shortening is most severe at a 200 nm pitch.

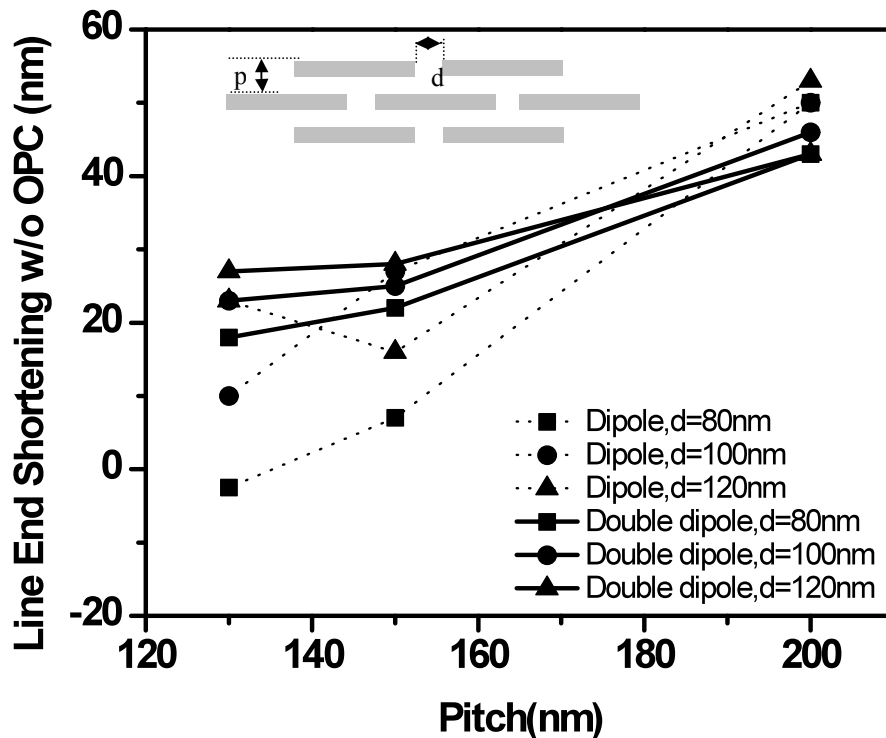


Fig. 5.28 Line end shortening for a staggered structure

For the conventional dipole illumination, it is noted that line end shortening is -2.5 nm at 130 nm pitch with 80 nm line end separation. The negative value of shortening indicates that instead of line end shortening, the separation between line ends is narrower than it is initially desired. Since the illumination settings are optimized to the smallest pitch, the

line end performance is expected to be better due to better image quality. For other pitches above 130 nm, the line end shortening is 7 nm for a 150 nm pitch and the shortening increases to 50 nm for a 200 nm pitch. The line end shortening increases significantly at the forbidden pitch of 200 nm due to its poor image contrast. As the line end separation increases, line end shortening becomes more severe. The largest line end shortening is observed for a line end separation of 120 nm. The image experiences a line end shortening of 23 nm at a 130 nm pitch. However, at a pitch of 200 nm, line end shortening increases to 53 nm. It can also be seen that for a pitch of 130 nm, the line end shortening increases from -2.5 nm to 23 nm as line end separation increases from 80 nm to 120 nm. At a 200 nm pitch, the line end shortening increases from 50 nm to 53 nm as the line end separation increases from 80 nm to 120 nm. Among the two factors considered, the results indicated that the pitch has a more significant influence on the line end shortening than that of the line end separation. This observation also agrees with that of the previous section.

The double dipole illumination also experiences similar line end shortening as the conventional dipole. For a line end separation of 80 nm, the line end shortening is 18 nm at 130 nm pitch. For the same line end separation, line end shortening increases to 43 nm at a pitch of 200 nm. The line end shortening increases with line end separation. At 120 nm line end separation, the line end shortening at a 130 nm pitch is 27 nm. The shortening increases to 43 nm at a 200 nm pitch. From the results, it can be observed that at 200 nm pitch, the line end shortening remains relatively constant for different line end separations. In general, pattern with larger pitch and line end separation suffers more line

end shortening. Similar to the conventional dipole illumination, the pattern pitch has a higher influence on the line end shortening than the line end separation.

The results of line end shortening for a staggered structure has shown that both conventional and double dipole illuminations experience similar amount of line end shortening. At a 130 nm pitch, the line end shortening is larger for a double dipole illumination. The additional dipole has resulted in the degradation of image contrast at the line end and hence results in a larger line end shortening. However, the line end shortening is maintained at about the same level for the 150 nm and 200 nm pitch. It is also noted that the range of variation for the double dipole illumination is smaller for different line end distances. This is attributed to the uniform through pitch performance of the double dipole illumination.

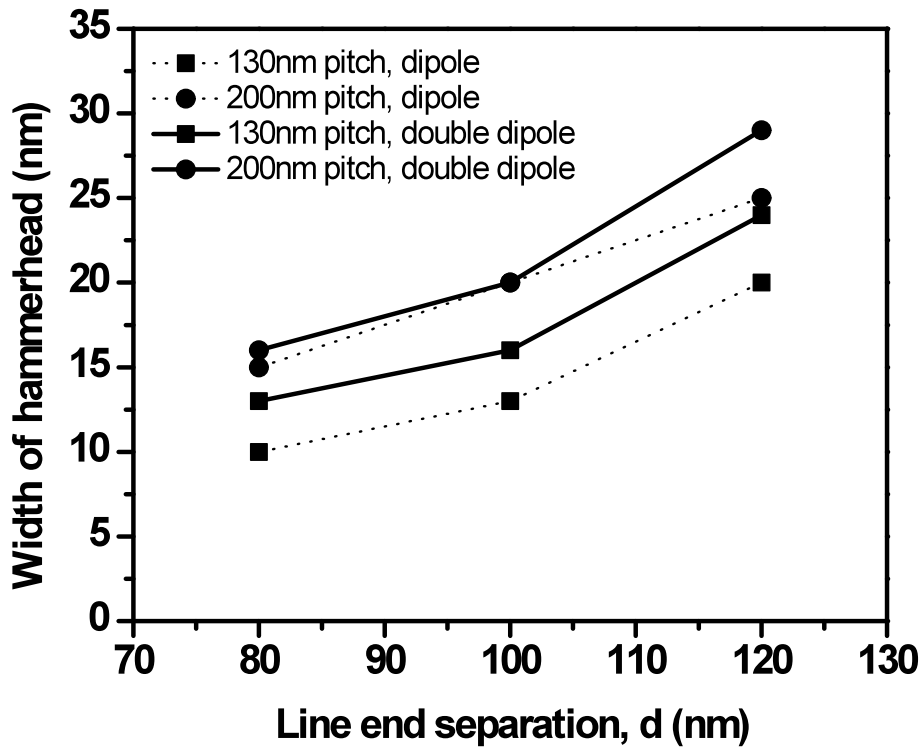


Fig. 5.29 OPC feature size comparison between dipole and double dipole illumination for a staggered structure

Figure 5.29 shows a hammerhead feature size required to correct line end shortening for a staggered pattern with pitches of 130 nm and 200 nm. It is seen that the feature size required increases with both the pitch and line end separation. Similarly, the size of the OPC feature does not increase significantly for the double dipole source. Hence, from the study on the two types of line end conditions shown above, it is observed that modifications on the OAI will not result in a significant change in the OPC feature size and violation of the mask design rules.

5.3 Resolution enhancement for contact hole patterning

5.3.1 CD and DOF performance comparison

Circular printed target with circular apertures on a mask is discussed in the following section. The patterning of a regular contact hole array with different pitches as shown in Fig. 5.30 is studied. Imaging performance such as CD through pitch and DOF through pitch are compared with results obtained by the conventional square aperture approach.

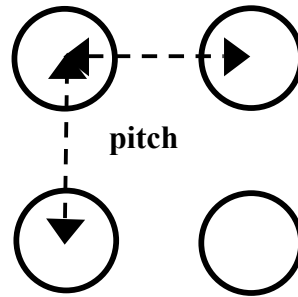


Fig. 5.30 Illustration of a regular contact hole array

The simulated CD through pitch results are shown in Fig. 5.31. Dimensional biasing on a mask is applied to both square and circular apertures to fulfill the target of a 80 nm CD and attain a common process window between dense and isolated patterns. For a mask with square apertures, dimensional biasing is achieved by varying the length of the opening. While for circular apertures, dimensional biasing is carried out by varying the diameter of the opening. From Fig. 5.31, it can be observed that both types of aperture experience a certain amount of CD fluctuation. This is due to the intrinsic difference in the diffraction order of different pitches. It can be seen that for a square aperture, the maximum CD error of 5.6 % occurs at a 170 nm pitch. The CD fluctuates in a range of 9 % for the square apertures while the circular apertures fluctuates in the range of 3.75 % and the maximum CD error is around 2 % at 190 nm pitch. Thus, by adopting the proposed circular apertures on mask, the maximum CD error is reduced by 64 % while

the CD fluctuation is reduced by 58 %. The average CD error is also reduced from 2.5 % to 0.6 % through implementation the proposed method. Hence from the simulated CD through pitch performance, it is demonstrated that a better CD control can be achieved by the implementation of a circular aperture. The improvement is attributed to the enhancement of the aerial image contrast resulted from the proposed method. Due to the diffraction characteristics of a circular aperture array as shown in Eq. (3.35), a higher magnitude first order diffraction is achieved which enhances the robustness of the aerial image.

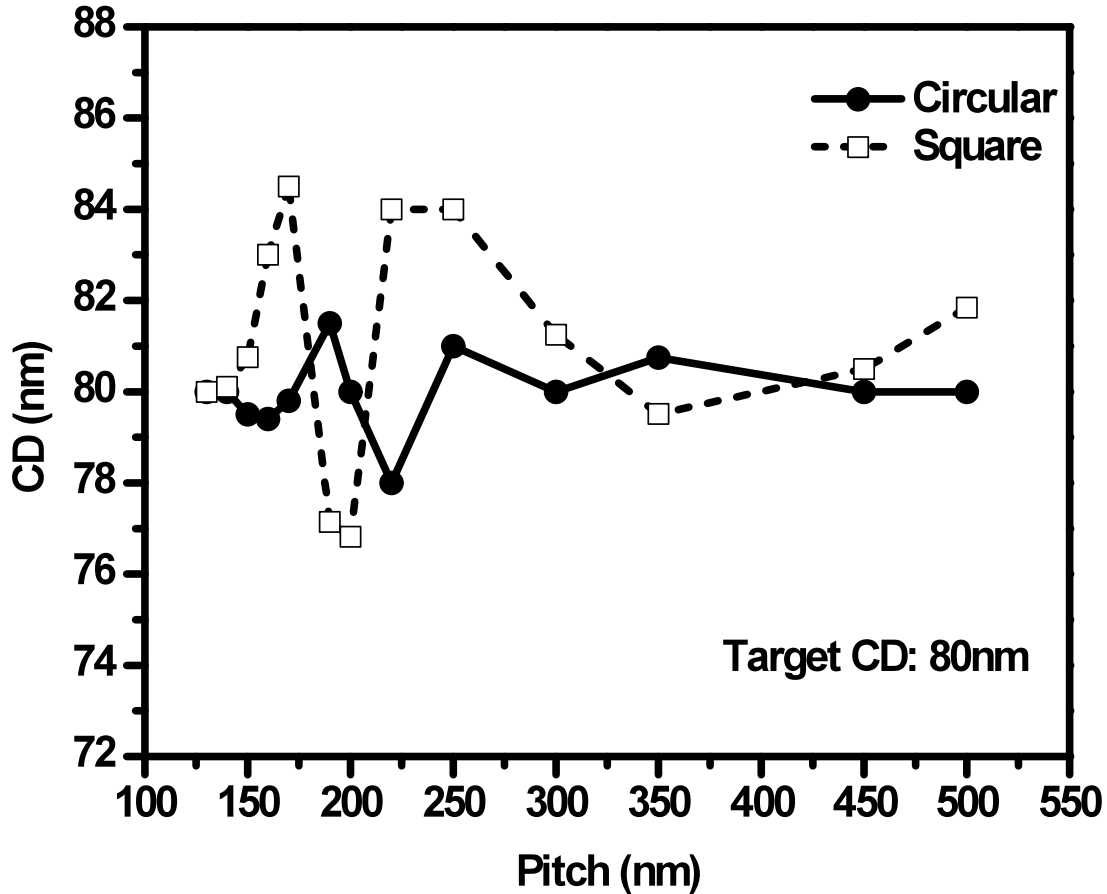


Fig. 5.31 CD through pitch performance comparison between a mask with circular and square apertures

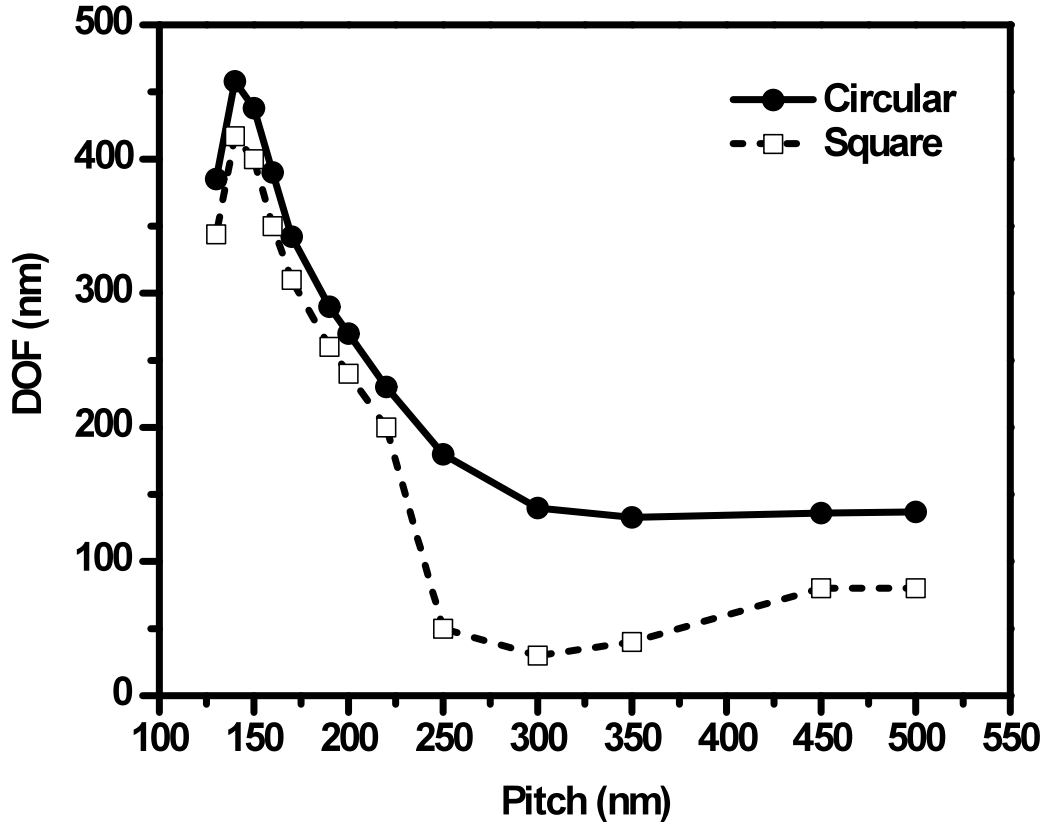
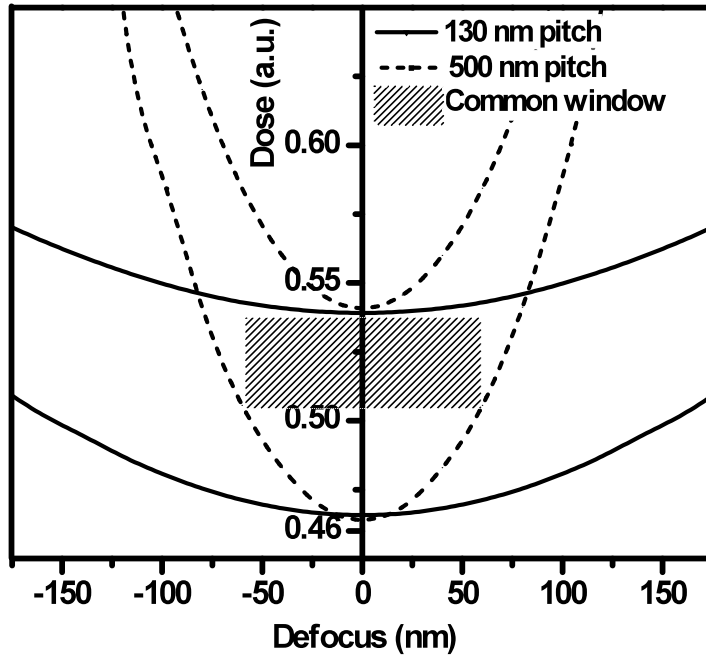


Fig. 5.32 DOF through pitch comparison between a mask with circular and square apertures

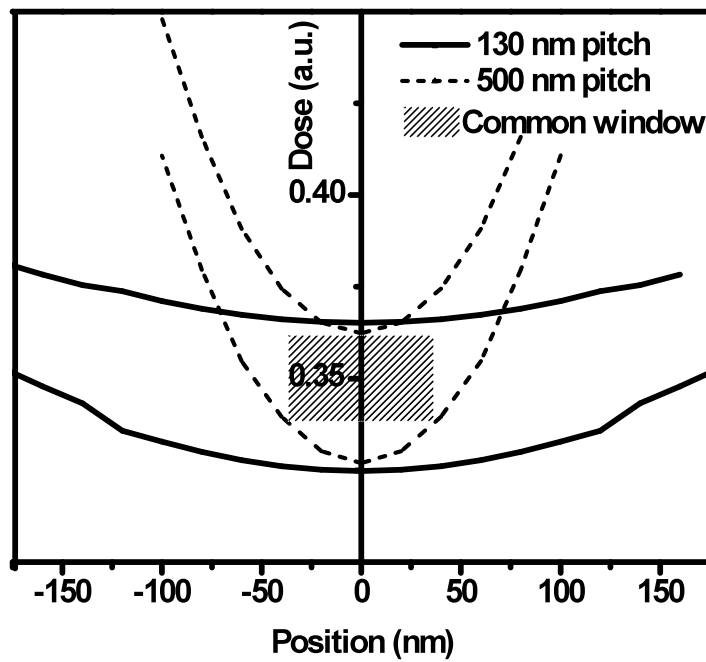
The simulated DOF through pitch at 5 % exposure latitude obtained for both the square and circular apertures is shown in Fig. 5.32. For both types of aperture, it is seen that the DOF is the largest at 140 nm pitch and it degrades for larger pitch since the illumination settings are optimized for the smallest pitch. For the larger pitch, the aerial image contrast is poorer and hence results in a degradation of the process window. The results shows that a square aperture has the largest DOF of 417 nm at 140 nm pitch but the DOF decreases to below 100 nm at 250 nm pitch and remains at that level for larger pitches. For a circular aperture, the largest DOF is 460 nm at 140 nm pitch and it decreases to around 140 nm at 500 nm pitch. Therefore, it can be observed that the application of a circular aperture would result in an improvement of the process window through pitch.

The largest gain occurs at the pitch range of 250 nm to 350 nm. The circular aperture mask shows an improvement for DOF of more than 100 % compared to a square aperture mask. The average increase in the DOF is around 11 % from 130 nm to 200 nm. In addition, a circular aperture can achieve a DOF of above 100 nm for a pitch size of up to 500 nm with a simple dimensional biasing. An improvement in DOF indicates that by adopting a circular aperture, the aerial image contrast is enhanced. Thus, the process window obtained is more robust and reliable.

The common process window for a 130 nm and 500 nm pitch contact hole array is shown in Fig. 5.33. The graphs comprise of the upper and lower CD limits for each of the pitches shown and the region within the CD limits indicates the process window for the pattern to be printed to within $\pm 10\%$ of the targeted CD. A rectangular process window which is also known as process latitude can be defined for a range of dose fluctuation. In this study, a 5 % dose fluctuation is used as the criterion for the process windows. The overlapping area between the two sets of CD limits is the common process window for both pitches. It can be seen that the process window for the 130 nm pitch is the largest as the illumination settings are optimized to provide the largest process window for this pitch. For a square aperture, the common process window is around 100 nm at a 5 % exposure latitude. The common process window for a circular aperture has improved by 30 % to 130 nm at a 5 % exposure latitude. Hence, a significant gain in the common process window can be achieved by a applying circular aperture on the mask for contact hole patterning.



(a)



(b)

Fig. 5.33 Common process windows for a contact hole array of 130 nm and 500 nm pitch (a)circular aperture, (b)square aperture

5.3.2 Comparison of NILS, MEEF and aerial image

The impact of implementing a circular aperture on the aerial image contrast can be further examined by studying the aerial image properties. Normalized image log slope (NILS) is first studied to determine the effect of a circular aperture on the aerial image robustness. The simulated NILS for pitches of 130 nm to 500 nm is shown in Fig. 5.34. In general, the NILS is higher at smaller pitches and its values reduce as the pitch increases since illumination conditions are optimized to provide optimum image contrast at smaller pitches. For a square aperture mask, the NILS at 130 nm pitch is around 1.75. For subsequent pitches the NILS improves and reaches maximum at 160 nm pitch. As the pitch increase to 250 nm, NILS decreases to a minimum of 0.68. For a circular aperture mask, the NILS at 130 nm pitch is around 2.2. Similarly, the NILS improves with the pitch and reaches a maximum at 160 nm pitch. However, it decreases to around 1.3 at 250 nm pitch. From the results, it is seen that for a circular aperture the NILS improves by around 20% from 130 nm to 160 nm pitches. For other pitches, the average improvement is around 15 %. At a pitch of 250 nm pitch, the NILS for a circular aperture is close to 2 times more than that of a square aperture. From the observations, it is seen that the aerial image quality is improved by the proposed modifications on the mask. The improvement of around 20 % at a smaller pitch range suggests that masks with circular apertures show significant aerial image contrast enhancement. Furthermore, a more uniform through pitch performance can be achieved by the implementation of the proposed method. The improvement in the aerial image NILS has also resulted in an increases in the process window as observed previously (Section 5.3.1).

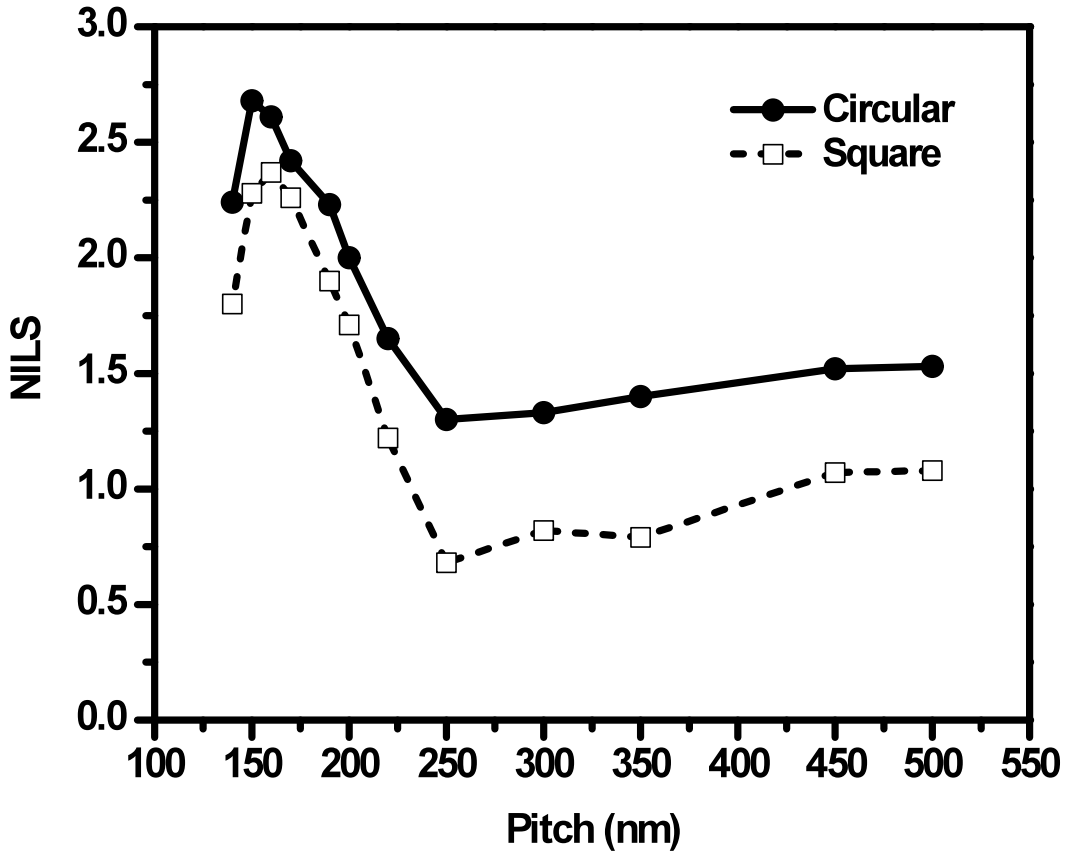


Fig. 5.34 NILS through pitch comparison between mask with circular and square apertures ($NILS = CD \frac{d \ln I_x}{dx}$)

Critical dimension error on mask feature is one of the most significant causes of CD errors on a wafer. As the feature dimension and pitch reduces, mask CD errors does not correlate linearly with CD error on a wafer. Mask error enhancement factor (MEEF) measures the ratio of wafer CD error to mask CD error and a larger MEEF indicates a higher process sensitivity to the mask CD variation. A comparison of MEEF between mask with a circular and a square aperture is shown in Fig. 5.35. In general, the MEEF is larger at a smaller pitch and decreases for a larger pitch. This is because at a smaller pitch, the imaging condition is closer to the resolution limit of the lithography system. The diffraction orders recorded are limited to the 0th and part of the 1st order light, and hence

there is a loss in the high spatial frequencies components resulting in enhanced the pattern edges. For a circular aperture, the MEEF (largest) at 130 nm pitch is 5.14 and as the pitch increases to 500 nm, the MEEF reduces to 1.5. The MEEF for a square aperture at 130 nm pitch is 5.67, and as the pitch increases to 500 nm, the MEEF reduces to 1.85. Hence with a circular aperture, the MEEF is reduced by 10 % at a 130 nm pitch, and by 20 % at a 500 nm pitch. The average improvement in the through pitch is around 15 %. A mask with a circular aperture is capable of achieving a lower MEEF due to the relatively smaller change in mask area. In addition, the improvement in the MEEF is also attributed to an improvement in the aerial image contrast resulted from the implementation of a circular aperture. Due to the diffraction property of a circular array, a higher amplitude of the 1st order light which enhances the aerial image contrast can be recorded. A process with lower MEEF is favourable because it prevents a loss of the process margin due to the CD errors resulting from the mask errors.

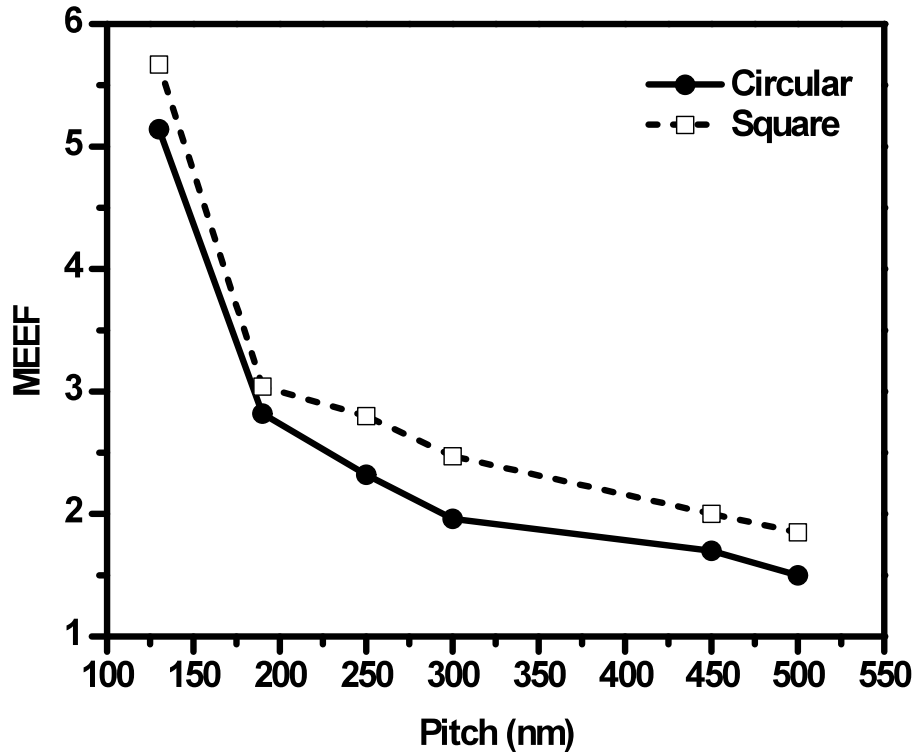
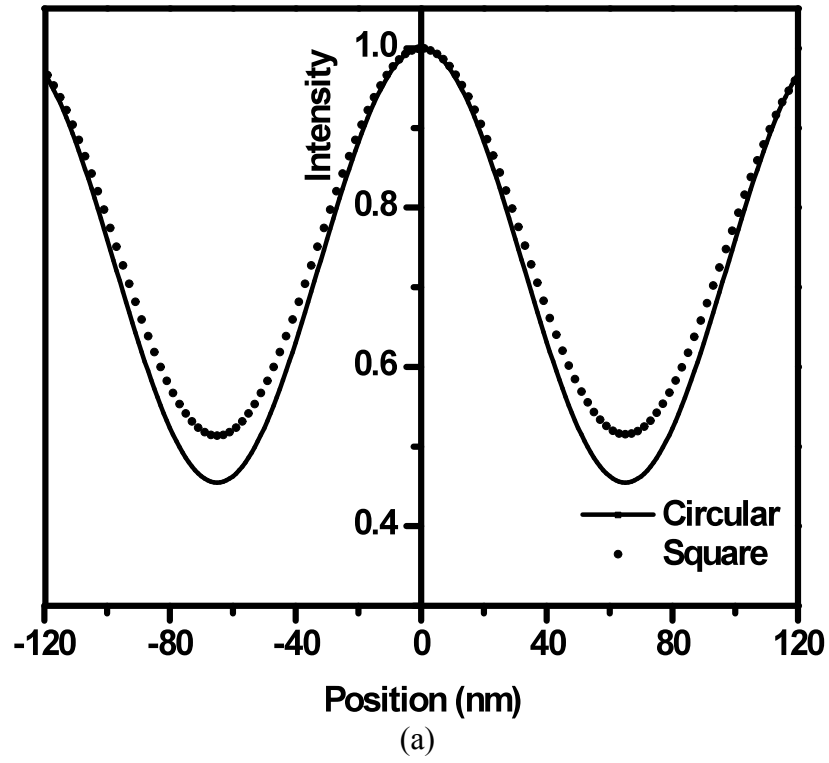
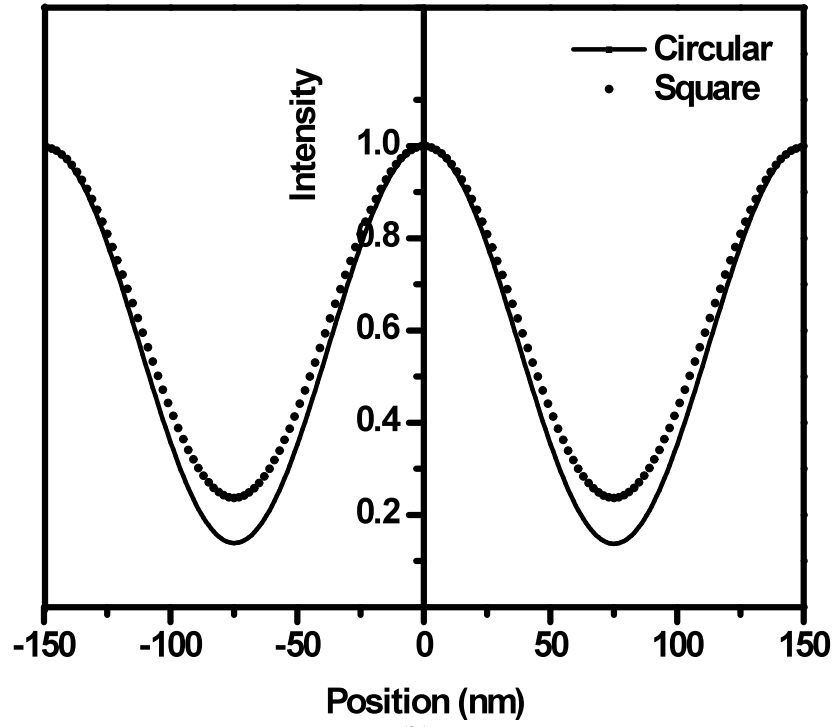


Fig. 5.35 MEEF through pitch comparison between a mask with circular and square apertures

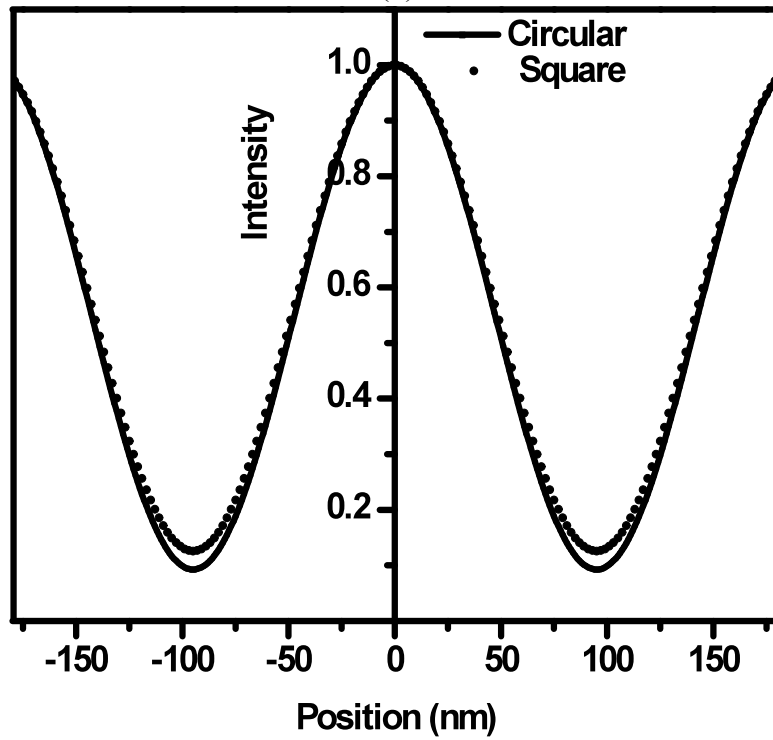
The influence of a circular aperture on the aerial image formation is examined by studying the aerial image intensity. The aerial image intensity for a contact hole formed by both types of apertures with 130 nm, 150 nm, and 190 nm pitch is shown in Fig. 5.36. The aerial image intensity is normalized with the maximum intensity of each case for comparison purposes. For a square aperture, the image contrast at a pitch of 130 nm is 0.32. For larger pitches, the difference between the maximum and minimum aerial image intensity increases. At a pitch of 190 nm, the aerial image contrast improves to 0.79. For a circular aperture, the image contrast at a pitch of 130 nm is 0.38. Similarly, the image contrast at 190 nm pitch increases to 0.84. Thus, it can be seen that better aerial image contrast can be achieved by implementing a circular aperture on a mask. The average improvement is more than 10 % across the pitch range studied. The enhancement in the

aerial image contrast has resulted in a significant gain in the process window as mentioned in previous discussions. The improvement in the aerial image contrast is attributed to the higher amplitude of the 1st order diffraction recorded during image reconstruction.





(b)



(c)

Fig. 5.36 Aerial image intensity plot for a contact hole array with pitches of (a) 130 nm , (b) 150 nm , and (c) 190 nm

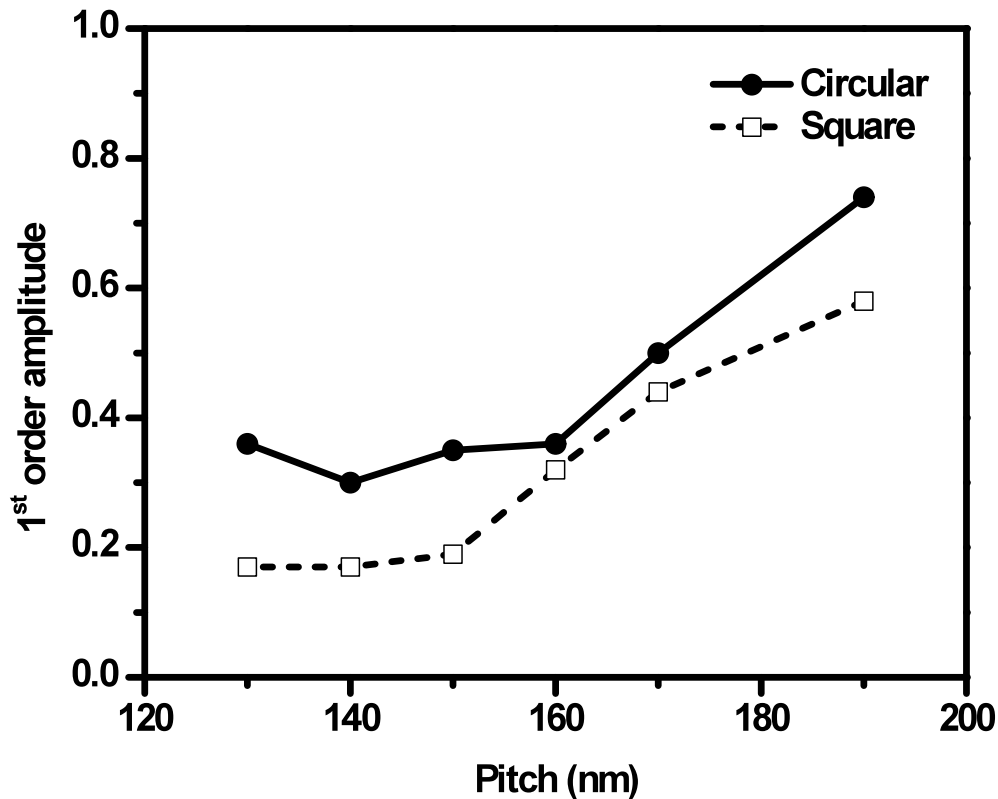


Fig. 5.37 A comparison of 1st order diffraction amplitude for a mask with circular and square apertures

The aerial image quality of a contact hole array depends on the diffracted light collected at the projection pupil plane. Therefore, the effect of a circular aperture on a mask can be examined by studying the diffracted light. Figure 5.37 shows the the 1st order amplitude for a circular contact hole array with different pitches. In general, the 1st order amplitude increases steadily as the pitch increases. This is because the diffraction order distribution is closer to the 0th order for larger pitches. It is seen that the increase in the 1st order magnitude is not linear due to different biasing. Since the intensity envelope follows either a Bessel or a *sinc* function which contains a central peak, the closer a diffraction order is to the center, the larger the magnitude of the 1st order. For a square aperture, the 1st order amplitude at a pitch of 130 nm is 0.17 which increases to 0.58 at a pitch of 190

nm. For a circular aperture, the 1st order amplitude at a pitch of 130 nm is 0.36 which increases to 0.74 at a pitch of 190 nm. The improvement in the image contrast and NILS is attributed to the increase in the 1st order amplitude collected at the pupil plane which results in a better aerial image quality during image reconstruction, as given by Eq. (3.37). Due to the difference in the envelope that defines the magnitude of the diffraction orders, improvement in the diffraction order magnitude can be achieved by a circular aperture on the mask.

5.3.3 Enhancement for staggered contact holes pattern

Apart from a regular contact hole array, designs that are similar to a staggered contact hole pattern are also commonly encountered. A staggered contact hole pattern is shown in Fig. 5.38. It consists of contact holes that are separated by a distance d in both the horizontal and vertical directions. The challenge in a staggered contact hole pattern is the non regular separation between neighboring features, and the separation is along a 45° orientation is $\sqrt{2}d$. A radial segmentation approach is employed to enhance the image contrast for a mask with circular apertures. For a mask with square apertures, the insertion serifs at the corners is adopted. Optimized illumination conditions for a pattern with the smallest spacing d are applied. The optimized conditions are similar the same for both type of apertures.

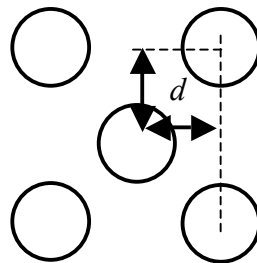


Fig. 5.38 Illustration of a staggered contact holes pattern

The DOF at a 5 % exposure latitude for a staggered contact holes with different staggered spacing d resulted from a circular and square aperture is shown in Fig. 5.39. It is seen that the DOF at the smallest spacing d of 100 nm is the largest since illumination conditions are optimized to produce a maximum process window at this spacing. For subsequent spacing, the DOF reduces gradually. In general, the characteristic of the DOF variation are similar for both the square and circular apertures. The largest DOF for a staggered contact hole pattern with circular apertures is around 160 nm at a spacing d of 100 nm. The smallest DOF at a spacing d of 200 nm is about 28 % less than that of 100 nm spacing. For a conventional square aperture, the largest DOF at a spacing of 100 nm is 130 nm. Similarly, the DOF reduces as the spacing increases. The smallest DOF at a spacing of 200 nm is around 22 % less than that at the optimum spacing. From the results it is seen that an average improvement in the DOF performance of around 10 % is achieved by incorporating circular apertures with radial segmentation. This indicates that the circular apertures with radial segmentation is also effective in improving the imaging performance of random contact hole pattern as well.

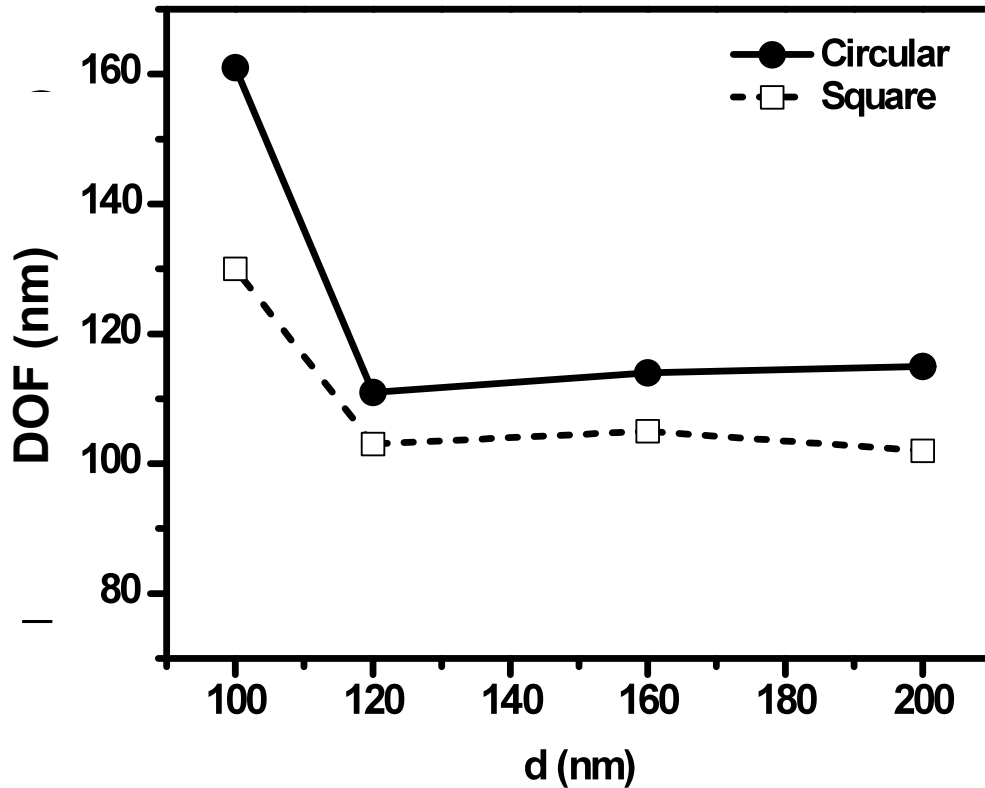


Fig. 5.39 Comparison of DOF between mask with circular and square aperture for a staggered contact hole pattern with spacing d

A NILS comparison for different spacing d is shown in Fig. 5.40. It can be observed that the NILS variation is similar for both the square and circular aperture. At the smallest spacing, the NILS achieved for a circular aperture is 1.94 and increases to a maximum value at a spacing of 160 nm (a 10 % increase). For a square aperture, the NILS at the smallest spacing is around 1.56 and increase to a maximum value at 160 nm spacing (a 25 % increases). From Fig. 5.40, it is seen that a staggered contact holes pattern with circular apertures have a higher NILS. On the average, the improvement is around 10 % for different spacings. Therefore, it is seen that the aerial image contrast has been enhanced by circular apertures with radial segmentation. The process window enhancement observed can thus be attributed to the gain in NILS. It is also seen from Fig.

5.40 that the NILS decrease after a spacing of 160 nm since illumination conditions are optimized to a smaller spacing at 100 nm.

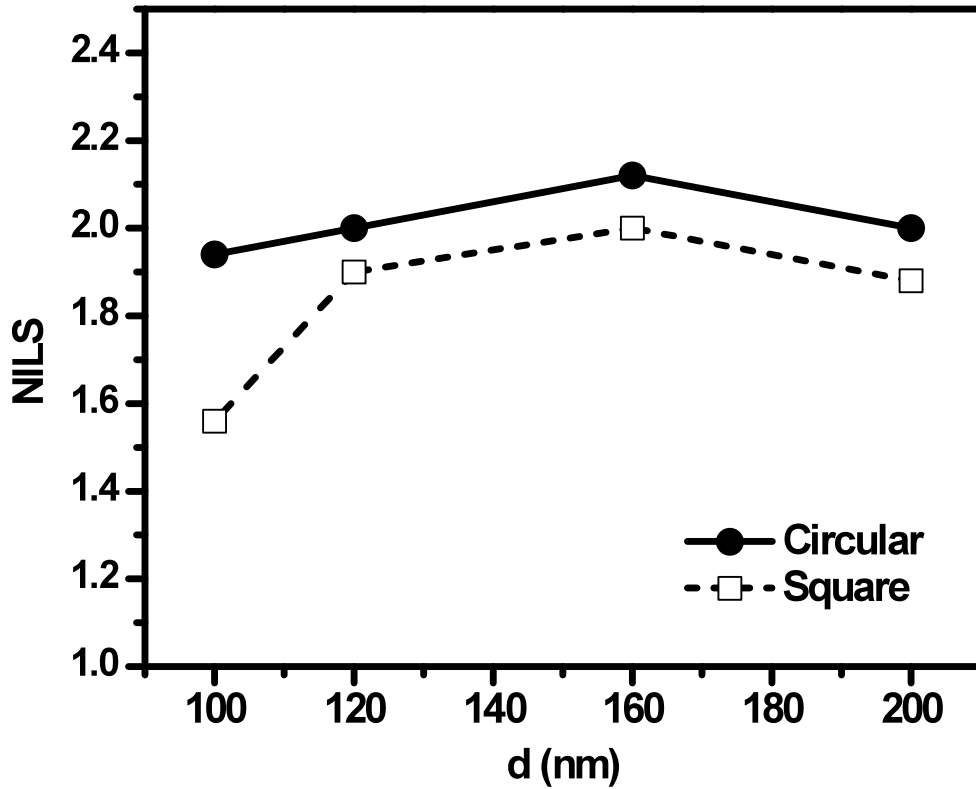
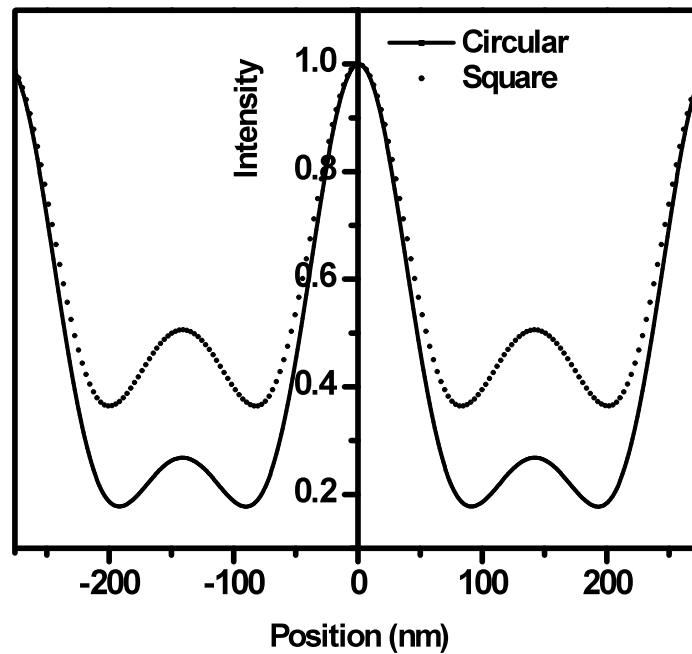


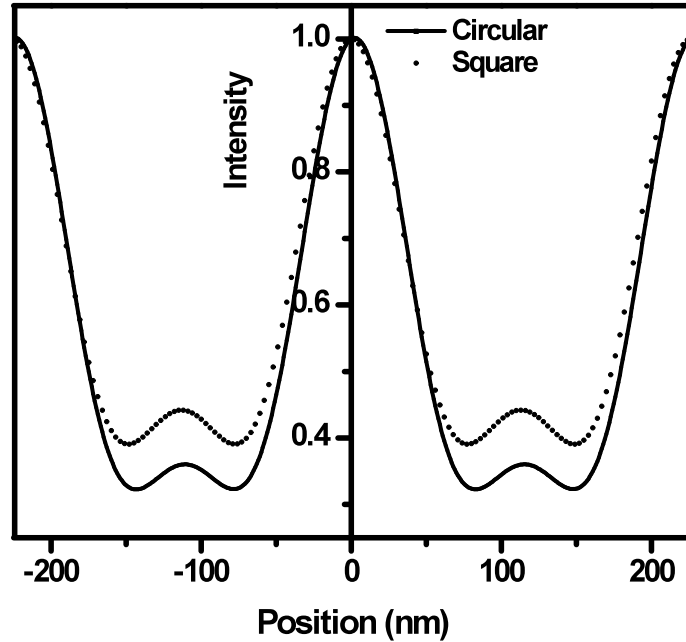
Fig. 5.40 A comparison of NILS between mask with circular and square apertures for a staggered contact hole pattern with spacing d

The aerial image intensity plots for a staggered contact hole pattern with spacings of 160 nm and 200 nm are shown in Fig. 5.41. The aerial image contrast for patterns with circular apertures are 0.67 and 0.51 at spacings of 160 nm and 200 nm respectively. While the aerial image contrast for pattern using square apertures are 0.45 and 0.42 at spacings of 160 nm and 200 nm respectively. Thus, it can be observed that the difference between the maximum and minimum image intensity is larger for a circular aperture. Furthermore, the improvement of aerial image contrast is more significant for a smaller spacing. This is a favorable condition as with the progress of dimensional scaling, the

distance between neighboring features would decrease. It is noteworthy that at these spacing values, the aerial image experiences the formation of secondary peaks in between neighboring features. These peaks are the result of constructive interference between light diffracted from the aperture into the space between neighboring holes. If the intensity of these peaks is high enough, undesired side lobes will be formed and thus affect the process yield. At a spacing of 160 nm, the secondary peak resulted from a circular aperture is 35 % of the maximum intensity. The secondary peak for a square aperture is 10 % higher than that of a circular aperture. At a spacing of 200 nm, the secondary peak formed by a circular aperture is around 25 % of the maximum image intensity. However, the image formed by a square aperture resulted in a secondary peak that is 20 % higher. The lowering of the secondary peak is attributed to the improvement in the collection of 0th and 1st order light since a circular aperture has more gradual transition of shape at the corners than a square aperture.



(a)



(b)

Fig. 5.41 A comparison of aerial image intensity between mask with circular and square apertures for a staggered contact hole pattern with (a) $d = 160\text{nm}$, and (b) $d = 200\text{nm}$

5.3.4 Optimization of Δr in radial segmentation approach

An aerial image contrast of a staggered contact hole pattern can be enhanced by the addition of radial extension segments. In this study, segments are added along a 45° direction of two neighboring features with an opening angle of 45° . The addition of segments is to ensure the CD of contact hole along the 45° direction meets the requirement. The radial extension allows additional light to pass through and improves the aerial image intensity. Segmentations are carried out by changing the radial extension Δr (Fig. 3.17). The effect of radial segmentation is shown in Fig. 5.42. In general, it is seen that NILS improves with radial extension through to a limited extent. The implementation of radial extension allows additional light to be collected for image reconstruction and improves the aerial image intensity. However, due to limitation of the space between neighboring features and the risk of pattern bridging, the radial extension

cannot be increased indefinitely. For a pattern with the smallest spacing of 100 nm, the improvement in NILS with a radial extension of 7.5 nm is around 8 %. However, no further improvement is observed when Δr increases beyond this value. As the spacing increases to 160 nm, the effect of radial extension becomes more obvious. The enhancement in NILS is around 31 % for a radial extension of 17.5 nm. For a pattern with the largest spacing of 200 nm, a 50 % improvement in NILS is observed for a radial extension of 25 nm. Furthermore, it can also be observed that by implementing the radial extension, the aerial image NILS between patterns with different spacings can be brought closer to each other, which helps in achieving a more robust process control.

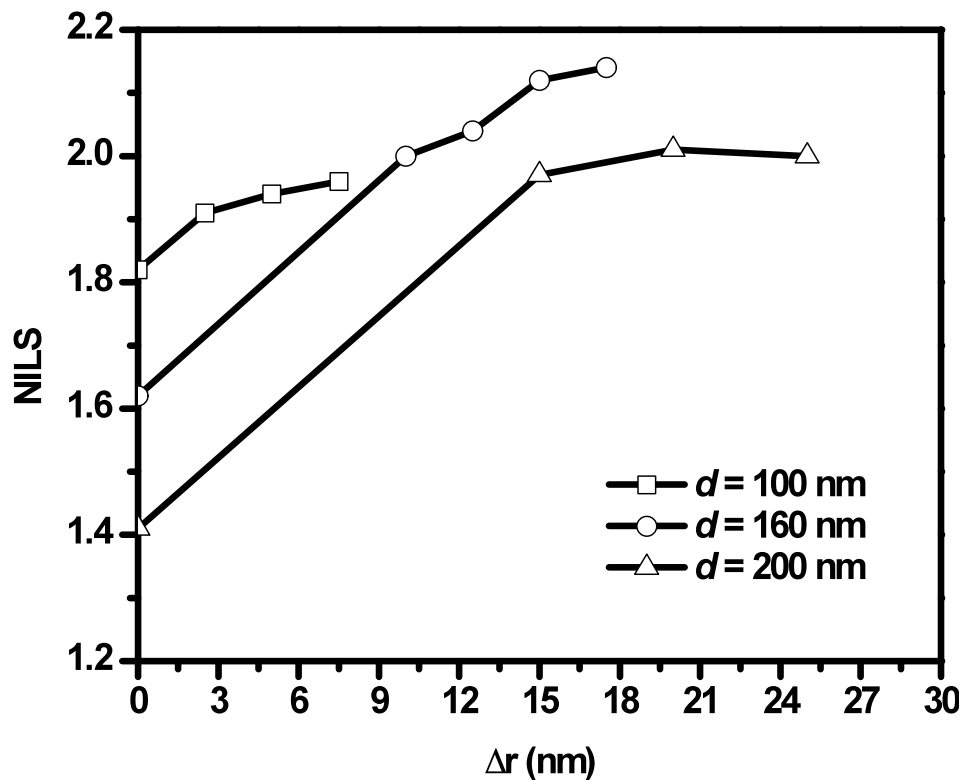
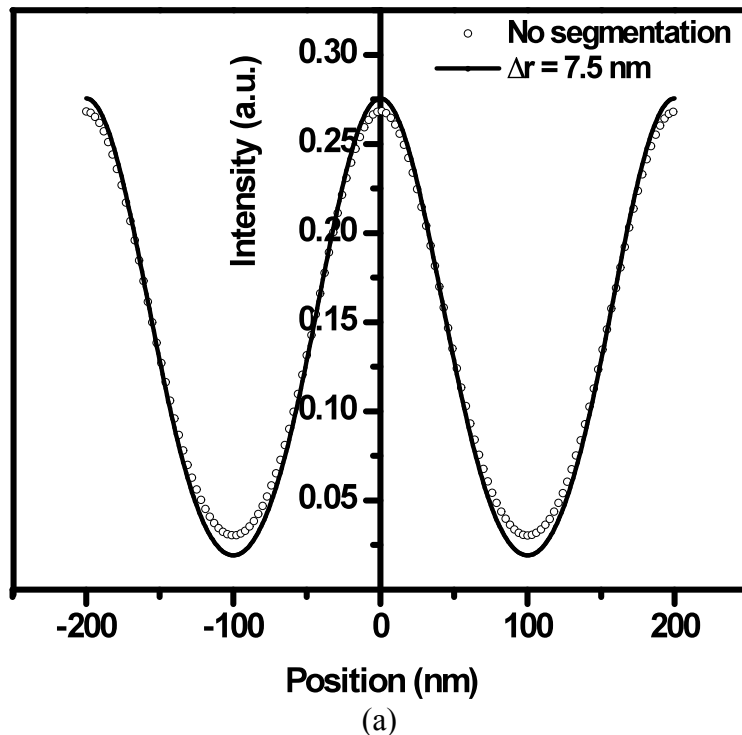


Fig. 5.42 Optimization of radial extension Δr for staggered contact holes with different spacing d by NILS

A comparison in aerial image intensity between a pattern with and without radial extension is shown in Fig. 5.43. For a pattern with a spacing of 100 nm and a radial extension Δr of 7.5 nm, the aerial image contrast is improved by 12 %. More improvement is observed for pattern with a spacing of 160 nm, where the aerial image contrast is improved by 55 % when a radial extension of 17.5 nm is applied. Furthermore, for a pattern with a spacing of 200 nm, the aerial image contrast is improved by 60 % with a radial extension of 20 nm. The aerial image side lobe intensity is also reduced when a radial extension is applied. For patterns with spacings of 160 nm and 200 nm, the maximum side lobe intensity is reduced by 50 % with radial segmentation. Thus, it is seen that by applying the radial extension on a staggered contact hole pattern, the aerial image intensity profile is enhanced with a higher maxima and a lower minima. From the results, the optimum radial extension ranges from 5 % to 7 % of the radial separation (which is equivalent to $\sqrt{2}d$).



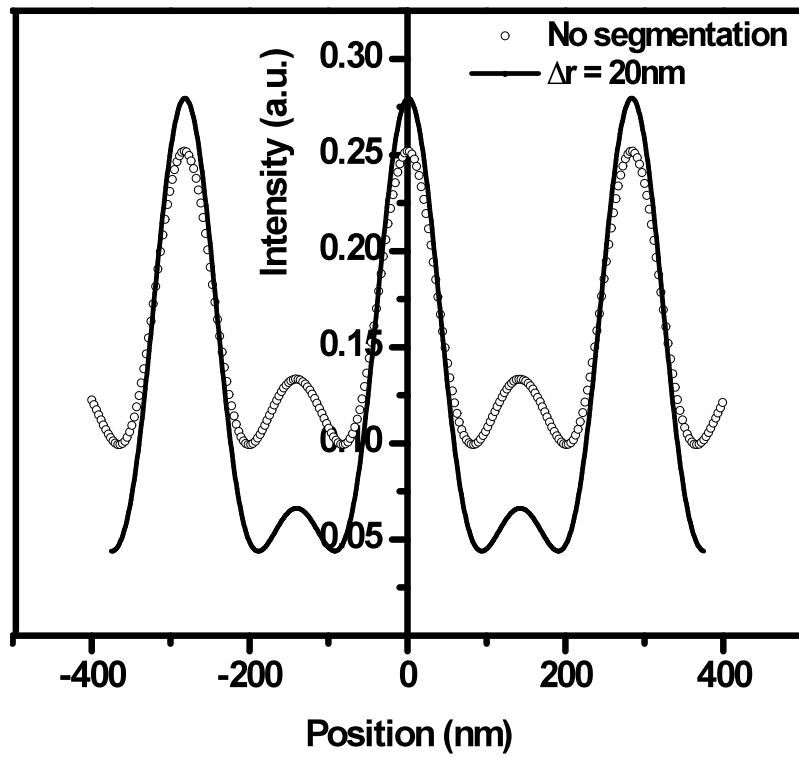
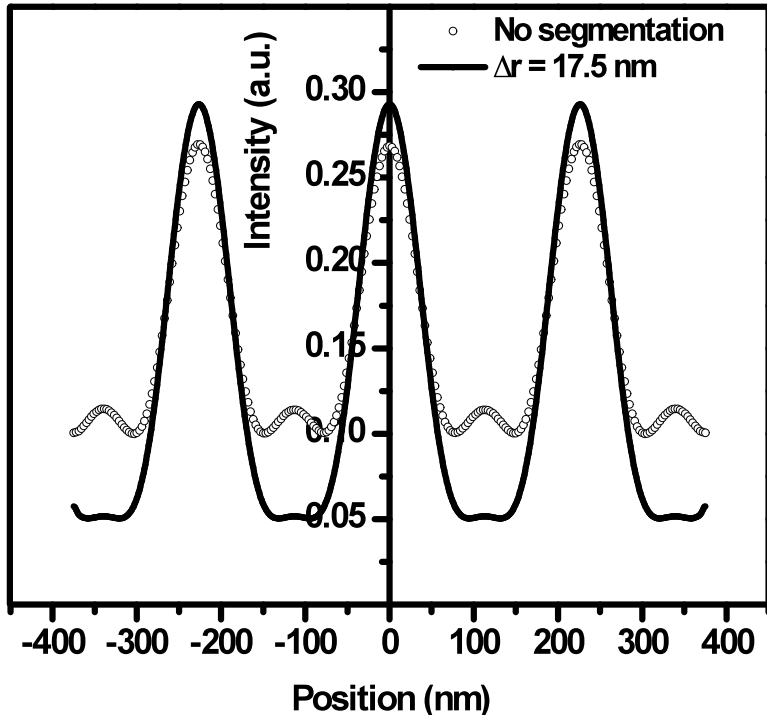


Fig. 5.43 A comparison of aerial image intensity between a staggered contact hole pattern with and without radial extension for spacing of (a) $d = 100$ nm, (b) $d = 160$ nm and, (c) $d = 200$ nm

Chapter 6 Conclusions and recommendations for future work

6.1 Conclusions

In this thesis, several issues regarding RET in immersion lithography have been studied. Firstly, the influence of defects on the patterning of the main feature of a 193 nm immersion lithography phase shifting mask is investigated. Parameters including defect size, location, pattern density, transmission, phase shift, and partial coherence are studied. The results indicate that the CD variation increases with the defect size and an adjacent defect has a more significant influence on the CD variation than a mid-point defect. Patterns with a smaller pitch show a higher sensitivity to the presence of a defect. The influence of transmission is dependent on the types of defect. Process related defects with a higher transmission show a larger influence on the CD variation while haze defects with a lower transmission show a larger influence on the CD variation. In addition, a lower partial coherence also results in an increase in the CD variation.

Secondly, a modified OAI is proposed and simulations to study its effect on imaging performance is carried out. A conventional OAI is modified by inserting a duplicate of the basic source at a region that corresponds to the optimum settings at the forbidden pitch. Computed results show that the maximum CD fluctuation for the proposed double annular illumination is 3% for the pitch range studied compared to a 13% fluctuation for the conventional annular illumination. The degradation in DOF at the forbidden pitch region is also reduced to 21% compared with 49% of DOF at the smallest pitch for conventional annular illumination. The effect of forbidden pitch is thus minimized and

patterning can also be carried out simultaneously with other pitch sizes. The method also provides flexibility for adjustment according to the pitch size to be patterned. Furthermore, the proposed technique can also be extended to include non-annular OAI sources. A patent application is submitted based on this concept of modified OAI. In the patent proposal, various shapes of OAI and methodology as discussed in this thesis for optimization are covered.

In addition, a new method for contact hole patterning is also studied. Instead of a square printed target, a circular OPC target is proposed. In this approach, circular apertures are adopted in place of conventional square apertures. From the simulated results, it is seen that that CD through pitch performance is improved. A reduction in CD deviation from 4 % to 1.25 % is achieved and the CD fluctuation is reduced from 6.25 % to 2.5 %. The process window robustness is also improved by applying the proposed method. From the simulated results, the average improvement in the DOF is around 15 %. The common process window improvement is 35 %. The improvement in CD and DOF can be attributed to the improvement in aerial image quality. The simulated NILS has also improved by 15 %. The study has shown that the application of a circular printed feature and circular aperture for contact hole patterning is capable of enhancing the process window robustness. A second patent application based on the circular aperture and radial segmentation approach for contact holes patterning is also submitted.

Through the course of this study, insight understandings of issues in application of RET has been achieved. A couple of new approaches for RET have been initiated and verified. A proposal to minimize the forbidden pitch effect due to application of OAI has been verified by simulation. Results agree well with the theoretical analysis. In addition, an

alternative approach for contact hole patterning appears feasible and improvement in image contrast and process window are achieved.

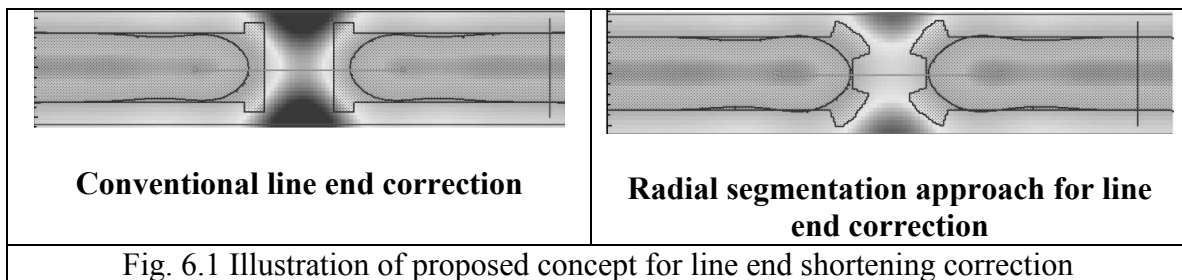
6.2 Recommendations for future work

It has been shown from the study above that process window and resolution enhancement can be achieved by modifying OAI to achieve optimum combination with the mask. A possible extension for future work is to combine the application of modified OAI and circular openings on mask for contact hole patterning. For example, there are some cases where the separation between neighboring contact holes is irregular such as for logic circuits. The concept of modified OAI can thus be applied to achieve optimum image contrast for features with different separations. In addition, the benefits of applying circular openings on masks for contact hole patterning can be exploited. This methodology can be adopted as the basis for the simultaneous optimization of illumination source and mask to achieve process window enhancement.

Based on the understanding of OAI and the use of SRAF developed during the course of this research, a potential interesting field of study in the optimization of SRAF orientation with respect to OAI can be explored. Conventionally, SRAF are always placed in a similar orientation with respect to the main feature, regardless of the shape of the OAI source used. The distance and sizing are the parameters used to optimize the imaging result. A possible parameter that has not been explored intensively is the orientation of the assist feature with respect to the OAI illumination. For example, for a quadrupole illumination, image contrast along the diagonal direction is enhanced. Thus, the effect of assist feature on improving aerial image quality could be enhanced by placing an assist

feature in the orientation of the illumination. Furthermore, the orientation of the main features could be also modified to exploit the benefits of the OAI.

In addition, the concept of a circular aperture can be extended to line end shortening correction. Similar to contact hole patterning, rounded line end can be used as a printed target. Alternatively, the final printed target can be of a curved shape to fulfill the design requirements and line end with curvature can be adopted. Similarly, radial segmentation can be applied to improve the image contrast at the line end corners, as shown in Fig. 6.1 below.



References

A

Airy G.B., On the diffraction of an object-glass with circular aperture, Transactions of Cambridge philosophical society, 1835.

Abbe E., Contributions to the theory of the microscope and the nature of microscopic vision(translated by Fripp H.E.), Archive for microscopic anatomy, 1873.

Asai S., Hanyu I., and Hikosaka K., Improving projection lithography image illumination by using sources far from the optical axis, Journal of vacuum science and technology B, 9, pp.2788-2791, 1991.

Asai S., Hanyu I., and Hikosaka K., High performance optical lithography using a separated light source, Journal of vacuum science and technology B, 10, pp.3023-3026, 1992.

B

M. Born and E. Wolf, Principles of Optics, (Pergammon, New York, 1972), Chap. 10.

Brueck S.R.J., Chen X., Spatial frequency analysis of optical lithography resolution enhancement techniques, Journal of Vac. Sci. Technol. B, 17, pp.908-920, 1999.

Bhattacharyya K., Volk W., Grenon B., Brown D., and Ayala J., Investigation of reticle defect formation at DUV lithography, Proceedings of SPIE 4889, pp.478-487, 2002.

Bok C., Kim S., Kim H., Oh J., Ahn C., and Shin K., 0.33-k1 ArF lithography for 100 nm DRAM, Proceedings of SPIE, 4691, pp.810-821, 2002.

Burkhardt M., and Seong N., Image fidelity improvement through optical proximity correction and its limits, Proc. SPIE 5040, pp.1184-1193, 2003.

Brist T., Bailey G. E., Drozdov A., Torres A., Estroff A., and Hendrickx E., Source polarization and OPC effects on illumination optimization, Proceedings of SPIE, 5992, pp.599232-1 – 599232-9, 2005.

Burning J.H., Optical lithography 40 years and holding, Proceedings of SPIE, 6520, pp.652004-5-652004-13, 2007.

C

Chen J. F., Laidig T., Wampler K., and Caldwell R., Optical proximity correction for intermediate-pitch features using sub-resolution scattering bars, Journal of vacuum science and technology B, 15, pp.2426-2433, 1997.

Cobb N., and Zakhor A., Experimental results on optical proximity correction with variable threshold resist model, Proceedings of SPIE, 3051, pp.458-468, 1997.

Chua G. S., Tay C. J., Quan C., and Lin Q., Modified Rayleigh criterion for 90 nm lithography technologies and below, Journal of vacuum science and technology B, 22, pp.801-808, 2004.

Chen J.H., Chen L.J., Fang T.Y., Fu T.C., Shiu L.H., Huang Y.T., Chen N., Oweyang D.C., Wu M.C., Wang S.C., Lin C.H., Chen C.K., Chen W.M., Gau T.S., Lin B.J., Moerman R., Gehoel W., Heijden E., Jong F., Oorschot D., Boom H., Hoogendorp M., Wagner C., Koek B., Characterization of ArF immersion process for production, Proceedings of SPIE, 5754, pp.13-22, 2005

Coles M., and Somervell M., Minimization of sidelobes in rectangular contact/via hole structures, Proceedings of SPIE, 6154, 61543Z, 2006.

Choi J., Jung J., Lee H., Oh J., Soojung K., Jaehyuck H., Kim Y., and Cho H., Prevention of chemical residue from growing into Haze defect on PSM pattern edge after normal cleaning process, Proceedings of SPIE, 7028, pp.702818-1-702818-9, 2008.

Chua J. K., Murukeshan V. M., Tan S. K., and Lin Q., Investigation of pupil-fill factors as process window indicators for dry optical lithography, Optics and Laser Technology, 40, pp.142-155, 2008.

D

Deng Y., Zou Y., Yoshimoto K., Ma Y., Tabery c., Kye J., Capodiec L., and Levinson H., Considerations in source mask optimization for logic applications, Proceedings of SPIE, 7640, pp.76401J-1-76401J-12, 2010.

E

Erdmann A., Shao F., Fuhrmann J., Fiebach A., Patsis G., Trefonas P., Modeling of double patterning interactions in litho-cure-litho-etch processes, Proceedings of SPIE, 7640, pp.76400B-1-76400B-12, 2010.

F

Finders J., Eurlings M., and Schenau K., Low k1 imaging: how low can we go?, Proceedings of SPIE, 4226, pp.1-15, 2000.

Fahey T., McClay J., Hansen M., TiTi B., and Lipson M.,SVG 157nm Lithography Technical Review, Proceedings of SPIE, 4346, pp.72-80, 2001.

G

Garofalo J., Biddick C., Kostelak R., and Vaidya S., Mask assisted off axis illumination technique for random logic, Journal of vacuum science and technology B, 11, pp.2651-2658, 1993.

Garofalo J., Otto O., Cirelli R., Kostelak R., and Vaidya S., automated layout of mask assist-features for realizing 0.5 k1 ASIC lithography, Proceedings of SPIE, 2440, pp.302-312, 1995.

Goodman J.W., Introduction to Fourier optics, pp.34-36, McGraw-Hill Inc, 1996.

Gans F., Jess M., Kohipoth S., Pforr R., Printability and Repair Techniques for DUV Photomasks, Proceedings of SPIE, 3236, pp.136-141, 1997.

Grenon B., Bhattacharyya K., Volk W., Phan K. and Pooock A., Reticle surface contaminants and their relationship to sub-pellicle defect formation, Proceedings of SPIE 5375, pp.355-362, 2004.

H

Hopkins H.H., On the diffraction theory of optical images, Proc. Of the Royal Society of London Series A, Vol. 217, pp.408-432, 1953.

B. Huynh, K. K. H. Toh, W. E. Haller, and A.R. Neureuther, Optical printability of defects in two-dimensional patterns, Journal of vacuum science and technology B, 6, pp.2207-2212, 1988.

Hoffnagle J. A., Hinsberg W. D., Sanchez M., and Houle F. A., Liquid immersion deep-ultraviolet interferometric lithography, Journal Vacuum Science and Technology B, 17, pp. 3306-3309, 1999.

Hecht E., Optics, pp.443-452, 469-470, Addison Wesley, 2002

Hsu S., Eurlings M., Hendrickx E., Broeke D., Chiou T., Chen J., Laidig T., Shi X., and Finders J., Double dipole lithography for 65 nm node and beyond: a technology readiness review, Proceedings of SPIE, 5446, pp.481-498, 2004.

Hsu M., Broeke D., Laidig T., Wampler E., Hollerbach U., Socha R., Chen J. F., Hsu S., and Shi X., Lithography manufacturing implementation for 65 nm and 45 nm nodes with model based scattering bars using IMLTM technology, Proceedings of SPIE, 5754, pp.355-367, 2005.

Hsu S., Burkhardt M., Park J., Broeke D., and Chen J. F., Dark field double dipole lithography for 45 nm node and beyond, Proceedings of SPIE, 6283, pp.62830U-1-62830U12, 2006.

Hermans J. V., Hendrickx E., Laidler D., Jehoul C., Heuvel V.D.C., and Goethals A.M., Performance of the ASML EUV Alpha Demo Tool, Proceedings of SPIE, 7636, pp.76361L-1-76361L-12, 2010.

I

Ito T., Tanuma M., and Morooka Y., Photo-projection image distortion correction for a 1 μm pattern process, Electronics and Communications in Japan Part II: Electronics 69, pp.30, 1986.

Ito Takashi, and Okazaki Shiji, Pushing the limits lithography, Nature, 406, pp.1027-1031, 2000.

http://www.intel.com/museum/archives/history_docs/mooreslaw.htm, Intel Museum, 2005.

International Technology Roadmap for Semiconductors, ITRS 2007 edition, pp.31, 2007.

J

Joesten L., Reilly M., DeSisto., and Jehoul C., The effect of scattering bar assist features in 193nm lithography, Proceedings of SPIE, 4691, pp.861-870, 2002.

Johnstone E.V., Dieu L., Chovino C., Reyes J., Hong D., Krishnan P., Coburn D., and Capella C., 193-nm haze contamination: a close relationship between mask and its environment, Proceedings of SPIE, 5256, pp.440-448, 2003.

Jones R., and Byers J., Theoretical corner rounding analysis and mask writer simulation, Proceedings of SPIE 5040, pp.1035-1043, 2003.

Jensen S. and Hansen O., Characterization of the microloading effect in deep reactive ion etching of silicon, Proceedings of SPIE, 5342, pp.111-118, 2004.

K

Kawata H., Carter J., Yen A., and Smith H., Optical projection lithography using lenses with numerical apertures greater than unity, Microelectronic engineering, 9, pp.31-36, 1989

Kamon K., Miyamoto T., Myoi Y., Nagata H., Tanaka M., and Horie K., Photolithography system using annular illumination, Japanese journal of applied physics, 30, pp.3021-3029, 1991.

Kalk F., Brankne K., Peters L., Improving Reticle Yields with After Develop Inspection (ADI), Proceedings of SPIE, 3996, pp. 38-46, 2000.

Koay C., Holmes S., Petrillo K., Colburn M., and Burns S., Evaluation of double patterning techniques for advanced logic nodes, Proceedings of SPIE, 7640, 764009-1-764009-10, 2010.

L

Lin B., Partially coherent imaging in two dimensions and the theoretical limits of projection printing in microfabrication, IEEE transactions on electron devices, Vol.27, pp.931-938, 1980.

Levenson M., Viswanathan N., and Simpson R., Improving resolution in photolithography with a phase-shifting mask, IEEE transactions on electron devices, 29, pp.1828-1836, 1982.

Lin B. J., Where is the Lost Resolution, Proceedings of SPIE, 633, p.44-50, 1986.

Lin B. J., Methods to print optical images at low- k_1 factors, Proceedings of SPIE, 1264, pp.2-13, 1990.

Liebmann L. W., Grenon B., Lavin M., Schomody S., Zell T., Optical proximity correction, a first look at manufacturability, Proceedings of SPIE, 2322, pp.229-238, 1994.

Liu H. Y., Karklin L., Wang Y. T., and Pati Y. C., Application of alternating phase-shifting masks to 140 nm gate patterning II: Mask design and manufacturing tolerances, Proceedings of SPIE, 2197, pp.294-301, 1994.

Lam M. and Neureuther A.R., Algebraic model for the printability of nonplanar phase defects, *Journal of Vacuum of Science Technology B*, 21, pp.2815-2820, 2003.

Liebmann L. W., Layout impact of resolution enhancement techniques: impediment or opportunity? , *Proceedings of ISPD*, pp.110-117, 2003.

a. Lin B. J., Immersion lithography and its impact on semiconductor manufacturing, *Journal of Micron/Nanolithography*, 3, pp. 377-395, 2004.

b. Lin B. J., The k_3 coefficient in nonparaxial λ/NA scaling equations for resolution, depth of focus, and immersion lithography, *Journal of Micro/Nanolithography, Microfabrication, and Microsystem*, 3, pp 8-12, 2004.

Lafferty N., Zhou J., Smith B. W., Mask enhancement using evanescent wave effect, *Proceedings of SPIE 6520*, 652041-1-65204-8, 2007.

Labovitz S., Zvi G. B., Dmitriev V., Graitzer E., and Zait E., Detection of progressive transmission loss due to haze with Galileo mask DUV transmittance mapping based on non imaging optics, *Proceedings of SPIE 7122*, 712216, 2008.

Lee. S., Byers J., Jen K., Zimmerman P., Rice B., Turro N., and Wilson C., An analysis of double exposure lithography options, *Proceedings of SPIE*, 6924, pp.69242A-1-69242A-12, 2008.

M

Moore G.E., Cramming more components onto integrated circuits, Electronic magazine, Vol. 38, No. 8, 1965.

Moore G.E., Progress in digital integrated electronics, IEEE International Electron Devices Meeting Technical Digest, pp.11-13, 1976.

Mastromarco V., Neureuther A.R., and Toh K., Printability of defects in optical lithography: Polarity and critical location effects, Journal of vacuum science and technology B, 6, pp.224-229, 1988.

Mack C., Optimum stepper performance through image manipulation, Proceedings of the KTI microelectronics seminar interface 1989, pp.209-215, 1989.

Matsuyama T., Ohmura Y., and Williamson D., The Lithographic Lens: its history and evolution, Proceedings of SPIE, 6520, pp.652002-6 615403-14, 2006.

Mack C., Fundamental principles of optical lithography: The science of microfabrication, pp.58-71, 75-128, 348-352, 419-429, John Wiley & Sons Ltd, 2007.

Melville D., Rosenbluth A., Tian K., and Lai K., Demonstrating the benefits of source mask optimization and enabling technologies through experiment and simulations, Proceedings of SPIE, 7640, pp.764006-1-764006-18, 2010)

N

Neureuther A.R., Flanner P., and Shen S., Coherence of defect interactions with features in optical imaging, *Journal vacuum science and technology B*, 5, pp.308-312, 1987.

Nitayama A., Sato T., Hashimoto K., Shigemitsu F., and Nakase M., New phase shifting mask with self-aligned phase shifters for a quarter micron technology, *IEDM technical digest*, 89, pp.57-60, 1989.

Noguchi M., Muraki M., Iwasaki Y., and Suzuki A., Subhalf micron lithography system with phase-shifting effect, *Proceedings of SPIE*, 1674, pp. 92-104, 1992.

O

Owen G., Pease R. F. W., Markle D. A., Grenvile A., Hsieh R. L., Bunau R. V., and Maluf N. I., 1/8 μm optical lithography, *Journal of Vacuum Science and Technology B*, 10, pp.3032-3036, 1992.

Ogawa T., Uematsu M., Ishimaru T., Kimura M., and Tsumori T., The effective light source optimization with the modified beam for the depth-of-focus enhancements, *Proceedings of SPIE*, 2197, pp.19-30, 1994.

Orii S., Sekino T., and Ohta M., Quarter-micrometer lithography system with oblique illumination and pupil filter, *Proceedings of SPIE*, 2197, pp.854-868, 1994.

Otto O., and Henderson R., Advances in process matching for rule-based optical proximity correction, Proceedings of SPIE, 2884, pp.425-434, 1996.

Owa S. and Nagasaka H., Immersion lithography; its potential performance and issues, Proceedings of SPIE, 5040, pp.724–733, 2003.

Ooishi K., Esaki Y., Sakamoto K., Sakurai H., Itoh M., Nakao M., Nishimura T., Miyashita H., Hayashi N., Tanabe S., Oosaki Y., and Sasagawa Y., New development method eliminating the loading and microloading effect, Proceedings of SPIE, 5130, 67-77, 2003.

Osborne S., Nanninga M., Takahashi H., and Woster E., Mask cleaning strategies: haze elimination, Proceedings of SPIE, 5992, 59923H, 2005.

P

Prouty M., and Neureuther A., Optical imaging with phase shift masks, Proceedings of SPIE, 470, pp.228-232, 1984.

Park J., Hsu S., Broeke D. V. D., Chen J. F., Dusa M., Socha R., Finders J., Vleeming B., Oosten A., Nikolsky P., Wiaux V., Hendrickx E., Bekaert J., and Vandenberghe G., Application challenges with double patterning technology (DPT) beyond 45 nm, Proceedings of SPIE, 6349, pp.634922.1-634922.12, 2006.

R

Reynolds G., A concept for a high resolution optical lithographic system for producing one-half micron linewidths, Proceedings of SPIE, 633, pp.228-238, 1986.

Rieger M., and Stirniman J., Mask fabrication rules for proximity corrected patterns, Proceedings of SPIE, 2884, pp.323-332, 1996.

Rothschild M., Bloomstein T.M., Liquid immersion lithography: Why, how and when?, Journal of Vac. Sci. Technol. B, pp.2877-2881, 2004.

Roy S., Broeke D. V. D., Chen J. F., Liebchen A., Chen T., Hsu S., Shi X., and Socha R., Extending aggressive low-k1 design rule requirements for 90-nm and 65-nm nodes via simultaneous optimization of NA, illumination, and OPC, Proceedings of SPIE 5379, pp.190-201, 2004.

Rosenbluth A.E., Seong N., Global optimization of the illumination distribution to maximize integrated process window, Proceedings of SPIE, 6154, pp.61540H-1-61540H-12, 2006.

Rosenbluth A. E., Melville D., Tian K., Bagheri S., Jaione T., Lai K., Waechter A., Inoue T., Ladanyi L., Barahona F., Scheinberg K., Sakamoto M., Muta H., Gallagher E., Faure T., Hibbs M., Trichtkov A., and Granik Y., Intensive optimization of masks and sources for 22nm lithography, Proceedings of SPIE 7274, 727409, 2009.

S

Saleh B., and Sayegh S., Reduction of errors of microphotographic reproductions by optimal corrections of original mask, *Optical Engineering*, 20, pp.781-784, 1981.

Starikov A., Use of single size square serif for variable print bias compensation in microlithography: method, design and practice, *Proceedings of SPIE*, 1088, 34-46, 1989.

Schellenberg F. M., Optimization of real phase mask performance, *Proceedings of SPIE*, 1604, pp.274-296, 1992.

Shiraishi N., Shigeru H., Takeuchi Y., and Magome N., New imaging technique for 64M-DRAM, *Proceedings of SPIE*, 1674, pp.741-752, 1992.

Socha R., Neureuther A.R., and Singh R., Models for characterizing phase-shift defects in optical projection printing, *IEEE Transactions on Semiconductor Manufacturing*, 8, pp.139-149, 1995.

Schellenberg F. M., Zhang H., Morrow J., Evaluation of OPC efficacy, *Proceedings of SPIE*, 2726, pp.680-688, 1996.

Smith B.W., Sheats J.R., *Microlithography: Science and Technology (Chapter 3: Optics for photolithography)*, pp.194-195, Marcel Dekker, 1998.

Shi X., Hsu S., Chen F., Hsu M., Socha R. J., Dusa M., Understanding the forbidden pitch phenomenon and assist feature placement, Proceedings of SPIE, 4689, pp.985-995, 2002.

Singh N., and Mukherjee M., Effect of feature size, pitch, and resist sensitivity on side-lobe and ring formation for via hole patterning in attenuated phase-shift masks, Proceedings of SPIE, 4691, 1054-1061, 2002.

Smith B. W., Forbidden pitch or duty-free: revealing the causes of across-pitch imaging differences, Proceedings of SPIE, 5040, pp.399-407, 2003.

Socha R., Broeke D., Hsu S., Chen J.F., Laidig T., Corcoran N., Hollerbach U., Wampler K., Shi X., and Conley W., Contact hole reticle optimization by using interference mapping lithography (IML), Proceedings of SPIE, 5446, pp.516-534, 2004.

Schmid R., Zibold A. M., Bhattacharya K., Chen X., and Grenon B., Evaluation of printability of crystal growth defects in a 193nm lithography environment using AIMS, Proceedings of SPIE, 5567, pp.1035-1043, 2004.

Schellenberg F.M., Selected papers on resolution enhancement techniques in optical lithography, pp.205, SPIE Press, 2004.

Schellenberg F. M., A history of resolution enhancement technology, Optical review, Vol. 12, No.2, pp.83-89, 2005.

Socha R., Shi X., and LeHoty D., Simultaneous source mask optimization (SMO), Proceedings of SPIE, 5853, pp.180-193, 2005.

Singh V., Computational lithography: the new enabler of Moore's law, Proceedings of SPIE 6827, pp.68271Q-1-68271Q-5, 2007.

Singh V., Hu. B., Toh K., Bollepalli S., Wagner S., and Borodovsky Y., Making atrillion pixel dance, Proceedings of SPIE, 6924, pp.69240S-1-69240S-12, 2008.

I

Terasawa T., Hasegawa N., Fukuda H., and Katagiri S., Imaging characteristics of multi phase-shifting and halftone phase-shifting masks, Japanese journal of applied physics, 30, pp.2991-2997, 1991.

Tsujita K., Mikami K., Naka R., Baba N., Ono T., and Suzuki A., Illumination optimization with actual information of exposure tool and resist process, Proceedings of SPIE 6520, pp.652036-1 – 652036-12, 2007.

Terai M., Ishibashi T., Shinohara M., Yonekura K., Hagiwara T., Hanawa T., Kumada T., Double patterning using dual spin-on Si containing layers with multilayer hard mask process, Proceedings of SPIE, 6924, pp.692420-1-692420-9, 2008.

V

A. Vanleenhove, D. Van Steenwinckel, A litho-only approach to double patterning, Proceedings of SPIE, 6520, 65202F, 2007.

W

Wolf S., Silicon processing for the VLSI era, Vol. 2, pp.5-11, Lattice Press, 1990.

Waas T., Eisenmann H., and Hartmann H., Proximity correction for high CD-accuracy and process tolerance, Proceedings of symposium on nanocircuit engineering, 1994.

Watson P., Cirelli R., Timko A., Nalamasu O., Lockstamphor C., Berger S., Bassom N., and Sundaram G., Proceedings of SPIE, 3334, pp.131-139, 1998.

Wong K. K., Resolution Enhancement Techniques in Optical Lithography, pp.71, 91, 118, SPIE Press, 2001.

Wong P., Wiaux V., Verhaegen S., and Vandebroek N., Litho-process-litho for 2D 32 nm hp logic and DRAM double patterning, Proceedings of SPIE, 7640, pp.76400I-1-76400I-11, 2010.

Y

Youn J., Shin K., Park H., and Kim D., Effects of Process Parameters on Microloading

in Sub—halfmicron Aluminum Etching, Proceedings of SPIE, 2875, pp.312-321, 1996

Appendix A List of publications

Journals

Ling M. L. , Tay C. J. , Quan C. , Chua G.S. , and Lin Q., Forbidden pitch improvement using modified illumination in lithography, Journal of Vacuum Science and Technology B, 27, pp.85-91, 2009

Tay C. J. , Quan C. , Ling M. L. , Lin Q. , Chua G. S. , Effect of process related and haze defects on 193 nm immersion lithography, Journal of Vacuum Science and Technology B, 28, pp.45-51, 2010

Tay C. J. , Quan C. , Ling M. L. , Chua G. S. , Tan S. K., Lin Q. , Circular apertures for contact holes patterning in 193 nm immersion lithography, Submitted to Journal of Vacuum Science and Technology B.

Conferences

Ling M. L. , Chua G. S. , Tay C. J. , Quan C. , Lin Q. , A comparative study for mask defect tolerance on phase and transmission for dry and immersion 193-nm lithography, Proceedings of SPIE 6520, 2007.

Ling M. L. , Chua G. S. , Lin Q. , Tay C. J. , Quan C. , Customized illumination shapes for 193nm immersion lithography, Proceedings of SPIE 6924, 2008.

Ling M. L. , Chua G. S. , Lin Q. , Tay C. J. , Quan C. , Line end shortening and corner rounding for novel off-axis illumination source shapes, Proceedings of the SPIE 7274, 2009.

Tay C. J. , Quan C. , Ling M. L. , Lin Q. , Tan S. K. , Chua G. S. , Circular apertures for contact hole patterning in 193-nm immersion lithography, Proceedings of SPIE 7522, 2010.

Ling M. L. , Chua G. S. , Tan S. K. , Quan C. , Lin Q. , Radial segmentation approach for contact hole patterning in 193 nm immersion lithography, Proceedings of SPIE 7640, 2010.

U.S. Patents

Ling M. L. , Chua G. S. , Lin Q. , Tay C. J. , Quan C. , Methods for enhancing photolithography patterning (Submitted in February 2008)

Tan S. K. , Ling M. L. , Chua G. S. , Chong R. , Yeo M. , Mask system employing substantially circular optical proximity correction target and method (Submitted in October 2008)

Appendix B Rayleigh resolution criterion

The image formed by a circular aperture through an imaging system is high circular spot with central maximum, known as Airy disk, named after Sir George Biddell Airy who derived the intensity of it. Airy disk consists of a central maximum surrounded by a dark ring. Alternating dark and bright ring can be observed around the Airy disk. The radius of an Airy disk is defined as the distance from central maximum to the first dark ring.

The radius of an Airy disk is given by:

$$r = 1.22 \frac{f\lambda}{D} \quad (\text{B1})$$

f is the focal length of the imaging system, λ is the wavelength of incident light and D is the diameter of the aperture. In order to determine the resolution of an imaging system, the airy disk produce by two point sources can be considered. Each of the point source will produce an Airy disk pattern. As the distant between these two point sources become closer, two Airy disks will be overlapping. Lord Rayleigh's criterion for resolution can be applied and the two Airy disks are just resolvable when the center of one Airy disk falls on the first minimum of another Airy disk. Thus the minimum resolvable angular separation is

$$\Delta\theta = \frac{r}{f} = 1.22 \frac{\lambda}{D} \quad (\text{B2})$$

The minimum separation between features is

$$\Delta l = 1.22 \frac{\lambda f}{D} \quad (\text{B3})$$

In lithography, Rayleigh's resolution criterion is applied to determine the minimum separation between features. As the distance between neighbour features becomes smaller,

diffraction order becomes more widely spread. Consider the extreme case when 1st order light incident at the outer edge of the projection lens (Fig. B1). The smallest pitch that is resolvable is thus :

$$\frac{1}{p} = \frac{\sin \theta_{\max}}{\lambda} = \frac{NA}{\lambda} \quad (\text{B4})$$

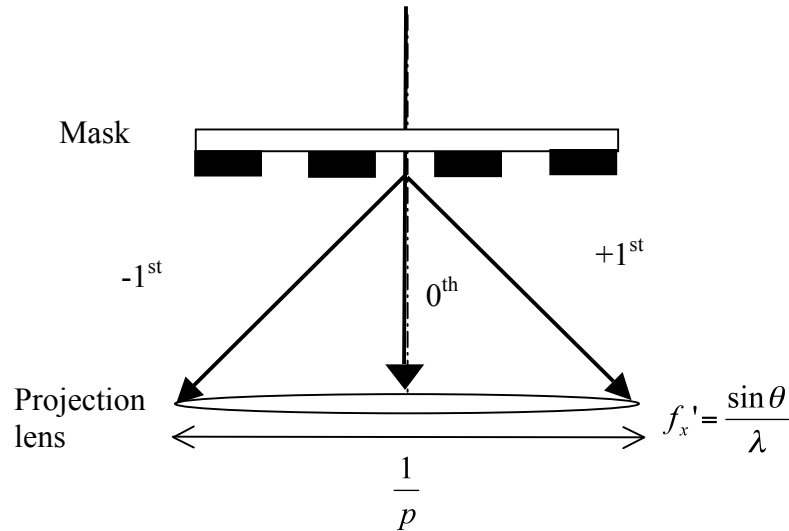


Fig. B1 Diffraction order distribution at resolution limit

Resolution is defined as the minimum line width that an imaging system can produce.

Assuming equal line and space, the minimum line width is half of the pitch

$$R = \frac{p}{2} = 0.5 \frac{\lambda}{NA} \quad (\text{B4})$$

Equation (B4) is the theoretical resolution for an imaging system. In deriving Eq. (B4), it is assumed that the projection lens is free from aberrations and thus the resolution depends on the collection of diffraction order. It is known as diffraction limited resolution.

Also, light is assumed to incident normally on the mask. A more general form of expression for resolution in lithography can is written as:

$$R = k_1 \frac{\lambda}{NA} \quad (B5)$$

k_1 is a parameters related to process and it can be seen as a scaling factor. Resolution enhancement techniques (RET) can be applied to push the resolution limit below that indicated by Eq. (B5). Various forms of RET will be discussed in a later section.

Another important parameter in lithography is depth of focus (DOF). Lord Rayleigh had also provided a simple approach to estimate DOF in an imaging system. In Fig. B2, the relationship between change in focus and the phase difference between zero order light and first order light at the edge of projection lens is shown. Rayleigh's criterion states that DOF is the distance z for which the optical path difference between the two rays equals to a quarter of the wavelength. Optical path difference is defined as the product of refractive index of the medium and distance traveled by light. DOF can be found by:

$$DOF = \frac{\lambda}{4} \frac{1}{(1 - \cos \theta)} = \frac{\lambda}{4} \frac{1}{2 \sin^2(\theta/2)} \approx \frac{\lambda}{2NA^2} \quad (B6)$$

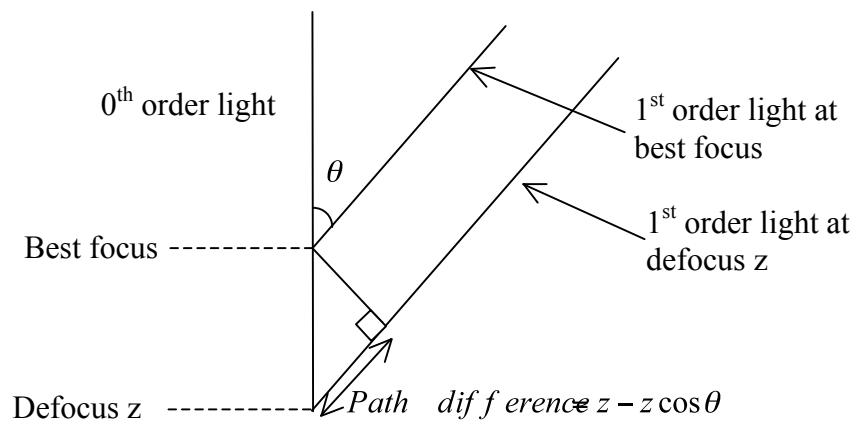


Fig. B2 Optical path difference at defocus z

A general form of expression for DOF can be written as

$$DOF = k_2 \frac{\lambda}{NA^2} \quad (B7)$$

k_2 is the process parameter.

Eq. (B5) and (B7) are known as the Rayleigh's resolution criteria in lithography. k_1 and k_2 are used to quantify the difficulty of a lithography process. Low k_1 process requires application of RET and generally has smaller DOF.

Appendix C Resist calibration

Resist calibrations were carried out before using LithoCruiser for the purposes of this study. Experimental data for line and space pattern with various pitches was collected from an immersion production tool. Subsequently, by applying the same exposure conditions (focus, dose, OAI illumination shape and partial coherent settings) and the line and space pattern, resist parameters such as the threshold values, diffusion constant were calibrated using LithoCruiser™ resists calibrations function. Based on the simulated image intensity function, LithoCruiser™ will fit various resist parameters by series of iterations using hybrid model based on fundamental diffusion phenomenon and some empirical model. Figure C.1 shows the comparison between experimental and simulation CD through pitch performance for line and space pattern with a target CD of 73 nm after resist calibrations is done. It is observed that the difference between experimental and simulation data is around 3 % for the pitch range studied.

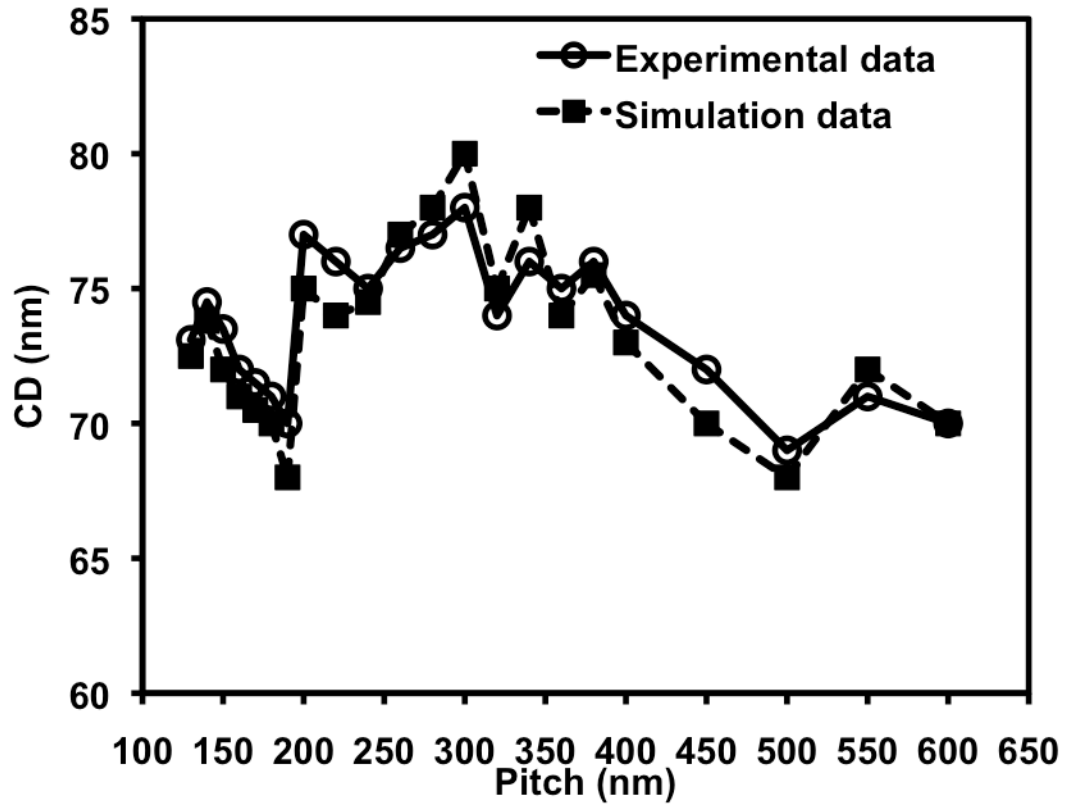


Fig. C.1 Through pitch performance comparison for line and space pattern after resist calibration